

**TECHNICAL
TRANSACTIONS**

MECHANICS

**ISSUE
3-M (21)**

**YEAR
2015 (112)**

**CZASOPISMO
TECHNICZNE**

MECHANIKA

**ZESZYT
3-M (21)**

**ROK
2015 (112)**



**WYDAWNICTWO
POLITECHNIKI
KRAKOWSKIEJ**

TECHNICAL TRANSACTIONS

MECHANICS

**ISSUE 3-M (21)
YEAR 2015 (112)**

CZASOPISMO TECHNICZNE

MECHANIKA

**ZESZYT 3-M (21)
ROK 2015 (112)**

Chairman of the Cracow
University of Technology Press
Editorial Board

Chairman of the Editorial Board

Jan Kazior

Józef Gawlik

Przewodniczący Kolegium
Redakcyjnego Wydawnictwa
Politechniki Krakowskiej

Przewodniczący Kolegium
Redakcyjnego Wydawnictw
Naukowych

Scientific Council

Jan Błachut
Tadeusz Burczyński
Leszek Demkowicz
Joseph El Hayek
Zbigniew Florjańczyk
Józef Gawlik
Marian Giżejowski
Sławomir Gzell
Allan N. Hayhurst
Maria Kusnierova
Krzysztof Magnucki
Herbert Mang
Arthur E. McGarity
Antonio Monestioli
Günter Wozny
Roman Zarzycki

Rada Naukowa

Mechanics Series Editor

Andrzej Sobczyk

Redaktor Serii Mechanika

Section Editor

Dorota Sapek

Sekretarz Sekcji

Typesetting

Adam Bania

Skład i łamanie

Native Speaker

Robin Gill

Wryfikacja językowa

Cover Design

Michał Graffstein

Projekt okładki

Basic version of each Technical Transactions magazine is its online version

Pierwotną wersją każdego Czasopisma Technicznego jest wersja on-line

www.ejournals.eu/Czasopismo-Techniczne www.czasopismotechniczne.pl www.technicaltransactions.com

ELŻBIETA AUGUSTYN*, MAREK S. KOZIEŃ**

POSSIBILITY OF EXISTENCE OF TORSIONAL VIBRATIONS OF BEAMS IN LOW FREQUENCY RANGE

MOŽLIWOŚCI WYSTAÑPIENIA DRGAÑ
SKRĘTNYCH W BELKACH W ZAKRESIE
NISKOCZĘSTOTLIWOŚCIOWYM

Abstract

This paper discusses the problem of the existence of torsional natural modes in the low frequency range for a beam with a rectangular cross-section with different ratios between width and height and different lengths. The rectangular type of cross-section is chosen because of practical applications to describe the vibrations of some turbine blades. The analyses were conducted by applying an analytical model, but were verified using the finite element method.

Keywords: *torsional vibrations, low frequency analysis, natural vibrations*

Streszczenie

W artykule rozważono zagadnienie możliwości wystąpienia form własnych drgań skrętnych w zakresie niskoczęstotliwościowym belek o prostokątnym kształcie przekroju. Rozważano wpływ stosunku wysokości do szerokości przekroju oraz długości belki. Prostokątny kształt przekroju został wybrany ze względu na zastosowania praktyczne analiz do opisu drgań łopatek turbin niektórych wirników. Rozważania opierają się na modelu analitycznym, ale były również weryfikowane poprzez analizy metodą elementów skończonych.

Słowa kluczowe: *drgania skrętne, analiza niskoczęstotliwościowa, drgania własne*

DOI: [10.4467/2353737XCT.15.170.4375](https://doi.org/10.4467/2353737XCT.15.170.4375)

* MSc. Elżbieta Augustyn, Faculty of Mechanical Engineering, Cracow University of Technology (PhD student).

** PhD. DSc. Marek S. Kozień, Institute of Applied Mechanics, Faculty of Mechanical Engineering, Cracow University of Technology.

1. Introduction

When analysing one-dimensional continuous type structural elements with a straight line in the general case, combined torsional-bending vibrations can arise. If the cross-section has two axes of symmetry, the shear centre and the gravity centre of the cross-section are the same point, and the torsional vibrations and the bending ones are separated. Therefore the torsional vibration of the beam can be analysed separately [4, 5, 9].

The motion of a realistic structure, independent of its shape, can be described as a deformable body. But to simplify the analysis, simpler models of the elements are commonly used. One of the groups to be considered is known as one-dimensional structures e.g. beams, shafts, rods. Due to the realistic cross-section shape, the description of motion of a beam can be described under some assumptions by applying a suitable theory. The general two groups of models, bearing in mind shape of the cross-section, are those for thin-walled cross-section and the monolytic ones [1, 3–5, 9]. If one characteristic dimension of the cross-section (known as the thickness) is small enough in comparison with the second one (known as the width) the whole structure is called thin-walled. A detailed rule states that for a thin-walled cross-section the thickness is more than eight times smaller than the highest dimension measured along the middle-line of the cross-section between its two end-points. Moreover, this length should be more than eight times smaller than the length of the beam [9]. It should be noted that the rectangle type of cross-section, for any ratios between width and height of cross-section, is to be understood as a monolytic type cross-section [9].

For some engineering applications, due to shape of their cross-sections and type of external loadings, the one-dimensional elements of beam type can be excited to torsional vibrations. For such cases, the torsional modes often lie in the low frequency for the structure [7]. The low frequency range is connected with the structure being analysed and is the range of frequency for which the modal density is not so high (not more than 10) and the value of the modal overlap factor is approximately unity.

It is commonly used in engineering vibrations to classify the frequency range of analysis to regions of low- and high-frequency. It should be pointed that the frequency upper limit of low-frequency analysis, and frequency the lower limit for high-frequency analysis depends on the dynamic characteristic of the structure analysed. In particular, it is a function of two parameters: modal density and modal overlap factor [2, 6].

This paper discusses the problem of the existence of torsional natural modes in the low frequency range for a beam with a rectangular cross-section with different ratios between width and height and different lengths. The low frequency range analysis is understood as taking into account a few of the lowest natural modes. The rectangular type of cross-section is chosen because of practical applications.

2. Natural vibrations of a beam

2.1. Torsional vibration

When the cross-section of a beam is a monolithic type with two axes of symmetry the equation of motion for natural torsional vibrations is independent of the equations of motion of bending vibrations, and has the form (1), where: $\varphi(x, t)$ – angle of torsion of the cross-

section, G – shear modulus, ρ – material density, J_s – equivalent moment of inertia of cross-section due to torsion, J_0 – polar moment of inertia of the cross-section.

$$\rho J_0 \frac{\partial^2 \varphi(x,t)}{\partial t^2} - G J_s \frac{\partial^2 \varphi(x,t)}{\partial x^2} = 0 \quad (1)$$

If the cross-section is circular in shape, the equivalent moment of inertia of cross-section due to torsion J_s is equal to the polar moment of the inertia of cross-section J_0 and the equation of vibrations of the beam (1) is simplified to form (2).

$$\frac{\partial^2 \varphi(x,t)}{\partial t^2} - \frac{G}{\rho} \frac{\partial^2 \varphi(x,t)}{\partial x^2} = 0 \quad (2)$$

Differential equations for torsional vibrations (1) or (2) can be solved to find the values of natural frequencies and mode shapes after taking into account two boundary conditions. These can be formulated by giving suitable values of:

- angle of torsion $\varphi(x, t)$ for a given cross-section,
- value of torsional moment $M_s = G J_s \frac{\partial \varphi}{\partial x}$ for a given cross-section.

For a non-circular cross-section during the process of torsion the deformation of cross-sections is observed (sometimes called warping). When analysing this process, the equivalent moment of inertia of cross-section due to torsion J_s can be analytically formulated for the cross-section under consideration. If the rectangular cross-section is analysed, it can be determined approximately based on formula (3) [8–11], where: b – width of cross-section, h – height of cross-section. The formula can be simplified to form (4) [8, 10].

$$J_s = b^3 h \left(\frac{1}{3} - \frac{64}{\pi^5} \frac{b}{h} \sum_{m=1,3,5,\dots}^{\infty} \frac{\tanh\left(\frac{m\pi h}{2b}\right)}{m^5} \right) \quad (3)$$

$$J_s = b h^3 \frac{1}{3} \left(1 - 0.63 \frac{h}{b} + 0.052 \left(\frac{h}{b} \right)^5 \right) \quad (4)$$

2.2. Bending vibrations

The equation of motion of a bending vibration of a beam based on the assumption of Bernoulli-Euler theory, for the case independent from the torsional one has the form (5), where: $w(x, t)$ – transversal displacement, E – Young modulus, J_y – moment of inertia of cross-section, A – area of cross-section.

$$\rho A \frac{\partial^2 w(x,t)}{\partial t^2} + E J_y \frac{\partial^4 w(x,t)}{\partial x^4} = 0 \quad (5)$$

The differential equation of the bending vibration (4) can be solved to find the values of natural frequencies and mode shapes after taking into account four boundary conditions. These can be formulated by giving the suitable values of:

- transversal displacement $w(x, t)$ for a given cross-section,
- slope angle $\varphi = -\frac{\partial w}{\partial x}$ for a given cross-section,
- value of bending moment $M_g = -EJ_y \frac{\partial^2 w}{\partial x^2}$ for a given cross-section,
- value of shear force $T = -EJ_y \frac{\partial^3 w}{\partial x^3}$ for a given cross-section.

3. Natural vibrations of a beam

3.1. General case

The easiest form of parametric presentation of the results of the analysis is a definition of the ratio $r_{(1)}^{(1)}$ between the lower value of natural frequency for torsional vibrations $\omega_t^{(1)}$ to the lower value of natural frequency for bending vibrations $\omega_g^{(1)}$. In general, the ratio $r_{(n)}^{(m)}$ is defined by (8), where $\lambda_t^{(m)}$ and $\lambda_g^{(n)}$ are parameters whose values depend on the type of boundary conditions of the beam under consideration, m is the mode number of torsional vibrations and n is the mode number of bending ones [5, 12]. The values for the natural frequencies of a beam can be determined based on formulas: (6) – for torsion and (7) for bending [5, 12].

$$\omega_t^{(m)} = \lambda_t^{(m)} \sqrt{\frac{GJ_s}{\rho J_0}} \quad (6)$$

$$\omega_g^{(n)} = (\lambda_g^{(n)})^2 \sqrt{\frac{EJ_y}{\rho A}} \quad (7)$$

$$r_{(n)}^{(m)} = \frac{\omega_t^{(m)}}{\omega_g^{(n)}} = \frac{\lambda_t^{(m)} l}{(\lambda_g^{(n)} l)^2} l \sqrt{\frac{G}{E}} \sqrt{\frac{J_s A}{J_0 J_y}} = \frac{\lambda_t^{(m)} l}{(\lambda_g^{(n)} l)^2} l \sqrt{\frac{1}{2(1+\nu)}} \sqrt{\frac{J_s A}{J_0 J_y}} \quad (8)$$

3.2. Clamped-free beam with rectangular and circular cross-section

Bearing in mind practical applications in turbine blades, the case of a clamped-free beam with a rectangular cross-section is analysed in detail as an example. A beam with length l has the rectangular cross-section with width b and height h . Moreover, the circular cross-section with diameter D is considered for comparison of results. The boundary conditions for torsion have form (9) and for bending form (10).

$$\varphi|_{x=0} = 0, \quad \frac{\partial \varphi}{\partial x}|_{x=l} = 0 \quad (9)$$

$$w|_{x=0} = 0, \quad \frac{\partial w}{\partial x}|_{x=0} = 0, \quad \frac{\partial^2 w}{\partial x^2}|_{x=l} = 0, \quad \frac{\partial^3 w}{\partial x^3}|_{x=l} = 0 \quad (10)$$

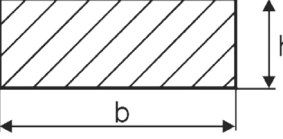
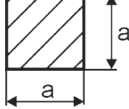
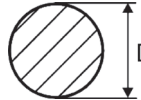
For this case, the values of $\lambda_i^{(1)}$ and $\lambda_g^{(1)}$ can be calculated from relationship (12). Values for the other cases can be found e.g. in [12]. Based on these formulas and relationship (4) for the three sections – rectangle, square and circle – the formula for ratio $r_{(1)}^{(1)}$ can be written in the forms given in Table 1 for material described by a Poisson ratio equal to $\nu = 0.29$ (e.g. steel, aluminium). For a rectangular cross-section, the non-dimensional parameter s (height/width) is useful for parametric description of the cross-section shape (11). Value $s = 1$ denotes a square cross-section.

$$s = \frac{h}{b} \quad (11)$$

$$\lambda_i^{(1)}l = 1.5708, \quad \lambda_g^{(1)}l = 1.8751, \quad \lambda_g^{(2)}l = 4.6941, \quad \lambda_g^{(3)}l = 7.854 \quad (12)$$

Table 1

Formulas for ratio $r_{(1)}^{(1)}$ for chosen cross-section shapes

SHAPE	FORM	RATIO $r_{(1)}^{(1)}$
RECTANGLE		$3.357 \frac{l}{\sqrt{b^2 + h^2}} \sqrt{\frac{1}{3} \left(1 - 0.63 \frac{h}{b} + 0.052 \frac{h^5}{b^5} \right)} =$ $3.357 \frac{1}{\sqrt{1+s^2}} \sqrt{\frac{1}{3} \left(1 - 0.63 s + 0.052 s^5 \right)} \frac{l}{b}$
SQUARE		$0.891 \frac{l}{a}$
CIRCLE		$1.119 \frac{l}{D}$

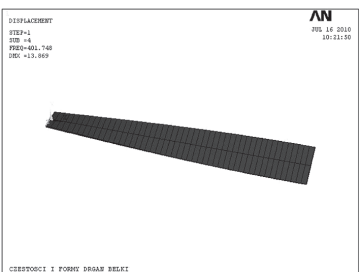
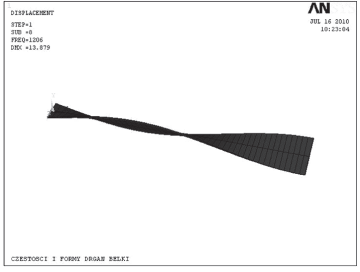
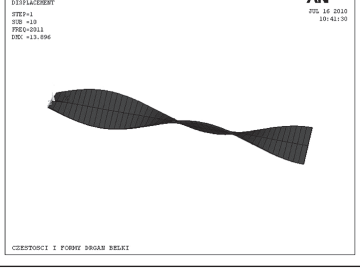
4. Analysis of existence of torsional modes in low frequency

4.1. FEM simulation

The simulations were performed for a free-fixed beam made of steel ($E = 2.1E + 11$ Pa, $\nu = 0.29$, $\rho = 7800$ kg/m³) with a length of 0.2 m and a rectangular cross-section (width 0.02 m, height 0.001 m). The length/width ratio is equal to ten, so the Bernoulli-Euler theory of bending can be applied. In the modal characteristic of the beam under consideration, there are two types of modes: bending (in two planes) and torsional. Only torsional modes are taken into account here.

Table 2

Natural frequencies of torsional vibrations for the analysed beam

MODE NO.	FREQUENCY [Hz]		MODE SHAPE
	THEORY	FEM	
1	397	402	 <p>DISPLACEMENT STEP=1 SUB =1 PRE=401,740 DRC =13,869</p> <p>AN JUL 16 2010 10:31:50</p> <p>CZESTOTLICZKI I FORMY DRGAN BELEK</p>
2	1191	1206	 <p>DISPLACEMENT STEP=1 SUB =1 PRE=4206 DRC =13,879</p> <p>AN JUL 16 2010 10:31:04</p> <p>CZESTOTLICZKI I FORMY DRGAN BELEK</p>
3	1985	2011	 <p>DISPLACEMENT STEP=1 SUB =1 PRE=4211 DRC =13,896</p> <p>AN JUL 16 2010 10:41:50</p> <p>CZESTOTLICZKI I FORMY DRGAN BELEK</p>

The first analysis was performed by applying the finite element package. The beam was modelled in the *Ansys* computer package using the *solid45* element.

The second results were obtained by the analytical formulas from the model discussed.

The values of the first three lowest natural frequencies of torsional type, obtained by the finite element method and analytical formulas, are given in Tab.1. These results are close to each other.

4.2. Influence of ratio height/width

The influence of the shape of the rectangular cross-section on the existence of torsional modes in the low frequency range is shown for the beam described above. The first three bending modes ($n = 1,2,3$), and the first torsional mode ($m = 1$) were taken into account. The independent parameter of the analysis was ratio s (height/width) – (9). Hence three functions were analysed – $r_{(1)}^{(1)}(s)$, $r_{(2)}^{(1)}(s)$, $r_{(3)}^{(1)}(s)$. The functions are shown in Fig.1.

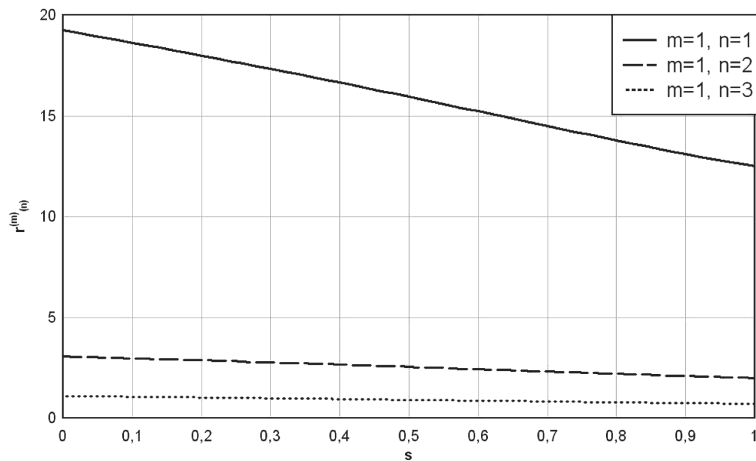


Fig. 1. Ratios $r_{(1)}^{(1)}(s)$ (top), $r_{(2)}^{(1)}(s)$, $r_{(3)}^{(1)}(s)$ (bottom) as functions of parameter s

It can be seen that the ratio for the first bending mode is much more than one for all values of parameter s . But for the third bending mode the ratio is approximately one. This means that the natural frequency for the third bending mode is almost the same as for the first torsional one for the beam with the geometry and material given.

4.3. Influence of length

The influence of the length of a rectangular cross-section on the existence of torsional modes in low frequency range is shown for the beam described above. The beam has a rectangular cross-section (width 0.02 m, height 0.001 m). The first three bending modes ($n = 1,2,3$), and the first torsional mode ($m = 1$) were taken into account. The independent

parameter in this analysis was length l (height/width). As above, three functions were analysed – $r_{(1)}^{(1)}(l)$, $r_{(2)}^{(1)}(l)$, $r_{(3)}^{(1)}(l)$. The functions are shown in Fig. 2.

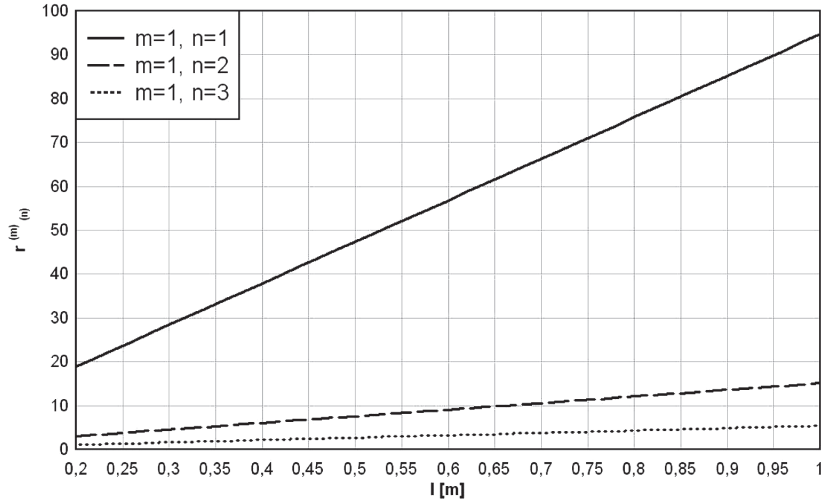


Fig. 2. Ratios $r_{(1)}^{(1)}(l)$ (top), $r_{(2)}^{(1)}(l)$, $r_{(3)}^{(1)}(l)$ (bottom) as functions of length l

It can be seen that the ratio for the first bending mode is much more than that for all values of parameter l . But for the third bending mode the ratio is approximately one for a short beam.

5. Conclusions

A fixed-free beam with a rectangular cross-section may exist in engineering structures, such as turbine blades. For some cross-section shapes, with an especially short length, the existence can be observed of torsional modes in the low frequency range for this beam.

For some cases of cross-sections, not analysed in the article, the theory of thin-walled beam must be applied in the analysis [1, 3–5, 9]. The rectangular cross-section type is not thin-walled for any values of the height/width ratio.

References

- [1] Augustyn E., Kozień M.S., *Analytical solution of excited torsional vibrations of prismatic thin-walled beams*, Journal of Theoretical and Applied Mechanics, vol. 54, no. 4, 2015, 991–1004.
- [2] De Rosa S., Marulo F., Lecce L, *The structural-acoustic analysis of coupled systems: some experiences for the prediction and control of the vibration and noise*, Proceedings of the Structural and Biomedical Acoustics, Vol. Structural Acoustics, Zakopane 1997, 39–48.

- [3] Gere J.M., *Torsional vibrations of beams of thin-walled open section*, Journal of Applied Mechanics – Transactions of the ASME, vol. 21, no. 4, 1954, 381–387.
- [4] Gere J.M., Lin Y.K., *Coupled vibrations of thin-walled beams of open cross section*, Journal of Applied Mechanics – Transactions of the ASME, vol. 25, no. 3, 1958, 373–378.
- [5] Kaliski S. (red.), *Drgania i fale. Mechanika Techniczna*, t. III, PWN, Warszawa 1974.
- [6] Kozień M.S., *Ćwiczenia laboratoryjne z miernictwa dynamicznego*, Wydawnictwo PK, Kraków 2000.
- [7] Łączkowski R., *Drgania elementów turbin cieplnych*, WNT, Warszawa 1974.
- [8] Nowacki W., *Dynamika budowli*, PWN, Warszawa 1976.
- [9] Piechnik S., *Mechanika techniczna ciała stałego*, Wydawnictwo PK, Kraków 2007.
- [10] Podgóński J., Błazik-Borowa E., *Wprowadzenie do metody elementów skończonych w statyce konstrukcji inżynierskich*, Lublin 2011.
- [11] Walczak J., *Wytrzymałość materiałów oraz podstawa teorii sprężystości i plastyczności*, tom II, PWN, Warszawa–Kraków 1978.
- [12] Woroszył S., *Przykłady i zadania z teorii drgań. Cz. 2 Układy ciągłe*, PWN, Warszawa 1984.

KRZYSZTOF DOBAJ*

INFLUENCE OF CAR WHEEL SUSPENSION PARAMETERS ON IMPROVEMENT OF ACTIVE SAFETY AND RIDE COMFORT

WPŁYW PARAMETRÓW ZAWIESZENIA KÓŁ SAMOCHODU NA POPRAWĘ BEZPIECZEŃSTWA CZYNNEGO I KOMFORTU JAZDY

Abstract

This paper deals with the simulation of car suspension parameter impact on the contact between the tyre and an uneven road. The simulation was based on the quarter car vehicle model used for the analysis of vertical vibrations of sprung and unsprung mass under the influence of discrete road unevenness. The parameters of the model relate to the front axle of a VW Passat B5. Suspension and damping characteristics were described by non-linear functions. The results included in the paper cover the influence of changing the rebound damping force, main spring stiffness coefficient and the unsprung mass on active safety and ride comfort.

Keywords: *vehicle vibrations, modelling, suspension, active safety, ride comfort*

Streszczenie

W artykule przeprowadzono symulacyjną analizę wpływu parametrów masowych, sztywnościowych oraz tłumieniowych zawieszenia koła samochodu na bezpieczeństwo czynne i komfort jazdy. Wykorzystano tzw. ćwiartkowy model pojazdu do analizy drgań pionowych masy nieresorowanej i resorowanej pod wpływem dyskretnych nierówności drogi. Parametry modelu dotyczą przedniej osi samochodu VW Passat B5. Charakterystyki resorowania i tłumienia opisano nieliniowymi funkcjami. W artykule zamieszczono wybrane wyniki analizy symulacyjnej dotyczące wpływu zmiany siły tłumienia amortyzatora w fazie odbicia, sztywności resorowania sprężyny głównej oraz masy nieresorowanej na wskaźniki bezpieczeństwa i komfortu jazdy.

Słowa kluczowe: *drgania pojazdów, modelowanie, resorowanie, bezpieczeństwo czynne, komfort*

DOI: [10.4467/2353737XCT.15.171.4376](https://doi.org/10.4467/2353737XCT.15.171.4376)

* MSc. Krzysztof Dobaj, Faculty of Mechanical Engineering, Cracow University of Technology (PhD Student).

1. Introduction

The suspension and damping characteristics of car wheel suspensions are chosen as a compromise between a number of requirements, such as: vibration comfort (isolation) [4, 5], durability of wheel suspension, and minimizing the time of separation between the tyre and the road surface [1]. In order to obtain the specific characteristics of the suspension and damping, often time-consuming cycles of road tests are conducted, usually using trial and error methods. The use of computer modelling allows us to improve and speed up the design process of the suspension elements [3, 5].

The aim of the simulation is to analyse the impact of changes in mass, stiffness and damping parameters of car wheel suspension on active safety (related to tyre cooperation with uneven road) and ride comfort. The simulation was based on a quarter car vehicle model used for the analysis of vertical vibrations of sprung and unsprung mass under the influence of discrete road unevenness. The model parameters cover the front axle of a VW Passat B5. Suspension and damping characteristics are described as non-linear functions. The subject of the analysis is discussed in more detail in [1].

2. Definition of the quarter car vehicle model

2.1. Physical scheme of the model

The model used for the analysis of vertical vibrations of the wheel-body set is a two-mass, non-linear model known as a quarter car vehicle model [2–4]. The scheme of the model is shown in Fig.1.

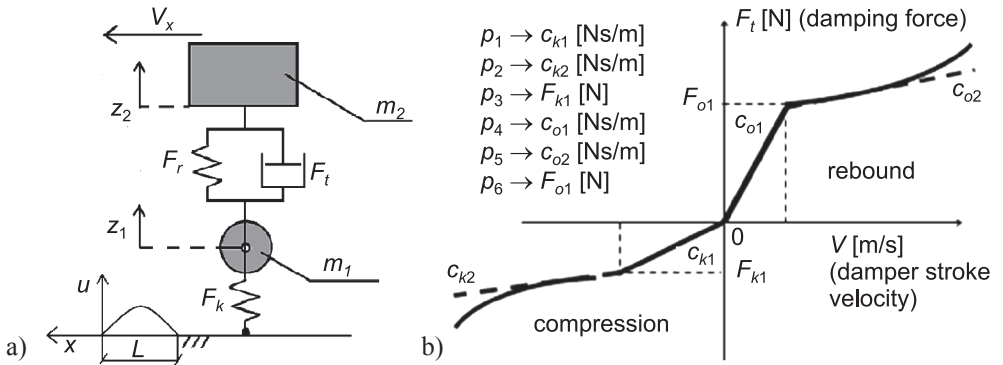


Fig. 1. a) Scheme of the quarter car vehicle model, b) damper characteristics used in the model

The model has two degrees of freedom (Fig. 1a), covering the vertical vibrations of the masses (m_1 and m_2). Coordinate z_1 is related to the vibration of unsprung mass (m_1). Coordinate z_2 is related to the vibration of the sprung mass (m_2). The model parameters are related to the damper which generates damping force F_r . Damper characteristics are

described by parameters $p_1 \dots p_6$, which refer to compression and rebound forces (F_{k1}, F_{o1}) and to coefficients which determine the slopes of damper characteristics ($c_{k1}, c_{k2}, c_{o1}, c_{o2}$). The description of these parameters is shown in Fig. 1b. Suspension elements which transfer the replacement force F_r , are described by, among others, the stiffness coefficient c_2 . The tyre, which only carries force normal to the surface (F_k) by point contact, is described by stiffness coefficient c_1 . The coefficient c_1 refers to a tyre of size 195/65 R15, with a pressure of 2.3 bar. Profile (u) of the unevenness (a hump), which has a certain length and height, is shown in Fig. 1a.

Table 1

Base values of the model parameters involved with the front axle of VW Passat [3]

$m_1 = 45$ [kg] (unsprung mass)	$p_2(c_{k2}) = 1433$ [Ns/m] (damp. coeff. (Fig.1b))
$m_2 = 495$ [kg] (sprung mass)	$p_3(F_{k1}) = 742$ [N] (damper compression force)
$c_2 = 78\,000$ [N/m] (spring element stiffness)	$p_4(c_{o1}) = 3120$ [Ns/m] (damp. coeff. (Fig.1b))
$c_1 = 260\,000$ [N/m] (tyre radial stiffness)	$p_5(c_{o2}) = 623$ [Ns/m] (damp. coeff. (Fig.1b))
$p_1(c_{k1}) = 14070$ [Ns/m] (damping coefficient (look Fig. 1b))	$p_6(F_{o1}) = 2053$ [N] (damper rebound force)

2.2. Assumptions for the analysis

The simulation model was based on the following simplifying assumptions [3]:

- 1) movement of the vehicle is a constant speed (V_x) and a straight line motion,
- 2) vertical oscillations with frequencies up to several Hz were analysed,
- 3) the road surface is non-deformable,
- 4) simulation runs were performed for road unevennesses with smooth and symmetric profiles,
- 5) the effects of aerodynamics and the influence of the brake system and powertrain were omitted,
- 6) the hysteresis of the damper and spring was omitted.

The base values of the model parameters equalled the front axle of a stock, unmodified VW Passat. The numerical data of the masses and the wheel suspension is included in Tab. 1.

2.3. Equations of the vehicle motion

In order to analyse the vertical vibrations of the wheel-body system the following equations were formulated describing the motion of the masses in the model (Fig. 1):

$$m_1 \ddot{z}_1 + F_k(z_1 - u) + F_r(z_1 - z_2) + F_t(\dot{z}_1 - \dot{z}_2) = 0 \quad (1)$$

$$m_2 \ddot{z}_2 + F_r(z_1 - z_2) + F_t(\dot{z}_2 - \dot{z}_1) = 0 \quad (2)$$

where:

- m_1, m_2 – unsprung and sprung mass,
- z_1, z_2 – vertical displacements (vibration components) of unsprung and sprung mass,
- F_k – the force transmitted through the tyre,
- F_r – the force transmitted through spring elements,
- F_t – damping force of the shock absorber,
- u – road profile described in relation to the distance travelled x .

2.4. Evaluation of ride comfort and active safety

The model's response under the influence of the uneven road was evaluated according to the criteria of comfort and active safety. Comfort criteria (K1 to K5) are associated with the vertical vibration of the sprung mass where the passenger seats are mounted (Fig. 2). The driving comfort criteria analysed in the paper are: maximum, minimum, and root mean square value of the body vertical acceleration (a_z), the RMS value of the body jerk (K4) and maximum vertical body displacement z_2 (K5).

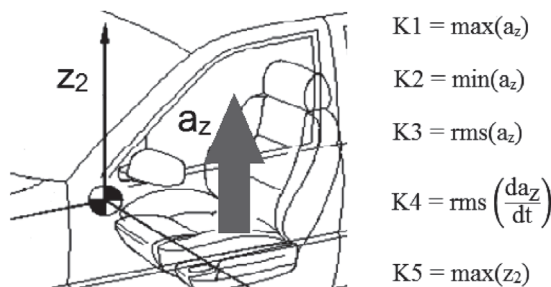


Fig. 2. Description of the driving comfort criteria

Criteria of active safety (B1 to B3) are associated with the normal tyre force (F_k) (unsprung mass element) with respect to the road (Fig. 3). Changes in that force causes changes in the tyre adhesion force to the road surface. In these circumstances, the vehicle response to acceleration, deceleration or change of direction forced by driver may be different than expected. Active safety criteria used in the analysis are: the RMS value and maximum of the force F_k and the time when the wheel lost contact with the road surface (criterion B3).

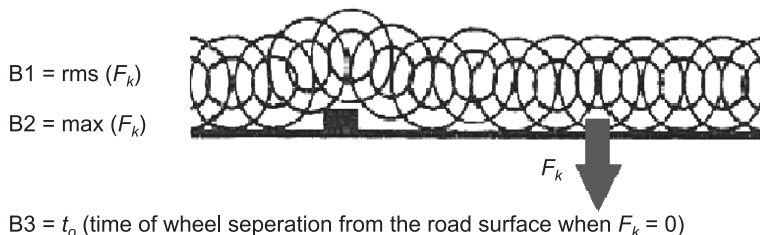


Fig. 3. Description of active safety criteria

3. Simulation analysis

For the analysis, Matlab simulation software was used. Five simulation scenarios were defined [1]. The results submitted in this section are compared with passing through a pothole (with a length of 1 m and a depth of 0.05 m) with a speed of 100 km/h and 50 km/h and also with passing through a bump (with a length of 1 m and a height of 0.05 m) with a speed of 100 km/h.

Scenario 1: bump, 100 km/h, influence of damper rebound force

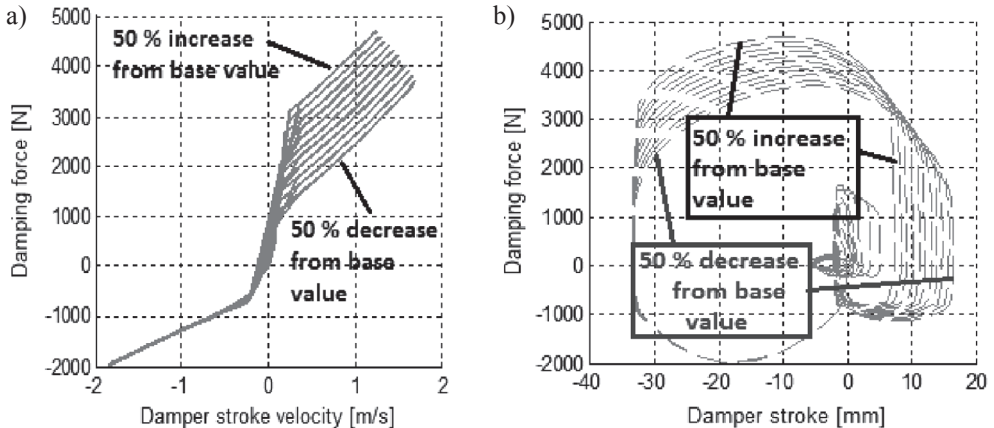


Fig. 4. Influence of damper rebound force change on damper characteristics: a) relation between damping force and damper stroke velocity, b) relation between damping force and damper stroke

The damper rebound force was varied within $\pm 50\%$, which was encoded in the range of -1 to 1 , where 0 is the base value of the parameter. The base value refers to a brand new shock absorber, without regulation. Fig. 4a and Fig. 4b show the influence of the rebound damping force change on the established damper characteristics. The relationship between the damping force and the damper stroke velocity is shown in Fig. 4a. Positive ranges of the damping force and the damper stroke velocity refer to the rebound motion of the car's suspension. On the other hand, the negative ranges of the damping force and the damper stroke velocity refer to the opposite direction of car suspension motion (compression). The change of the parameter affects the part of characteristics shown in Fig. 4a which refers to the positive range of damper stroke velocity. The rebound damping force increased by 50% from the base value determines a maximum of damping force of about 4500 N and maximum of damper stroke velocity about 1.25 m/s. When the rebound damping force is decreased by 50% from the base value, the maximum damping force is about 3500 N and corresponds to a maximal value of damper stroke velocity of about 1.75 m/s. When the damper rebound force is increased, the maximum damper stroke velocity takes smaller values. It is provoked by increased suspension movement resistance caused by greater damper rebound force.

The relationship between the damping force and the damper stroke is shown in Fig. 4b. Positive ranges of the damping force and the damper stroke correspond to the rebound

motion of the car's suspension and negative ranges refer to the suspension compression. The damper rebound force change affects the positive ranges of the values shown in Fig. 4b. Greater suspension movement resistance (caused by an increased damper rebound force) results in reduced damper stroke. The maximum damping force (about 4500 N) occurs when the damper parameter is increased by 50%. The line of the damping force at about 4500 N passes into the line of damper stroke about 8 mm (to the right of Fig. 4b.) The minimum damping force (about 3500 N) occurs when the damper rebound force is decreased by 50%. The line of the damping force at about 3500 N passes into the line of damper stroke at about 16 mm.

The driving comfort and active safety criteria were also normalized, so that a value of 1 corresponded to the base values of parameters. The reduction of that value corresponds to an improvement in the wheel-car body system qualities and an increase in that value refers to deterioration of the criteria under consideration. For example, the value Criteria K = 1.1 refers to the deterioration of the comfort criterion by about 10%. On the other hand, the value Criteria B = 0.95 shows an improvement in the ride comfort criterion by about 5%.

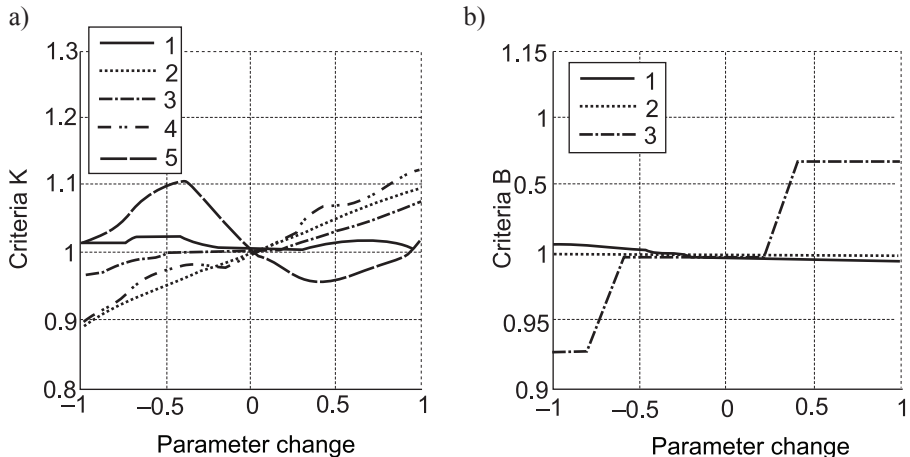


Fig. 5. Influence of the rebound damping force change in scenario no. 1 on the criteria:
a) K-ride comfort, b) B-active safety

In this scenario, the increase in the rebound damping force provokes a deterioration in four of the five comfort criteria analysed (Fig. 5a). Only the maximum of body vertical displacement (criterion K5) shows irregular change. The maximum normal tyre force (criterion B2) does not depend on the change in rebound damping force, which is shown in Fig. 5 b. The RMS value of normal tyre force shows negligibly small changes. The criterion which depends on the parameter change most of all is the period of wheel separation from the road surface (criterion B3). When the rebound damping force is greater, the wheel separation time is longer (Fig. 5a).

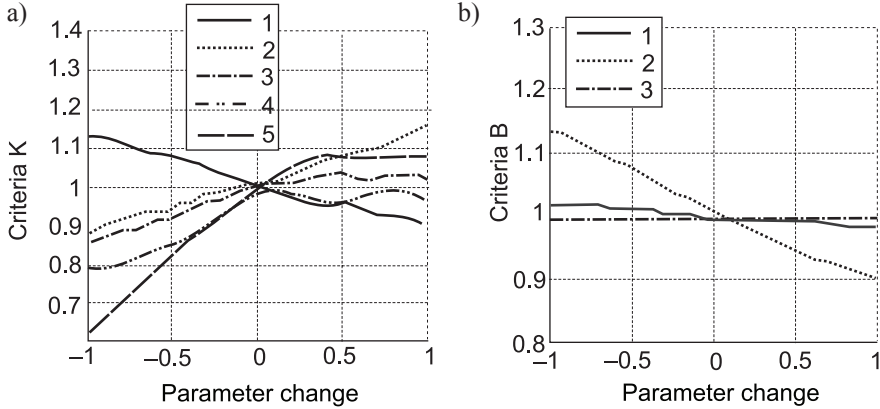
Scenario 2: pothole, 100 km/h, influence of damper rebound force


Fig. 6. Simulation scenario no. 2- influence of the rebound damping force change on the criteria:
a) K-ride comfort, b) B-active safety

Increasing the rebound damping force provokes deterioration in four of five of the comfort criteria analysed (Fig. 6a). Only criterion K1 (maximum of body vertical acceleration) shows an improvement. The RMS value of normal tyre force (criterion B1) decreases when the rebound damping force is greater. However, the amount of change in this criterion is inconsiderable (Fig. 6b). The maximum normal tyre force also decreases, but change in this criterion is significant. According to Fig. 6b, the difference between maximum and minimum values of criterion B2 obtained is about 25%. In scenario 2, time of wheel separation from the road surface does not depend on a change in the rebound damping force.

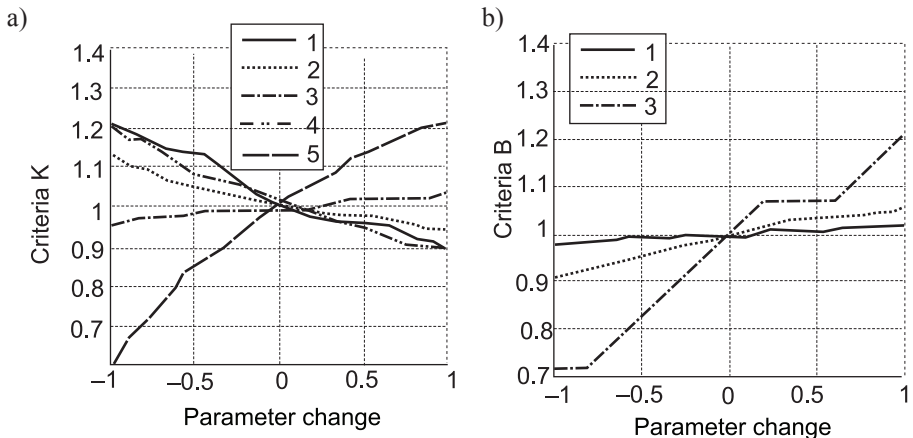
Scenario 3: bump, 100 km/h, influence of unsprung mass


Fig. 7. Influence of the unsprung mass change in scenario no. 3 on the criteria: a) K-ride comfort,
b) B-active safety

In the case of scenario 3, increasing the rebound damping force provokes improvement in the maximum and minimum vertical body acceleration (criteria K1 and K2 respectively) and the RMS value of body vertical jerk (criterion K4). This is shown in Fig. 6a. The RMS value of body vertical acceleration (criterion K3) and maximum of body vertical displacement (criterion K5) show deterioration (increase). The changes in criterion K3 are inconsiderable, but the increase in the maximum body vertical displacement is prominent. The difference between the maximum and minimum value of this criterion obtained is about 50%.

Increase in the rebound damping force provokes a deterioration in all the active safety criteria. The criterion which shows the most significant deterioration is the period of wheel separation from the road surface (B3). A greater rebound damping force provides resistance which slows damper rebound motion when the wheel is separated from the road surface. In these conditions, the period of wheel separation from the road surface is extended.

Scenario 4: pothole, 100 km/h, influence of unsprung mass

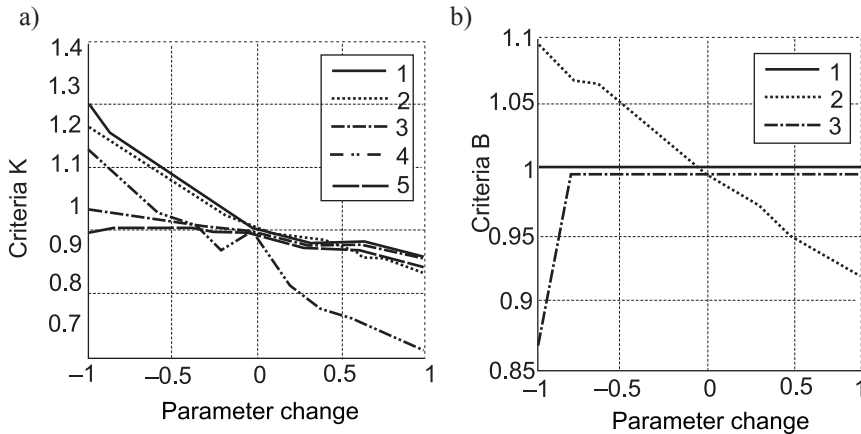


Fig. 8. Simulation scenario no. 4- change of the criteria: a) K-ride comfort, b) B-active safety in accordance with unsprung mass change

In this scenario, all the active safety criteria show improvement when the unsprung mass is increased (Fig. 8a). The criterion whose value is minimized the most is the RMS value of body jerk (K4). The difference between maximal and minimal values for this criterion is about 30%. In the case of maximum and minimum vertical body acceleration (criteria K1 and K2 respectively) this difference is about 15%. Criteria K3 and K5 (respectively the RMS value of body vertical acceleration and maximum of body vertical displacement) show comparatively small improvement.

When the unsprung mass is greater, the maximum normal tyre force (criterion B2) shows a significant decrease (improvement). This is shown in Fig. 8b. In scenario no. 4, the RMS value of this force does not depend on the unsprung mass change. When the unsprung mass is reduced by 50% compared to the base value, the period of wheel separation from the road surface (criterion B3) is comparatively beneficial. However, when the unsprung mass is further increased, this criterion does not depend on this parameter change.

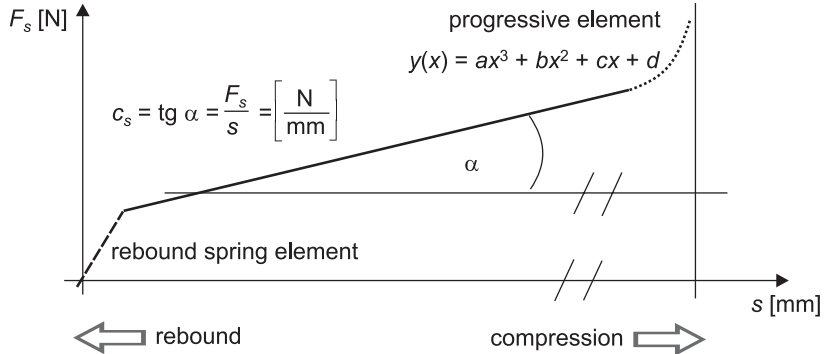
Scenario 5: pothole, 50 km/h, influence of spring elements stiffness


Fig. 9. The suspension characteristics

The suspension element in the front axle of a VW Passat B5 consists of three components, which act in different ranges of suspension movement (Fig. 9). In the largest part of the suspension travel (solid line in Fig. 9), the relation between the suspension force and suspension movement is linear. In this range of suspension travel the main spring element functions, described by its stiffness coefficient c_s . The suspension stiffness coefficient is equal to the tangent of the angle between the blue line of suspension characteristics and the horizontal axis. In the front suspension of a VW Passat B5, the main spring element is a coil spring. In the final phase of the rebound movement (dashed line in Fig. 9), the suspension stiffness coefficient achieves a larger value. This is provoked by the additional rebound spring element. In the final stage of the suspension compression (dotted line in Fig. 9), the progressive element acts. Its characteristics are described in the numerical model by a polynomial of the third degree. The model parameter changed in this scenario is the suspension stiffness coefficient c_s .

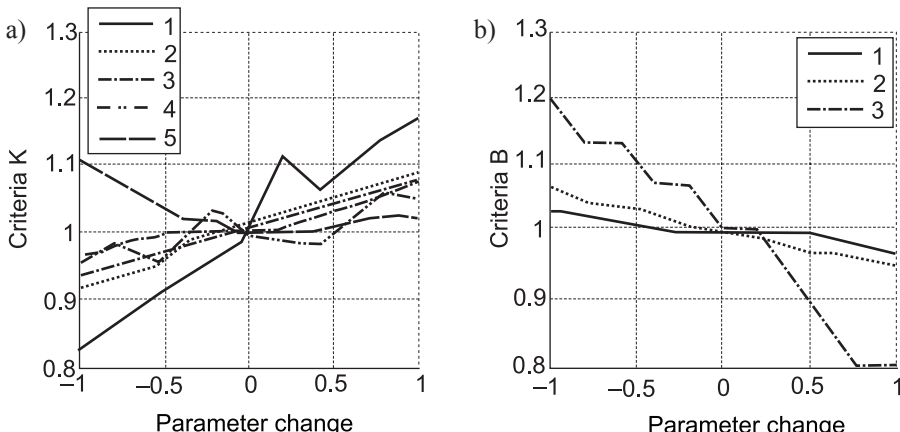


Fig. 10. Scenario 5: influence of spring elements stiffness change on criteria: a) K-ride comfort, b) B-active safety

An increase in spring element stiffness provokes deterioration in four of the five comfort criteria obtained (Fig. 10a). A large spring element stiffness causes resistance on wheel vertical movement under the influence of an uneven road. For this reason, the vibrations provoked by the uneven road are largely transferred to the car's body. In this simulation scenario, only criterion K5 (maximum of body vertical displacement) shows irregular changes.

A spring element which has a large stiffness has a tendency to rebound rapidly after taking the load off. This quality is confirmed in Fig. 10b and results in significant improvement in the period of wheel separation from the road surface (criterion B3). Criteria B1 and B2, involved with normal tyre force (its maximum and RMS value), are also improved. However, this improvement is less significant.

4. Conclusions

The results obtained confirm the contradiction between the analysed criteria of comfort and active safety which occurs in most of the simulation cases [1]. An increase in damper rebound force provokes deterioration in the considered ride comfort criteria in most simulation cases. At the same time, an increase in this parameter provides an improvement in the most active safety criteria [1]. An increase in the unsprung mass results in deterioration in the comfort criteria and active safety criteria. When the spring element stiffness is increased, comfort criteria take less beneficial values, but active safety criteria are improved.

The relationships between the criteria considered are not smooth because of the nonlinearities that occur in certain model response conditions. Due to the large number of independent parameters and variety of simulation scenarios, the selection of specific settings (e.g. in order to maximize active safety) is a very complex issue. This problem is difficult to solve without appropriate optimization algorithms [3, 5].

References

- [1] Dobaj K., *Assortment of car wheel suspension parameters for improving the contact of tyre with uneven road*, Engineering thesis, Faculty of Mechanical Engineering, Cracow University of Technology, 2013.
- [2] Gobbi G., Mastinu G., *Analytical description and optimization of the dynamic behaviour of passively suspended road vehicles*, Journal of Sound and Vibration (2001) 245(3), 457–481.
- [3] Maniowski M., *Damping characteristics optimization of a car shock absorber in conditions of passing over a single unevenness*, Materials of the Symposium „Influence of Vibrations on Environment”, Janowice 2010.
- [4] Mitschke M., Wallentowitz H., *Dynamik der Kraftfahrzeuge*, 4. Auflage, Springer Verlag, Berlin/Heidelberg 2004
- [5] Goncalves J., Ambrosio J., *Optimization of Vehicle Suspension Systems for Improved Comfort of Road Vehicles Using Flexible Multibody Dynamics*, Nonlinear Dynamics 34, 113–131, 2003.

PIOTR DOBRZANIECKI*

ACTIVE SYSTEM FOR CONTROL OF OPERATIONAL PARAMETERS OF MINE DIESEL LOCOMOTIVE DRIVE

AKTYWNY SYSTEM KONTROLI PARAMETRÓW PRACY UKŁADU NAPĘDOWEGO GÓRNICZEJ LOKOMOTYWY SPALINOWEJ

A b s t r a c t

Requirements for better reliability, durability and effectiveness of the suggested means of transportation make the need of using state-of-the-art control systems and the system managing the work of the various vehicle components, such as the engine, brakes, etc. ABS, ASR, ESP and other systems are well known and widely used in the automotive industry. The traction control systems, eliminating the negative phenomena in the transient operation of driving systems are also met in rail vehicles. As there are no such solutions for narrow-gauge railway vehicles, including those used in mining plants, the system for control of operational parameters of the driving system of a mine diesel locomotive is suggested. The method for measurements of vehicle speed is indicated and use of these data in an adaptive system which adapts the operation of the driving system to the current contact conditions between wheel and rail is indicated.

Keywords: *diesel drive, mine rail locomotive, traction control system*

S t r e s z c z e n i e

Rosnące wymagania odnośnie do niezawodności, trwałości i efektywności proponowanych środków transportowych powodują, że niezbędne jest stosowanie nowoczesnych systemów sterujących i zarządzających pracą poszczególnych układów pojazdu, takich jak silnik spalinowy, układ hamulcowy itp. Powszechnie znane i stosowane w motoryzacji są układy typu ABS, ASR, ESP i inne. Również w pojazdach szynowych spotyka się układy kontroli trakcji, zapobiegające niekorzystnym zjawiskom w stanach nieustalonych pracy układu napędowego. Wobec braku tego typu rozwiązań, przeznaczonych do wąskotorowych pojazdów szynowych, w tym tych stosowanych w zakładach górniczych, zaproponowano opracowanie systemu kontroli parametrów pracy układu napędowego, przeznaczonego dla górniczej lokomotywy spalinowej. Wskazano sposób realizacji pomiaru prędkości pojazdu i zaproponowano wykorzystanie tych danych w adaptacyjnym układzie dostosowującym pracę układu napędowego do aktualnych warunków współpracy koła z szyną.

Słowa kluczowe: *górnictwo, napęd spalinowy, górnicza lokomotywa spalinowa, system kontroli trakcji*

DOI: 10.4467/2353737XCT.15.172.4377

* Ph.D.Piotr Dobrzaniecki, Division of Roadway Systems Institute of Mining Technology KOMAG, Gliwice, Poland.

1. Introduction

Active systems for controlling traction parameters are commonly used in transportation, especially in the mining industry. ABS, ASR, ESP and other systems are examples. These systems increase effectiveness of operation of drive transmission during both acceleration and braking. The traction control systems also enable limiting the overload of driving systems through active adaptation of applied torque to the momentary possibilities of its transmission to the carriageway. The ABS system can also be used in rail vehicles. However, so far such systems have not been used in driving the machines such as the narrow-gauge locomotives used in mining plants. Suggestions for solutions to an active system for the control of traction parameters on the example of a Lds-100 mine rail locomotive are given.

2. Systems for control of traction parameters of rail vehicles

Systems which increase the efficiency of transmission of traction torque and braking forces to the carriageway are commonly used in the automotive industry. Cars have advanced systems for control of transition parameters, which enable intervention regarding transmission of forces in the driving system. Advanced control systems enable selective control of operational parameters of each wheel (braking, reduction of applied torque), which improves significantly drive efficiency and safety. ABS (anti-lock braking system) or ASR (acceleration slip regulation) are examples. These systems (ASR acceleration slip regulation system and analogous TCS, ASC+T and other systems) maintain the neutral traction properties of the vehicle (especially steering ability) by intervention in a degree of transmission of driving force and braking force by each wheel (in the latest version of the systems). ABS, in cooperation with other systems enables control over the vehicle during manoeuvring on slippery surfaces and keeping the required track.

The problem of maintaining the vehicle on the route when its speed and load is within the limits does not apply to rail vehicles. However, in this case, some wheel slippage can occur during acceleration and wheels can be blocked with slippage during braking. When wheels are blocked during braking they can be locally worn out deforming the rings. As a consequence of frequent blockage of wheels earlier repairs of locomotive wheels are required.

Manufacturers of locomotives intended to be used on tracks of width $S = 1435$ mm offer advanced control and diagnostics systems in their new products. Such advanced systems enable full automation of the locomotive with keeping the speed set by the operator, as well as control of start-up, acceleration and braking operations through an anti-slippage system with individual action on each wheel and with adjustment of braking force. The GRIFFIN and DRAGON locomotives presented in Fig. 1 and 2 are examples.

In the GRIFFIN locomotive, the driving system with two two-axle carriages in Bo'Bo' arrangement is used. In the case of the DRAGON locomotive the driving system has two three-axle carriages in Co'Co' arrangement with an individual drive for each axle [1]. Analysis of the parameters of each motor's power supply as well as the individual character of the drive enable the state of each axle to be determined and, in connection with information about electric parameters, we are provided with complete data about the transmission of drive torque and braking force. Such a solution increases the effectiveness of machine operation



Fig. 1. GRIFFIN electric locomotive manufactured by NEWAG Group [1]



Fig. 2. DRAGON electric locomotive manufactured by NEWAG Group [1]

and also limits overloads and protects against excessive wear of the components which as a result increases the reliability and life of the entire system.

In locomotives used in the mining industry there are no solutions that would prevent against slippage during acceleration or braking. Only hydrostatic braking in the case of hydraulic motors and electrodynamic braking in electric motors are possible. Recovery of energy during braking is possible, when the motors operate in generator mode; however, slippage is still possible. In the case of a hydro-mechanical drive transmission, proper selection of diesel engine and hydrokinetic gear enable reducing the slippage during start-up, but cannot eliminate blocking of wheels during braking. Further in the paper, the drive of a mine diesel locomotive is presented, as well as the method of speed measurement, and new solutions increasing the efficiency of traction torque transmission are given.

3. Lds-100 locomotive driving system

The Lds-100 locomotive has a hydro-mechanical system for drive transmission which is presented in Fig. 3.

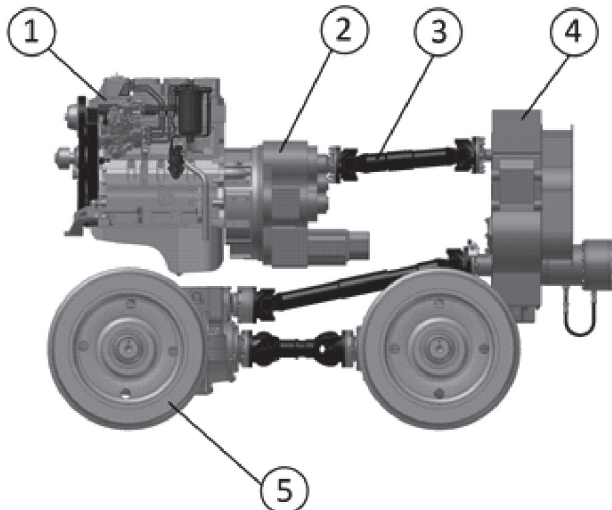


Fig. 3. Diagram of Lds-100K-EMA locomotive driving system [6]

where:

- 1 – Diesel engine
- 2 – Hydrokinetic gear
- 3 – Jointed shaft
- 4 – Reversible gear
- 5 – Wheel sets with a gear

Driving torque in the diesel engine is transmitted by jointed shafts through a hydrokinetic gear, reversible gear and intersecting axis gear of wheel sets. There is no differential gear in wheels (pos. 5) what means that all wheels have the same rotational speed. The linear speed of the locomotive is determined using an inductive sensor installed on the reversible gear's body. A special disk, revolutions of which are recorded by a sensor, is installed on the shaft flange. Information about the revolutions is transmitted to the locomotive control system and, after taking the velocity ratio for the place of the sensor installation into account, it is displayed on the operator's control panel as the locomotive speed. This information is also sent to the control system. Control only of rotational speed does not give the full information required to determine the condition of the system. In the case of slippage, which is controlled by the operator in a limited way, there are dynamic overloads to the drive system and that speeds up wear of its components (shafts, gears) and reduces the efficiency of driving system. In this case, much depends on how the vehicle is run by the operator. The efficiency of using operational parameters of the machine depends on the driver's strategy. Slippage during vehicle start up also overloads the hydrokinetic element and increases the temperature of the

working medium, which reduces its efficiency. Increase in the temperature of the working medium in the hydrokinetic gear has a negative impact on its lifespan. The adaptability of a system equipped with traction control parameters and active mechanisms supporting the operator would increase the safety and reliability of the machine. Due to the fact that there are no practical solutions of the systems for identification of operational parameters, the paper presents a suggested system, which, by comparison of two independently determined vehicle speeds, would identify frictional coupling between wheels and rail and would control the actuating components of the driving system to adapt operational parameters (engine rotational speed, braking force) to the actual conditions.

4. System for control of traction parameters of mine diesel locomotive

The suggested active system for the control of traction parameters is based on the comparison of two vehicle speeds determined in relation to two reference systems. A schematic diagram of the system is presented in Fig. 4. The suggested method is a universal one and after some adaptation, it can be applied in vehicles with different driving systems.

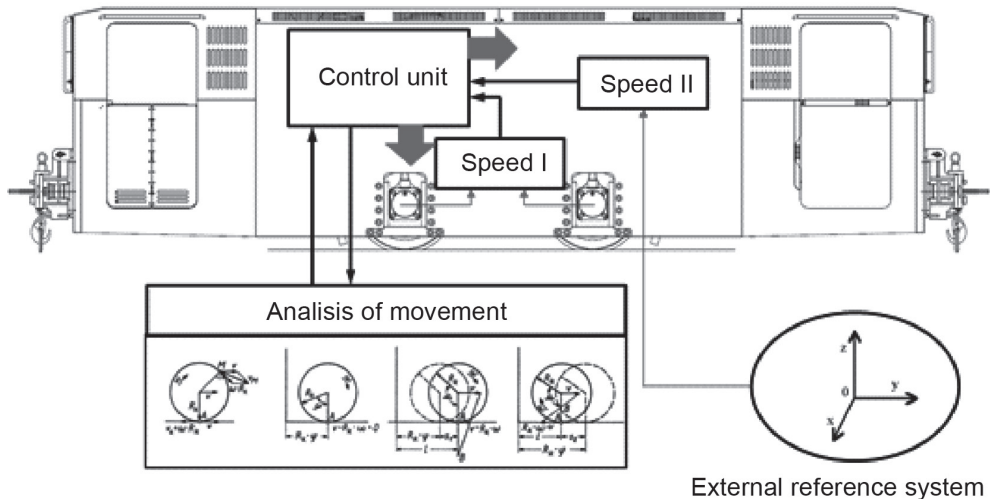


Fig. 4. Schematic diagram of the system for control of traction parameters

The principle of its operation is based on the simultaneous measurement of rotational speed in the selected place of the driving system as well as the linear speed of the vehicle in relation to the reference systems (objects on the carriageway on which the vehicle moves). Transformation of rotational speed in the driving system to the linear speed of the vehicle (using the right gear ratio) and its comparison with the linear speed measured in relation to the reference systems enable identifying movement condition according to the following criteria:

- $[n_1 \Rightarrow v_1] > v_2$ – slippage of driving wheels,
- $[n_1 \Rightarrow v_1] = v_2$ – stable operation,
- $[n_1 \Rightarrow v_1] < v_2$ – slippage of driving wheels,

where:

- n_1 – rotational speed in the driving system,
- v_1 – linear speed of the vehicle, determined from the rotational speed in the driving system,
- v_2 – linear speed of the vehicle measured directly.

Identification of the real condition of the driving system is the input information to be used in controlling the traction parameters by actuating systems, responsible for engine operational parameters (rotational speed) and braking parameters.

In Fig. 5 the concept of the model system for the analysis of an active system for control of traction parameters is given.

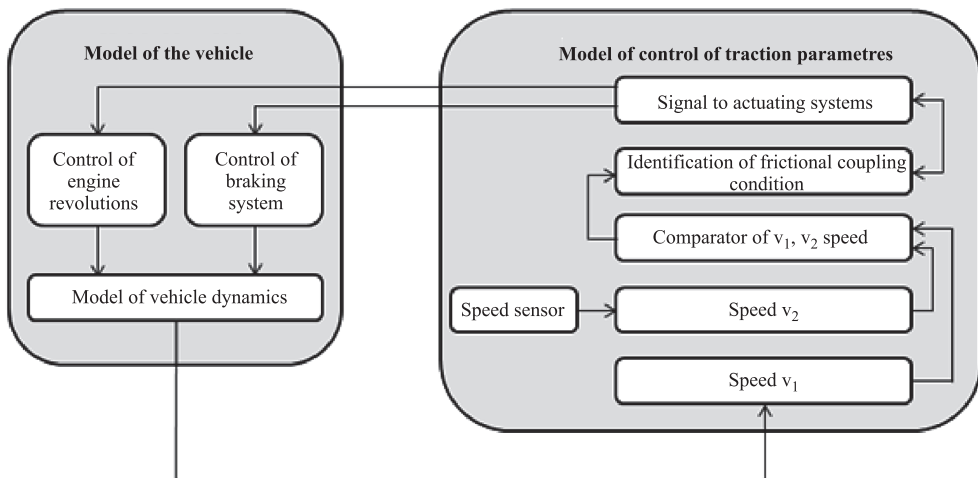


Fig. 5. Model of the system for control of traction parameters cooperating with a rail vehicle

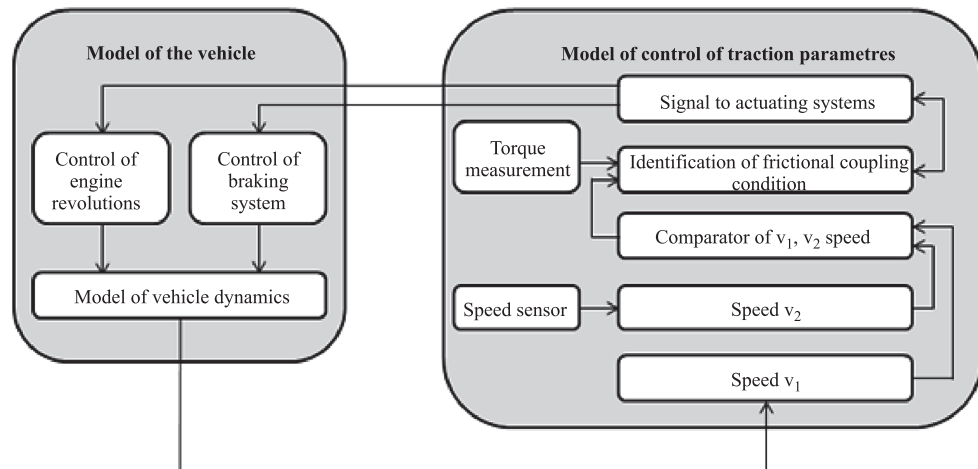


Fig. 6. Model of the system for control of traction parameters cooperating with a rail vehicle.
Version with a torque sensor

The suggested model of the system for control of traction parameters can also be connected with a torque sensor installed in the vehicle driving system that enables better analysis of the drive transmission system. A schematic diagram of the model system is given in Fig. 6.

The manner of using the torque sensor in the locomotive driving system is explained in [4].

The system can be developed by use of special software e.g.:

- MATLAB/Simulink,
- packet ANSYS,
- MSC ADAMS.

Tests of each solution of the control system will be carried out using the model system. It will enable the required corrections to be made, system tuning and optimization as regards its required parameters considering limitations resulting from features of the vehicle, actuating components, controlled objects and control-and-measuring instruments.

5. Method of additional speed measurements

An optical sensor placed over the rail head is planned to be used to determine v_2 speed (as in Fig. 5 and 6). The suggested method of speed measurement is used among others to determine the movement of rolled metal sheets. A simplified method of the optical sensor operation is shown in Fig. 7.

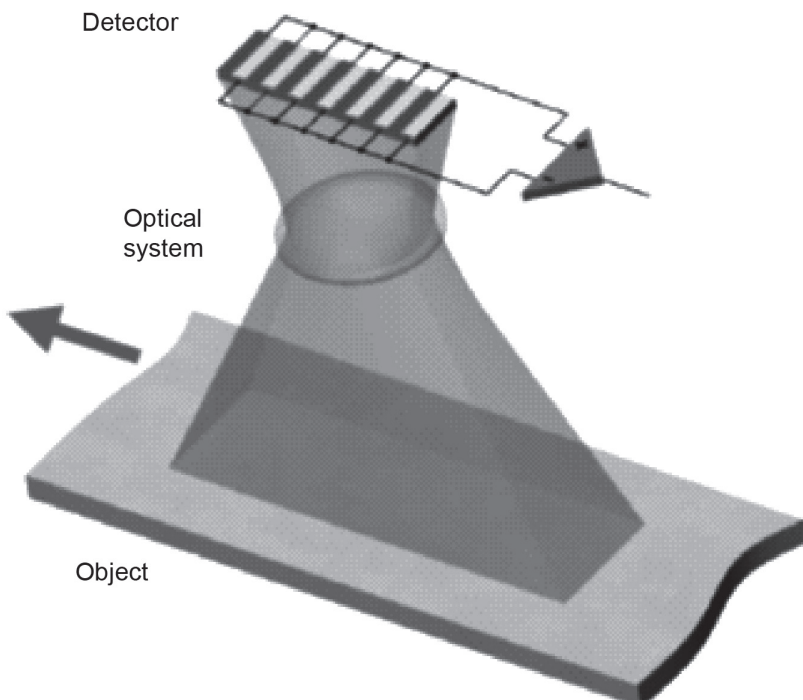


Fig. 7. Method of optical sensor operation [2]

Measurement of speed with use of the abovementioned sensor requires its installation in a place, where its proper operation is possible. In the case of an underground locomotive additional lightening may be required to improve sensor operation. The recommended method of sensor assembly is given in Fig. 8.

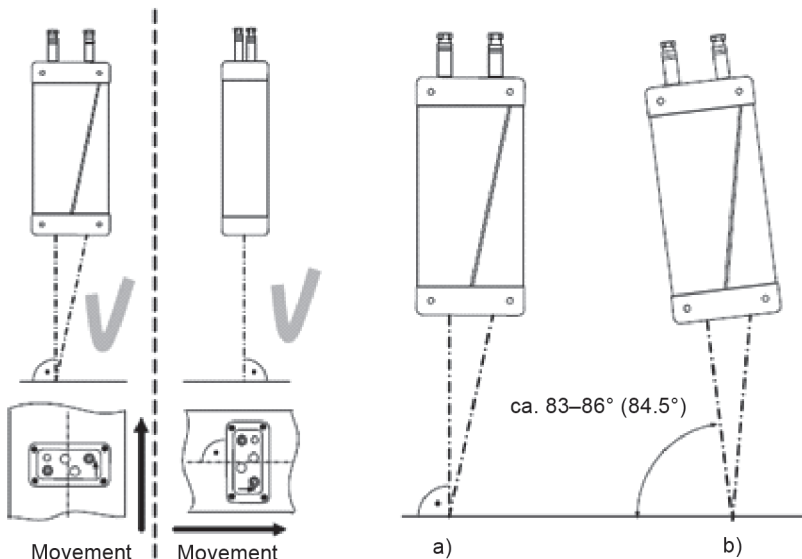


Fig. 8. Recommended method of the optical sensor assembly [2]

In the case of harsh operational conditions, the offered sensors are equipped with protective enclosures. Micro-Epsilon's device is an example [2].



Fig. 9. Sensor's protective enclosure made of stainless steel [2]

The usability of modules, which are available on the market and used also for positioning of quadcopter units, should be indicated. An example of the PX4FLOW module is described in [3]. The module is offered as presented in Fig. 10.

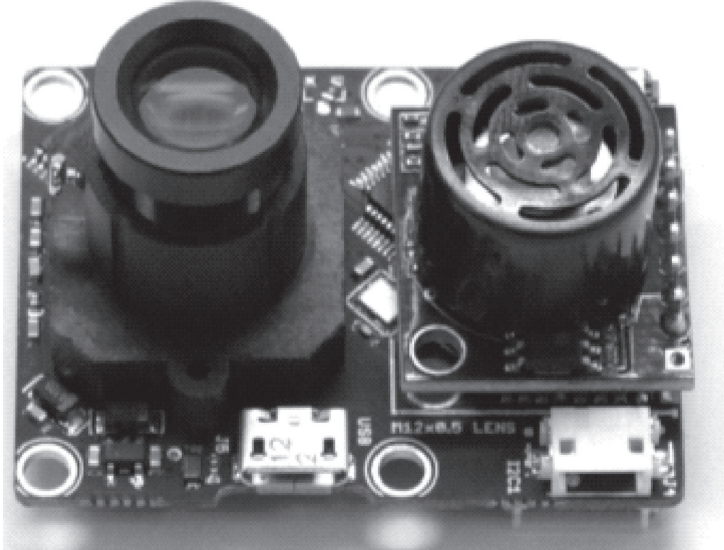


Fig. 10. Module PX4FLOW [3]

It is also possible to use other sensors, which have a similar principle of operation, e.g. use the optical sensor of a computer mouse [3]. However, it requires verification tests to confirm their usability in the specific conditions, as well as to select indispensable additional equipment such as lighting or an air nozzle to clean the lenses of object glasses.

6. Potential advantages of the developed system

Because the suggested solution does not have its equivalent in the state of the art, its advantages go beyond the product's quality improvement. Damage to drive transmission systems is the main reason for the failure of vehicles used in transportation. Slippage and overload of the driving system, occurring during acceleration and braking, is the main reason of such damage. Traction conditions of the drive system should be monitored to avoid such situations. Reduction of overloads to the drive system can increase its reliability and reduce the costs of maintenance of the transportation vehicle. Improved efficiency of the drive transmission system also increases the operational safety.

Total elimination of unwanted occurrences would result in the reduction of operational costs associated with replacement of damaged components of the drive system. Total costs are not only the cost of components but also servicing costs and the cost of breakdowns. Repair services made during locomotive operation concern the following components:

- hydrokinetic gear,
- jointed shafts,
- reversible gear,
- gears at wheel sets,
- rims of wheel centres.

Elimination of unwanted conditions in the drive system, like slippage, can increase its life and improve its reliability. Additionally it can reduce the operation of engine at highest operational parameters (revolutions, fuel consumption). Automatic adaptation of engine operational parameters (revolutions, fuel consumption) to the actual conditions (transported load, parameters of wheel-rail coupling, inclination) will enable avoiding the engine operation at too high power. In the case of a drive system without control of traction parameters, too high power generates too high torque, which in consequence causes a break in wheel adhesion and driving force is lost. Higher fuel consumption is an additional disadvantage as the quantity of harmful substances in exhaust gases emitted to the work environment increases. Thus, it is recommended to develop a technical solution that would eliminate these disadvantageous conditions in drive system operation.

7. Summary

The method for using the additional measuring equipment described in the paper is the first stage of the project aimed at developing an innovative system for controlling traction parameters, intended to be used in mine rail vehicles. Proper operation of the suggested optical sensors and the use of carriageway objects as the reference system will enable them to be used in an active system for the control of traction parameters. In addition to the measurable benefits resulting from the elimination of disadvantageous traction conditions with overload to drive system components, there are also not measurable benefits associated with exposure of workers to exhaust gases containing harmful substances. The negative impact of such substances in exhaust gases like carbon monoxide, nitrogen oxides, and hydrocarbons as well as other substances has been confirmed, so emission of exhaust gases should be maximally reduced. There is an additional benefit, which is difficult to be described using simple quantitative relationships, which reduces the factor responsible for increasing the incidences of certain types of diseases [5]. Research work associated with development of the suggested system will be realized in a mechatronic project, which combines different fields of knowledge. The project will require tests with use of the real available machines as well as with use simulation models.

References

- [1] Technical data from NEWAG Group, www.newag.pl
- [2] Documentation of AscoSpeed 5500 sensor.
- [3] Honegger D., Meier L., Tanskanen P., Pollefey M., *An open source and open hardware embedded metric optical flow CMOS camera for indoor and outdoor applications*, ETH, Zürich 2013.

- [4] Dobrzański P., *Propozycja wykorzystania momentomierza do analizy układu napędowego lokomotywy typu Lds-100K-EMA*, Maszyny Górnictwa 4/2014.
- [5] Szlązak N., Borowski M., *Wentylacyjne aspekty stosowania maszyn z silnikami spalinowymi w kopalniach podziemnych*, Biblioteka Szkoły Eksploracji Podziemnej, Kraków 2002.
- [6] Mężyk A., Dobrzański P., *Modelowanie charakterystyk trakcyjnych napędów na przykładzie pojazdów górnictwa węglowego*. Projekt badawczy N N524 354838, Gliwice 2010–2011 (not published).

PIOTR DOBRZANIECKI, KRZYSZTOF KACZMARCZYK*

TESTS OF DIESEL DRIVES CARRIED OUT AT KOMAG**KIERUNKI BADAŃ NAPĘDÓW SPALINOWYCH
PROWADZONE W ITG KOMAG****A b s t r a c t:**

The directions of KOMAG's investigations into diesel drives used in workings at risk of explosion are described. Two groups of research problems, i.e. the impact of a flameproof inlet-outlet system on the engine's operational parameters as well as identifying the phenomena in the engine regarding the emission of toxic substances with tests on improvement in the quality of exhaust gases, were specified.

Keywords: mining industry, diesel engine, ATEX, quality of exhaust gases

S t r e s z c z e n i e :

W artykule opisano kierunki prowadzonych badań w ITG KOMAG dotyczące napędów spalinowych eksploatowanych w wyrobiskach zagrożonych atmosferą wybuchową. W badaniach tych wyszczególniono dwie grupy problemów badawczych ,tj.: wpływu ognioszczelnego układu dolotowo-wylotowego na parametry pracy silnika oraz identyfikacji zjawisk zachodzących w silniku w aspekcie emisji substancji toksycznych wraz z badaniami pozwalającymi poprawić jakość spalin.

Słowa kluczowe: górnictwo, silnik spalinowy, ATEX, jakość spalin

DOI: 10.4467/2353737XCT.15.173.4378

* Ph.D.Piotr Dobrzaniecki, Ph.D. Krzysztof Kaczmarczyk, Division of Roadway Systems, Institute of Mining Technology KOMAG, Gliwice, Poland.

1. Introduction

In the mining industry, diesel engines are commonly used to drive the machines designed for operation on the surface as well as the locomotives and drivetrains used underground. Using this type of drive safely in underground mine necessitates meeting the requirements associated with the hazard of ignition of flammable dust and/or gases, and with the emission of hazardous substances in the exhaust gases to the workings' atmosphere. The regulations determine composition of air in workings as regards maximum concentration of such substances as carbon dioxide (CO_2), carbon monoxide (CO), nitrogen oxides (NO_x), sulphur dioxide (SO_2) and hydrogen sulphide (H_2S) [9]. The maximum temperature of the surface of objects placed in the atmosphere potentially threatened by coal dust and methane ignition hazard are also determined. Thus, because of the hazards and the permissible concentration of each harmful substance in the atmosphere, operating a diesel drive cannot create the risk of ignition of flammable dust and/or gases present in its operational area, and it cannot worsen air quality. With this in mind, designing a machine with a diesel drive should include systems aimed at ensuring its safe operation. A testing facility enabling complex testing and assessment of impact of diesel engine protecting systems on engine operation has been designed at KOMAG. It is also possible to carry out research work aimed at testing the new systems designed for cooperation with diesel engines, e.g. systems improving the quality of exhaust gases. An overview of the work conducted over the last few years, focusing on the improvement and optimization of diesel drives designed for operation in underground mines, is presented.

2. Tests of diesel drives with reference to the impact of a flameproof inlet-outlet system on engine operation

The hazards resulting from the use of diesel drives in a potentially explosive atmosphere can be reduced by special protections, especially in the diesel engine itself. Protection of engine compartments against contact with atmosphere, in such way that in the case of failure and generation of flame or sparks the ignition of potentially explosive atmosphere is impossible, is the key issue. Moreover, any surface that has contact with external atmosphere cannot reach a temperature above 150°C , i.e. the limit value associated with the possibility of coal dust ignition. A flameproof inlet-outlet system, protecting against propagation of flame or sparks from engine internal compartments to the outside, is one of the components of diesel drives designed for operation in areas threatened by methane and/or coal dust explosions. Its design affects the flow of air and exhaust gases, which can result in the change of engine's operational parameters.

Because of the lack of information about the operation of diesel engines fitted with flame-proof inlet-outlet systems, comprehensive tests aimed at determining its operational parameters were carried out [3, 4]. A general view of the testing facility is presented in Fig 1.

The design of the testing facility and the methodology for testing the engine are described in [2]. The characteristics of an engine cooperating with a simplified inlet-outlet system and with a flameproof inlet-outlet system designed at KOMAG were prepared based on test results. A comparison of the characteristics obtained enabled us to assess the impact of the flameproof inlet-outlet system used on diesel engine performance. Examples of characteristics are presented in Fig. 2 and 3.

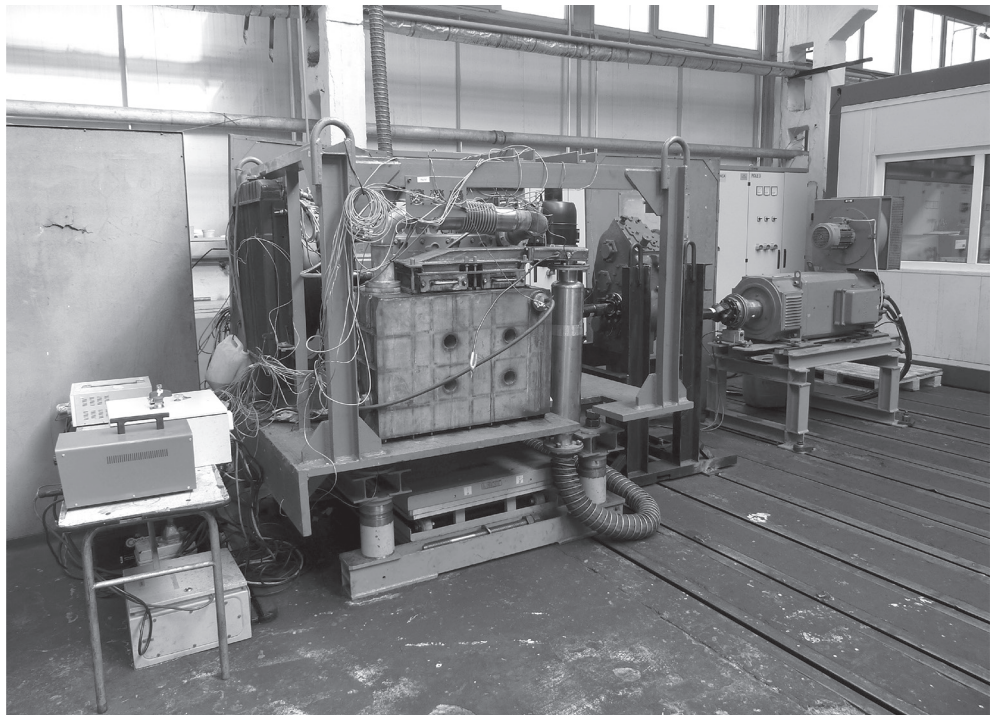


Fig. 1. General view of stand for testing the diesel drives [3]

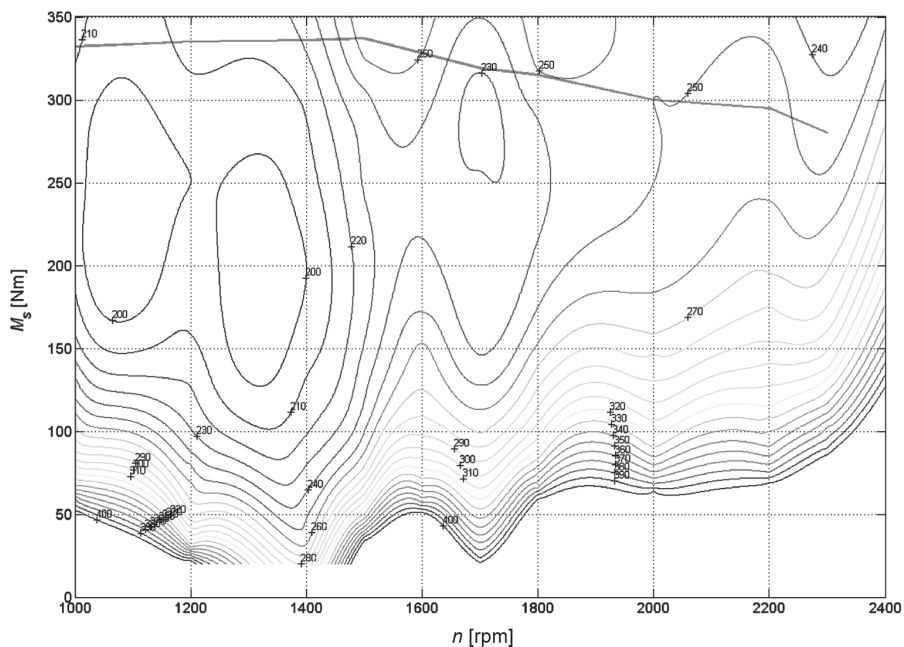


Fig. 2. Versatile characteristics of engine with flameproof inlet-outlet system [2]

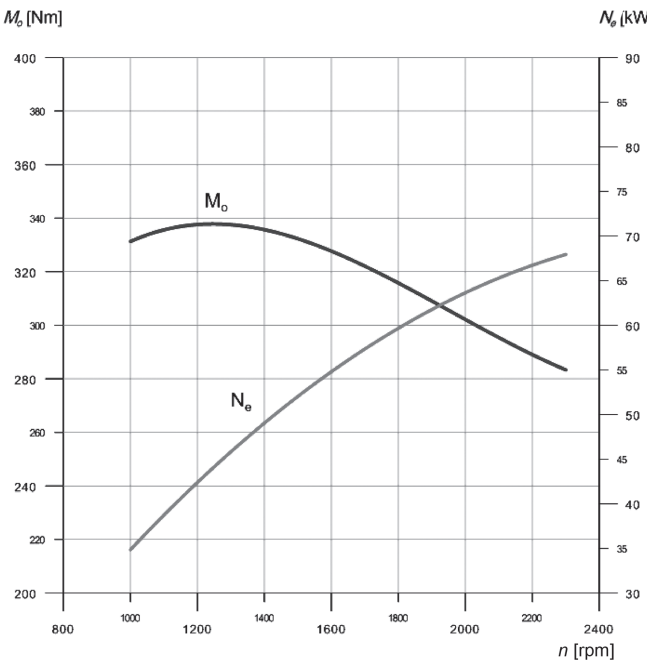


Fig. 3. External characteristics of diesel engine [4]

Unique data as regards operational parameters of diesel engine with a flameproof inlet-outlet system were obtained as a result of stand tests. Further work improving the design of the diesel drive, which is used among others in the Lds-100K-EMA mine underground diesel locomotive, was conducted on their basis. Simulation tests of the inlet-outlet system were carried out and the impact of the system's design on resistance of flow of air and exhaust gases was determined on the basis of test results [2]. The results of stand tests were also used for optimization of design of outlet system. Simulation tests are presented in Fig 4.

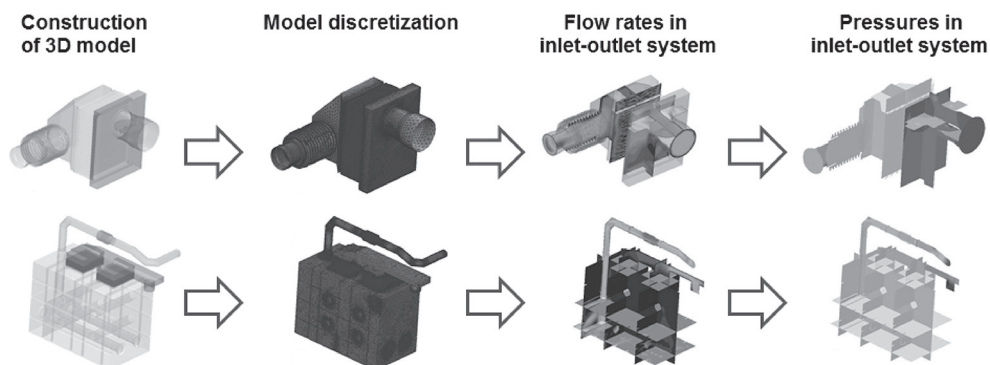


Fig. 4. Simulation tests of inlet-outlet system with use of CFD software programme [3]

An example of a diagram presenting the pressure drop in each component of outlet system is presented in Fig. 5.

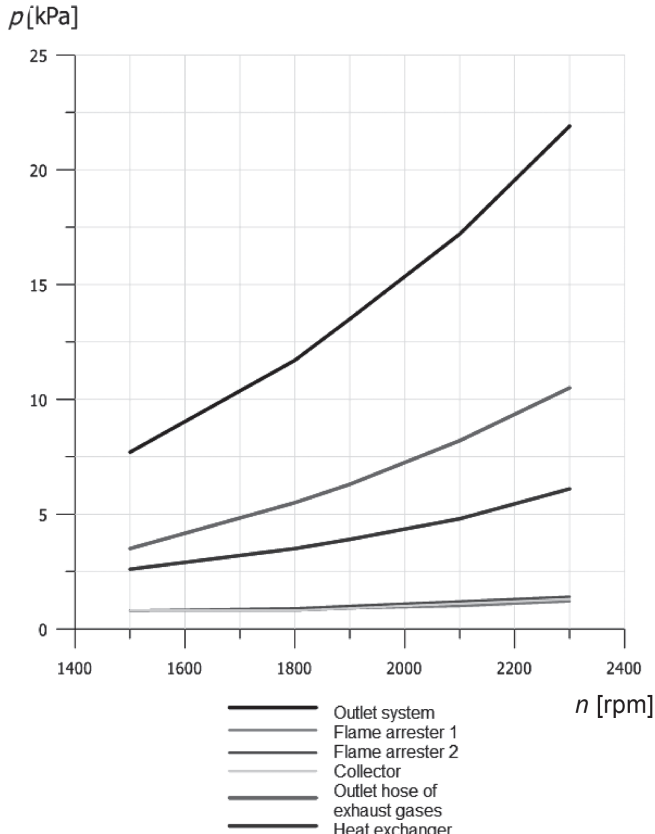
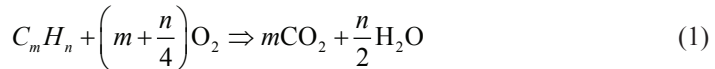


Fig. 5. Flow resistance in each component of the outlet system [3]

Changes in the design of the outlet system, minimizing the flow resistance of exhaust gases, were made as a result of optimization work. Moreover, simulation tests using the results of the stand tests enabled the adaptation of the hydrokinetic gear used in the drive of the Lds-100 locomotive to the diesel engine to be assessed. Further work on stand tests of diesel drive will cover an analysis of the cooperation between diesel engine and hydrokinetic gear, which will enable the model of the driving system to be improved.

3. Tests of diesel drives in the aspect of emission of toxic substances

The processes in an engine's combustion chamber are complex and take place in a very short time. According to theoretical assumptions, H_2O and CO_2 should be the products of hydrocarbon combustion (1).



In fact, the composition of exhaust gases is more complex. According to the composition of exhaust gases presented in Fig. 6, harmful substances represent only 1% of their volume. They include carbon monoxide, hydrocarbons (including the especially harmful polycyclic aromatic hydrocarbons), solid particles and heavy metals, which have a significant impact on the environment, and in the case of machines operating in the workings of underground mines – on the health of mining teams.

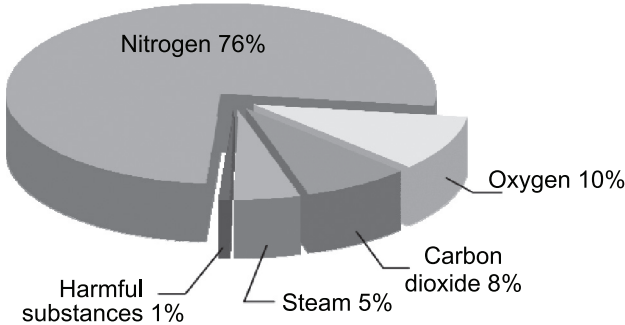


Fig. 6. Sample composition of exhaust gases from self-ignition engines [6]

Tests aiming at identifying the phenomena in the engine in terms of emission of toxic substances have also been carried out within KOMAG's research work on diesel engine designed for operation in underground workings where there is a risk of explosion, to develop methods for reducing the content of toxic substances in exhaust gases.

Within this research work on improving the quality of exhaust gases, the testing facility for diesel drives was extended by a system for processing the exhaust gases (after-treatment system) installed in the outlet system Fig. 7. This was preceded by an analysis of the known methods for converting toxic substances regarding their application in diesel drives operating in a potentially explosive atmosphere. The method of improving the parameters of exhaust gases can be successfully applied in surface machines with no need to change the engine's design.

Testing of the diesel drive which is used in the Lds-100K-EMA underground locomotives and SKZ-81 drivetrain was carried out. The state-of-the-art, turbocharged diesel engine with direct injection was used in this drive. The tests were carried out in eleven stages in the test cycle. Each stage was characterized by operational parameters of engine such as rotary speed and torque. The results of the tests in terms of determining the quality of exhaust gases enabled the conclusion to be drawn that the emission of nitrogen oxides is the most significant hazard (emission of hydrocarbons and carbon monoxide was low). Emission of carbon monoxide was the main problem in the case of diesel drives used in the previous decade, e.g. the SW400 manufactured by Andoria. This problem was less significant in the

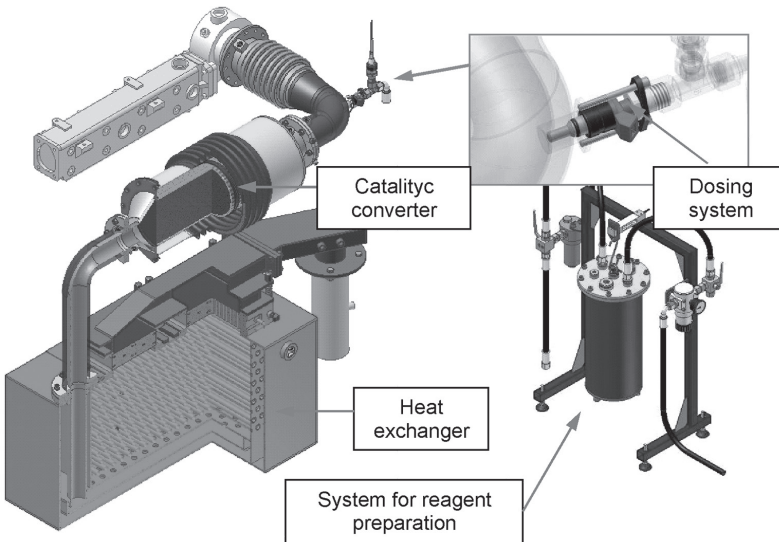


Fig. 7. Systems for processing the exhaust gases in the outlet system [5]

newer D916 engine manufactured by Deutz MWM. These engines were normally aspirated engines with a pre-combustion chamber. The requirements of the ATEX Directive should also be taken into account in the case of drives operating in workings at risk of explosion [8]. The systems for protecting against excessive temperature on the surface can affect the conversion of toxic substances included in exhaust gases. Selective catalytic reduction (SCR) systems were used in the system presented in Fig. 7 [1, 7]. The efficiency of the SCR system was tested at each stage of the test cycle in relation to the operational parameters of the diesel engine and temperature in selected points of the outlet system. The results obtained enabled the impact of temperature protection of external surfaces on the efficiency of the system for conversion of toxic substances to be determined. It was observed that a deposit is prone to settle on the internal surface of the outlet channel, between the reactant injector and the catalytic reactor, which had a negative impact on the level of NO_x conversion. Further work as regards systems for exhaust gases processing will be focused on optimizing the reactant dosing system and design of the outlet channel for exhaust gases in terms of reactions of thermolysis and the hydrolysis of the fed reactant.

4. Summary

The main problem is the absence of any possibility to use the technical solutions applied in the surface machines increasing the economy and ecological effectiveness of such drives in the mine drives, which should meet the requirements of the ATEX Directive. The KOMAG Institute of Mining Technology realizes work on diesel drives designed for operation in workings at risk of explosion. There are the following main directions in the tests carried out at the Division of Roadway Systems:

- tests of diesel drives in terms of the impact of a flameproof inlet-outlet system on the operational parameters of the engine,
- tests of diesel drives in terms of emission of toxic substances.

The tests that have been conducted on the impact of the flameproof inlet-outlet system on the operational parameters of the engine have so far provided information about the flow resistance of air and exhaust gases, and the simulation tests enabled the design of the system to be optimized, minimizing the flow resistance of the medium. The test results enable the fuel consumption to be reduced and the engine efficiency to be increased. The results of the test regarding the ecological aspects of diesel engines operation confirmed the necessity of using the system for conversion of nitrogen oxides in drives that are used underground. The tests carried out using the SCR system gave information about the impact of the mine outlet system on the functionality of the SCR system.

References

- [1] Brzeżański M., Sala R., *Problemy eksploatacji systemów selektywnej redukcji katalitycznej tlenków azotu*, Silniki Spalinowe 3/2013.
- [2] Dobrzański P., Mężyk A., *Kształtowanie cech eksploatacyjnych górniczych pojazdów szynowych*, Monografia nr 39 KOMAG, Gliwice 2012.
- [3] Dobrzański P., *Modelowanie charakterystyk trakcyjnych napędów na przykładzie pojazdów górnictwa węglowego*, grant badawczy promotorowski N524 354835, ITG KOMAG, Gliwice 2011 (not published).
- [4] Dobrzański P., *Doskonalenie napędów spalinowych w aspekcie podnoszenia bezpieczeństwa i niezawodności*, praca statutowa EG\E33-05836, ITG KOMAG, Gliwice 2011 (not published).
- [5] Kaczmarczyk K., *Metoda dostosowania silnika do wymagań górniczych napędów spalinowych*, praca statutowa EG/E44-12421, ITG KOMAG, Gliwice 2013 (not published).
- [6] Kaczmarczyk K., *Ekologiczne aspekty eksploatacji górniczego napędu spalinowego*, Maszyny Górnicze, nr 4, 2013, 56–62.
- [7] Kojtch A., *Zastosowanie selektywnej redukcji NOx amoniakiem (NH3-SCR) do pojazdów napędzanych silnikiem z zapłonem samoczynnym*, MOTROL 6/2004.
- [8] Decree of Ministry of Economy of 22 December 2005 on the main requirements for protective systems and equipment to be use in a potentially explosive atmosphere (Dz.U. of 2005 no 263, pos. 2203).
- [9] Przepisy bezpieczeństwa i higieny pracy oraz prowadzenia ruchu i specjalistycznego zabezpieczenia przeciwpożarowego w podziemnych zakładach górniczych, Katowice 1998.
- [10] Pieczora E., *Doskonalenie napędów spalinowych maszyn i urządzeń górniczych*, report from the statutory project E/BD-7774, ITG KOMAG, Gliwice 1999 (not published).

GUZOWSKI STANISŁAW, MICHNEJ MACIEJ*

FRETTING WEAR IN THE WHEEL-AXLE JOINT OF A WHEEL SET WITH AN AUTOMATIC GAUGE CHANGE SYSTEM

ZUŻYCIE FRETTINGOWE W POŁĄCZENIU KOŁO-OŚ ZESTAWU KOŁOWEGO Z AUTOMATYCZNĄ ZMIANĄ ROZSTAWU KÓŁ

A b s t r a c t

An essential problem in the usage and maintenance of a wheel set with an automatic gauge change system is posed by the wear on the surface of wheel-axle rotary joint. Operational tests have shown that the problem includes fretting wear. This article presents an attempt at explaining this type of wear in a wheel-axle rotary set. The tests were performed on a joint model in which the similarity with the real object in the aspect of dimensions was maintained as well as the character and value of loading. In the description of the fretting wear mechanism in a rotary joint an analogy with wear in a wheel-axle press-fitted joint of a conventional wheel set was shown.

Keywords: railway vehicle, wheelset, railway technology, fretting wear

S t r e s z c z e n i e

W artykule przedstawiono problem eksploatacji i utrzymania zestawu kołowego z samoczynną zmianą rozstawu kół powodowany przez zużycie powierzchni połączenia obrotowego koło-oś. Określono typ zużycia, które występuje w połączeniu obrotowym koło-oś. Badania przeprowadzono na modelu połączenia z zachowaniem podobieństwa wymiarowego do obiektu rzeczywistego. Przedstawiono analogię mechanizmu zużycia frettingowego w połączeniu obrotowym do zużycia frettingowego w połączeniu wciskowym.

Słowa kluczowe: pojazd szynowy, zestaw kołowy, zużycie frettingowe

DOI: 10.4467/2353737XCT.15.174.4379

* Prof. Ph.D. DSc. Stanisław Guzowski, PhD. Maciej Michnej, Faculty of Mechanical Engineering, Institute of Rail Vehicles, Cracow University of Technology.

1. Introduction

The Polish railways, operating in places of two different track gauges, with eight transfer stations on the eastern border, could derive great economic benefits from improving cargo transport between Europe and Asia. The stations at the border of countries that use different track gauges occupy large areas, their track layout is complex, they are equipped with numerous facilities and instruments, and they are staffed by many people. During reloading there is a high risk of ecological contamination of the area. Hazardous cargo transport by rail is impossible because their reloading is prohibited.

What could significantly improve railway transport would be the introduction of rail cars furnished with wheel sets of adjustable gauge of wheels moving from the standard gauge directly to the wide-gauge track and back through a gauge changing facility, built at the contact point of the two tracks. This would eliminate all the difficulties mentioned above.

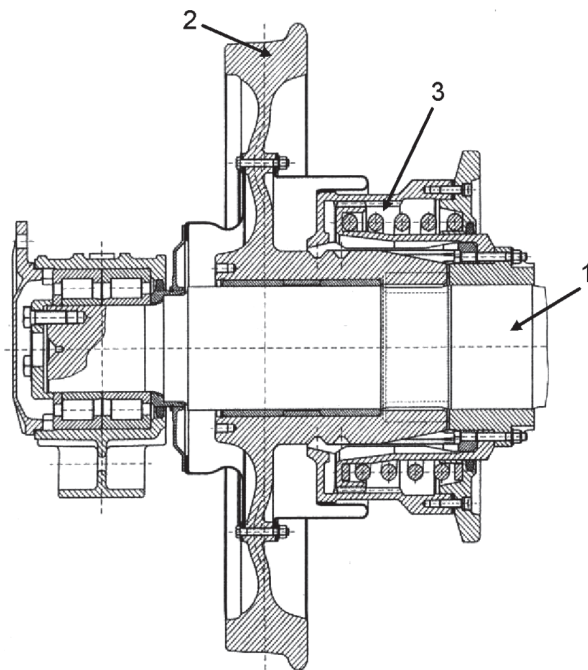


Fig. 1. Cross-section of wheel set with an automatic gauge change system [1]

In an attempt to solve the problem, in the late 1990s an original wheel set was designed and manufactured at the Central Design Bureau of Polish Railways in Poznań. The new wheel set would enable unmanned, automatic transfer from a track of a certain gauge to a track of a different gauge (1435/1520mm), via the gauge changing facility. Part of the cross section of the wheel set discussed has been shown in Fig. 1. Its basic elements include:

- axle (1),
- two wheels moving along the set axle (2),
- locking mechanism (3).

What is the essential element of the design is the wheel-axle joint? Unlike the traditional wheel set, in which the wheels are joined with the axle permanently due to pressing, it is a free assembly joint. This solution makes it possible for the wheels to move along the axle when the wheel gauge is being changed, and to be next locked against the axle during travel.

During the initial operation of the set it was found that serious problems in wheel gauge change occurred even after a short distance covered (1.5 thousand km) [1]. There was a considerable increase in the force necessary for the wheel movement along the axle, which even resulted in damage to the gauge changer. The observation of the wheel seat surface after disassembly of the wheel set showed that there appeared to be fretting wear in the area of contact with the wheel hub. Moreover, considerable grease ageing processes were noticed, which resulted in wheel locking on the axle during the wheel gauge change.

The process of fretting wear in the traditional wheel-axle joint has been described in detail [2], but this only dealt with the press-fitted joint, and the analysis was performed on the basis of results of model studies. In the case of the wheel set with automatic wheel gauge change, however, we are looking at a free assembly joint. This is why the different state of the outer layer of the joined surfaces is observed already at the joining process phase, and this difference may initiate the fretting wear.

This article presents the results of studies on a model of a wheel set with automatic wheel gauge change, simulating real operation conditions and verifying the possibility of the development of fretting wear.

2. Investigation of wear in the wheel-axle with an automatic gauge change system

To explain the mechanism of fretting wear propagation in a wheel-axle joint of a railway axle assembly with an automatic gauge change system, experiments were performed on models simulating the real wheel-axle joint. The dimensions of the specimen (shaft, sleeve) and the material were selected so as to ensure similarity with a prototype pair of the real axle assembly (Fig. 2). The shaft outer diameter and the sleeve inner diameter were selected so as to ensure the running fit in the joint. In the fatigue tests the sleeve was locked against the shaft (as in a real assembly) to prevent its displacement along the perimeter and transverse displacement in respect of the shaft, while maintaining the radial displacement.

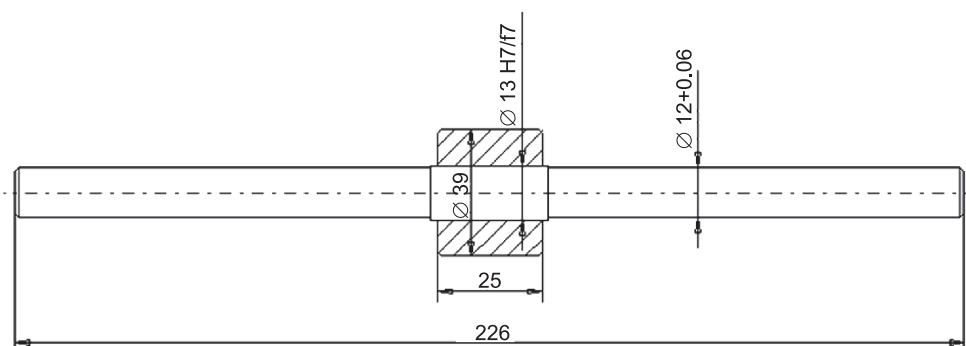


Fig. 2. Dimensions of the sample for modelling tests

The wear tests were performed on a fatigue tester which ensured a load nature in the conditions of rotary bending similar to those in a real wheel set. In the diagram shown in figure 3 the force Q is the base-load of the sample during rotary bending and the force P produces a surface pressure between shaft and sleeve. Forces $P + Q$ simulate the actual static load of the wheelset.

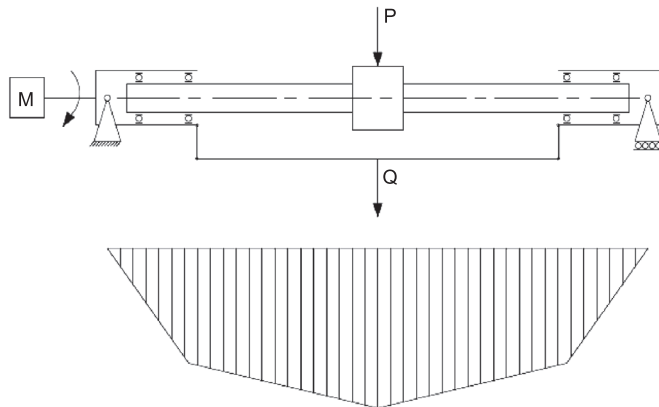


Fig. 3. Specimen loading and bending moment distribution

The tests were performed on a model in which both shaft and sleeve were made from steel (as in the prototype). No lubricants were used in the joint. This variant of specimen preparation was selected in order to obtain the image of the potential wear non-contaminated by other agents. The damage at the coupled elements contact zone will be affected only by the surface pressure from the normal force load P (Fig. 3) and the relative slip between the coupled interface resulting from the deflection of the rotating specimen. These are also the conditions for fretting wear development.

The parameters of specimen testing on the fatigue tester were: rotations $n = 1360$ rpm, specimen loading $Q = 300$ N and $P = 50$ N, number of cycles $N \approx 6 \times 10^6$.

The fatigue tests showed damage on the shafts surface typical of fretting wear. Fig. 4 illustrates a characteristic image of the damage recorded along the length of the joint with the sleeve. Its characteristic feature, common for this type of coupling and loading conditions, is damage distribution, found mainly on the coupling edges.

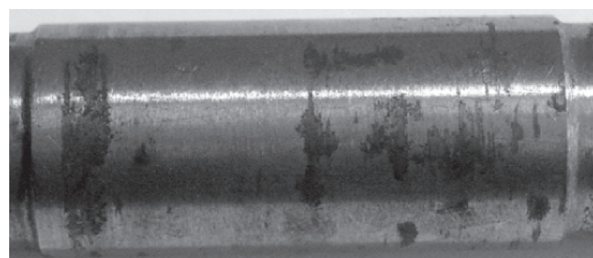


Fig. 4. Shaft surface after fatigue testing – clear marks of fretting wear on shaft edges, with decrease in intensity inwards, magnified ca. 3×

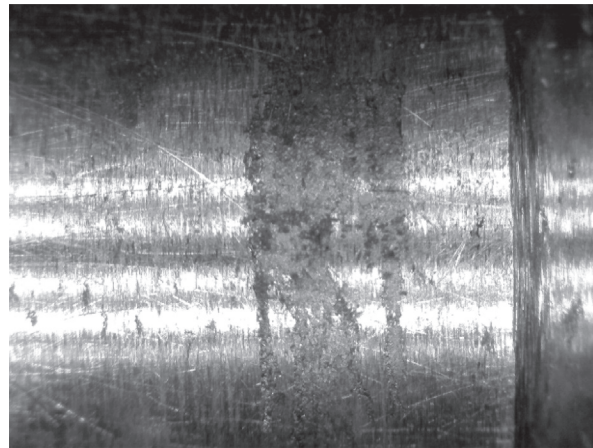


Fig. 5. Macroscopic picture of fretting damage on shaft surface – corrosion marks characteristic of fretting, magn. ca. 15×

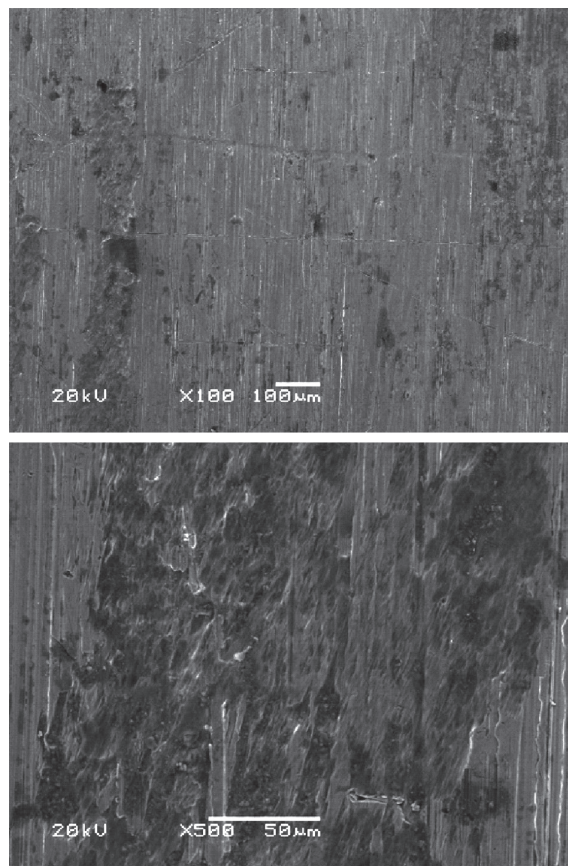


Fig. 6. Scanning picture of fretting damage on shaft seat – pits and material ridges in damage area and its oxidation, magn. 100× and 500×

Fig. 5 shows a macroscopic picture of the surface damage due to fretting wear for selected parts of the shaft seat, Fig. 6 – an image of the damage recorded with a scanning microscope.

For comparison in what follows, the results of tests on a specimen modelling the wheel-axle joint of a conventional axle assembly are discussed. As mentioned before, this is a press-fitted joint. The dimensions of the specimen (shaft, sleeve) and the material were also selected so as ensure the similarity with the real wheel-axle set.

The wear tests were also performed on the MUJ fatigue tester providing specimen variable loading in rotary bending conditions. The parameters of specimen testing were as follows: rotations $n = 1360$ rpm, load of specimen $Q = 400$ N, number of cycles $N \approx 6 \times 10^6$. In the tests the specimen loading with force P was disregarded. For models with press-fitted joint this force is of no consequence for wear development. What is essential is surface pressure resulting from press-fitting the sleeve onto the shaft together with the bending moment which determines the relative slips between the coupled surfaces. Moreover, the tests covered various specimen manufacture manners including different roughnesses of assembly surfaces and different values for the press-fitting. The aim was to test and describe the mechanism of fretting wear development in the wheel-axle joint of a rail vehicle axle set.

The figures below present the characteristic images of wear recorded in tests. Fig. 7 shows a macroscopic picture of the damage on the shaft seat surface for various values of press-fitting, while Fig. 8 gives a scanning picture in the area of the fretting damage.

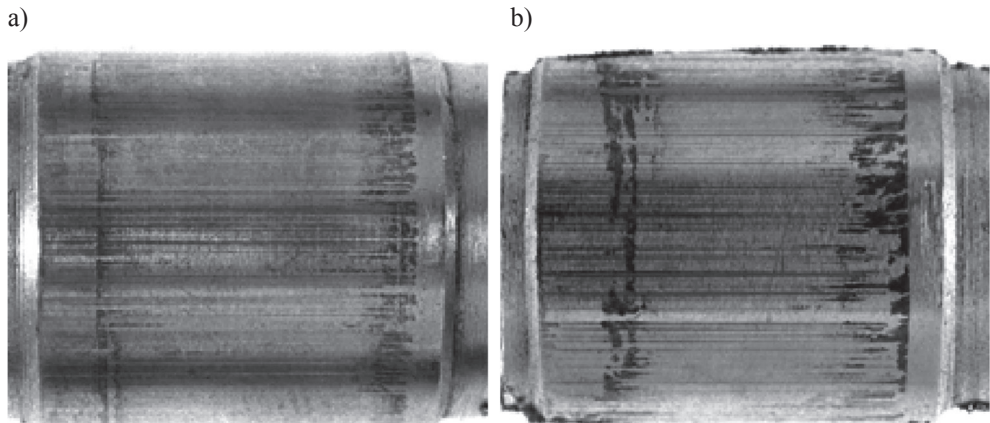


Fig. 7. Photographs of shaft seat after wear tests, press-fitted joint, magn. 4×, press-fitting:
a) – 0,02 mm, b) – 0,04 mm.

The results of tests on a wheel-axle press-fitted joint model show that it is the state of the outer surface of the coupled elements that is the decisive factor in fretting wear development. The state of the surface, in turn, depends on the assembly surface roughness and the value of fitting pressure [2]. The characteristic image of the contact interface for press-fitted joint has been shown in Fig. 8. The effect of the tested factors on the real contact interface is very complex. The decisive aspect is the manner of joint manufacture (press-fitted or thermocompression joint). The other two factors, initial roughness of the surfaces and fitting pressure value are of minor importance, increasing or decreasing the intensity of the changes on the interface.

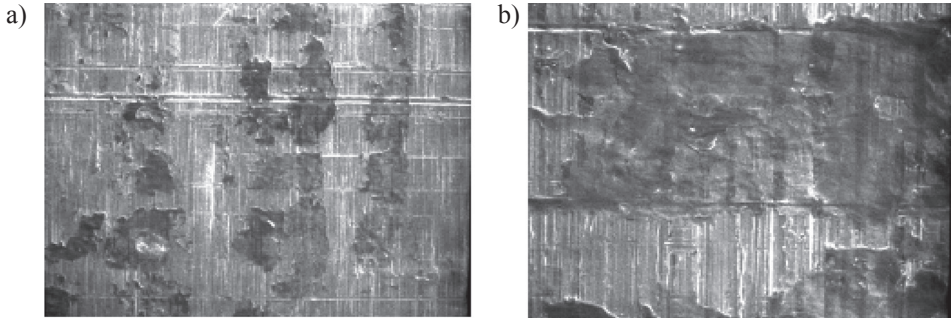


Fig. 8. Scanning picture of fretting wear on shaft seat surface, press-fitted joint,
a) magn. $200\times$ – wear areas scattered on the surface in the form of oxidised ridges,
b) magn. $1000\times$ – material ridges, plastic deformations, pits

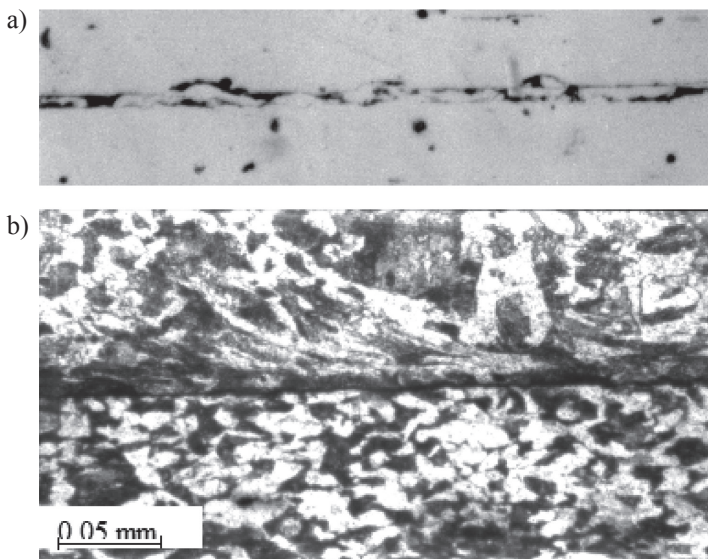


Fig. 9. Shaft-sleeve interface, press-fitted joint, magn. $320\times$, a) non-etched, b) etched

The press-fitting process results in the surface of the contact region along the length of the joint being uneven. The actual contact of primary (first) bodies takes place mainly in the middle part of the joint. Practically, it does not occur on the edge. The other regions of the joint, in turn, are a place where a third body accumulates as a product of surface micro-irregularities truncation during press-fitting. With the increase of roughness of the joined surfaces the length of the contact region containing the third body increases, while the area of the real contact of the primary (first) bodies decreases. An increased fitting pressure value increases the region of the actual contact of the primary bodies.

In fretting wear development in a press-fitted joint the wear is mainly initiated by adhesion, formation and disruption of adhesion tacking. Other types of wear, also at work, such as plastic deformation, oxidation, micro-machining are of minor significance, they

intensify the damage formed earlier due to adhesion tacking disruption. It should be noticed that the majority of researchers [3–8] treat fretting as a phenomenon of very complex wear mechanism, in which adhesive wear, surface fatigue, delamination, oxidation, truncation of irregularities and wear loose by-products overlap or follow each other. The disagreements among particular scientists are derived mainly from the adoption of one of these processes as the initiator of the fretting wear development.

In [2] the fretting wear development mechanism in a wheel-axle assembly was proposed as a process of several stages the most important elements of which are:

- formation of primary (first) bodies actual contact regions during press-fitting,
- generation of relative displacements of very low amplitude at elements surfaces contact due to rotary bending,
- formation of adhesive tacking in regions of actual contact, at joint edges in particular (highest amplitude of relative slips), which next are disrupted to form gaps and ridges on the contact surfaces,
- oxidation of formerly damaged area,
- micro-machining with the oxidised ridge tops of the opposite surface,
- formation of wear by-products as a result of micro-machining – formation of the third body and wear process stabilisation.

3. Conclusions

The comparison of macroscopic and scanning pictures of damage on shafts surfaces in both a press-fitted joint of a conventional wheel set and a rotary one modelling an wheel set with an automatic gauge change system show the similar character of fretting wear development in both joints. The essential conditions for fretting wear development have been met: surface pressures between the coupled surfaces relative slips resulting from specimen deflection in rotary bending conditions. It can then be safely stated, too, that in the wheel-axle joint of an wheel set with an automatic gauge change system the conditions for fretting wear development are satisfied and they will be initiated by the adhesion processes.

Adhesive tacking formation is affected by the following factors:

- physical and chemical properties of the coupled metal surfaces,
- the value of pressure in the contact between the coupled surfaces,
- no oxidised layers on the contact surface,
- the amplitude of the coupled elements oscillations.

The fretting wear development is restricted by, first of all, prevention of adhesion. Oscillations, due to the coupling working conditions, cannot practically be restricted.

One of the ways to eliminate or restrict adhesion, and consequently fretting wear, is to manufacture the elements contact surfaces from materials with a high toughness gradient or to use appropriate lubricants in the joint.

Fig. 10 presents a picture of molybdenum shaft seat surface coupled with a steel sleeve in a rotary joint after fatigue tests using the same parameters as in the rotary joint model. The molybdenum surface hardness was 460 HV that of steel shaft 210 HV. Complete elimination of fretting wear is evident.

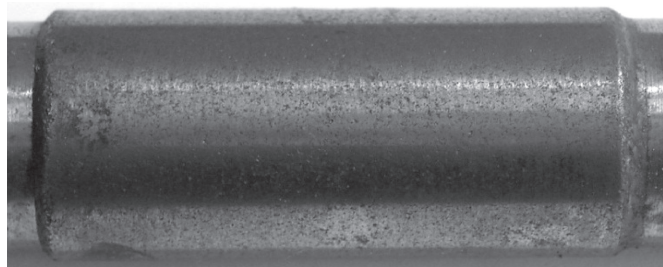


Fig. 10. Surface of molybdenum shaft after fatigue tests – no fretting wear, magn. ca. 3×

A similar effect was obtained when Glacier grease was used in the coupling. The shaft and sleeve were made from steel, similar to the rotary joint model. The image of the shaft surface after fatigue tests is shown in Fig. 11.



Fig. 11. Surface of steel shaft lubricated with Glacier grease after fatigue tests – no fretting wear, magn. ca. 3×

The examples of shaft surfaces after fatigue testing in manufacture variants other than the prototype model to restrict adhesion confirm the very favourable effect leading to fretting wear elimination. In this way the thesis is also confirmed that the fretting wear process is initiated by adhesion.

References

- [1] Suwalski R.M., *The Automatic Wheel Gauge-Changing System of Rail Vehicles*, AGH University of Science and Technology Press, Dissertations and Monographs 154, 2006.
- [2] Guzowski S., *Analysis of Fretting Wear in Clamped Joints on Example of Rail Vehicle Wheel set Axles*, Cracow University of Technology Press, Monographs 284, 2003.
- [3] Neyman A., *Fretting in Machine Elements*, Gdansk University of Technology Press, 2003.
- [4] Waterhouse R.B., *Fretting fatigue*, Applied Science Publishers Ltd., London 1981.
- [5] Volchok A., Halperin G., Etsion I., *The effect of surface regular microtopography on fretting fatigue life*, Wear, 253, 2002, 509–515.

- [6] Yoshiharu Mutoh, Jin-Quan Xu, *Fracture mechanics approach to fretting fatigue and problems to be solved*, Tribology International, 36, 2003, 99–107.
- [7] Waterhouse R.B., *Fretting Wear*, ASM Handbook, vol. 18, Friction, Lubrication and Wear technology, Clevelaud, OH, ASM International, 1992, 233–256.
- [8] Zhou Z.R., Nakazawa K., Zhu M.H., Maruyama N.Ph., Kapsaand L., Vincent, *Progress in fretting maps*, Tribology International, 39 (10), 2006, 1068–1073.

MICHAŁ KLUZIEWICZ*

MODELLING MANOEUVRES THAT MAY INDUCE SIDE SKID IN A FRONT-WHEEL DRIVE CAR

MODELOWANIE MANEWRÓW WYWOLUJĄCYCH STAN ZARZUCENIA W SAMOCHODZIE PRZEDNIONAPĘDOWYM

Abstract

The simulation and experimental verification of oversteer inducing manoeuvres are presented. A transient state of oversteering in a front-wheel drive car is initiated only by using steering wheel, throttle and brake inputs. The car's motion is simulated with a single-track dynamic model with a parameterized input that sufficiently reproduces the behaviour of a front-wheel drive Peugeot 106 XSI (group N). The conclusions may be useful in better understanding complex driving techniques and vehicle dynamics that are not commonly described in basic elaborations.

Keywords: *vehicle dynamics, car driving techniques, road traffic safety, oversteering, side skid*

Streszczenie

Przedstawiono wyniki badań symulacyjnych oraz drogowych dla manewrów wywołujących przejściowy stan nadsterowności przednionapędowego pojazdu o podsterownej charakterystyce w ruchu ustalonym. Do analizy symulacyjnej wykorzystano rowerowy model o nielinijowych charakterystykach samochodu Peugeot 106 XSI (N-grupowy) zweryfikowany podczas prób drogowych. Inicjacja stanu nadsterowności następowała wskutek zadanego wymuszenia kierownicą oraz pedałami przyspieszniaka i hamulca. Wyniki pracy mogą być przydatne w zrozumieniu bardziej złożonej dynamiki samochodu i techniki jego prowadzenia, które nie są opisywane w klasycznych opracowaniach.

Słowa kluczowe: *dynamika samochodu, techniki prowadzenia, bezpieczeństwo ruchu drogowego, nadsterowność, zarzucenie*

DOI: [10.4467/2353737XCT.15.175.4380](https://doi.org/10.4467/2353737XCT.15.175.4380)

* MSc. Michał Kluziewicz, Faculty of Mechanical Engineering, Cracow University of Technology.

1. Introduction and aims

The vast majority of technically fit passenger cars, apart from their construction and drive type, are characterized by understeer steady-state cornering behaviour. Nonetheless almost every understeer car can be forced by the driver to induce a temporary state of oversteering of a various durations. These are the most essential factors for initiating oversteering:

- tyre load change by accelerating/decelerating,
- additional tyre horizontal loads required to change the angular momentum of chassis yaw rotation,
- limitation of tyre friction (tyreforce ellipse) [8].

As a parts of the author's previous investigations the following goals were completed:

- creation of a plain dynamic model of a front-wheel drive car with suitably parametrized inputs that sufficiently simulates states of oversteering [5],
- definition of the manoeuvres that possibly induce oversteering in a nominally understeering front-wheel drive car [4],
- sensitivity analysis of different driving techniques affecting the possibility of oversteering occurrence in manoeuvres considered [5],
- verification of the car model formula and steering methods via comparison to data collected during execution of road tests [5],
- comparison of race and rally cornering techniques efficiency in a front-wheel drive car [6].

The main goal of this paper was to compare the data obtained during road tests to the modelled oversteer manoeuvres. In addition to previous articles, all simulations were followed by equivalent test drives. The second objective was to present the overlapping timelines for both simulations and trials. The following manoeuvres that could possibly induce oversteering in typical road traffic conditions were taken into consideration:

- a) "Scandinavian flick" – slight steering input towards the opposite direction of the corner, then steering into the turn, while sharply lifting off the throttle [11],
- b) "Left-foot braking" – braking while the throttle is opened.

In this example a nominally understeering front-wheel drive compact car was considered. Manoeuvres were executed with open-loop steering – no driver model was used. The results may be useful for a better understanding of complex car dynamics and driving techniques that are not widely described in basic elaborations. Some examples of aggressive manoeuvre simulations with different drive types and other surfaces can be found in quoted articles [1, 3, 11].

2. Formulation of the rally car model

The car's motion on a flat, plain and non-deformable surface was simulated with a single-track dynamic model [11]. The model consists of three rigid bodies: car chassis and 2 wheels (reduced front and rear axles). Both wheels rotate while the front one swivels. Driving and braking torques are applied to the wheels.

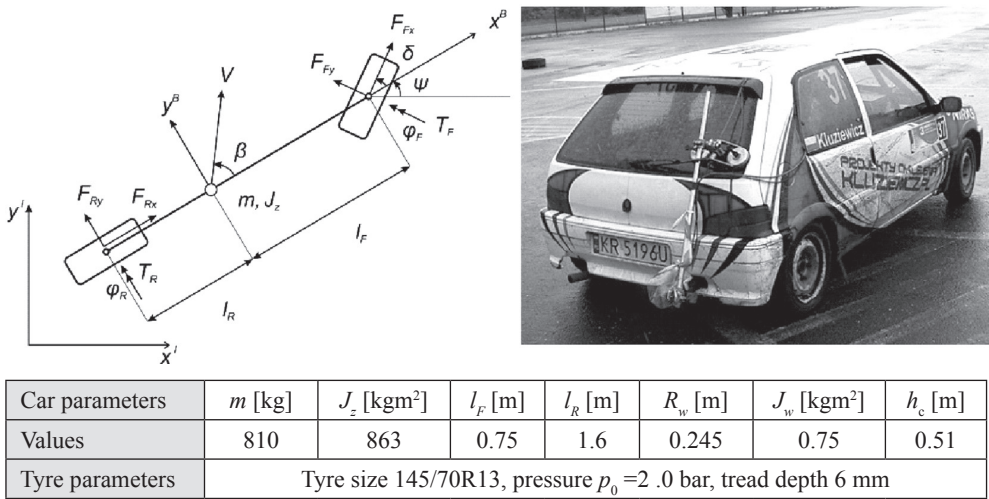


Fig. 1. Bicycle car model scheme and test vehicle photograph

A physical model with five degrees of freedom, represented by x , y , ψ , φ_F and φ_R coordinates, was formulated according to the following assumptions:

- the suspension travel effects, steering trapeze, differential, stabilizing moment and drivetrain dynamics were neglected;
- the tyres slip characteristics of both axles were reduced to one wheel (one trail);
- the vertical load variations were calculated by a static relation formula;
- the tyre relaxation length was taken into account.

The following values were assumed as parametrized inputs: steering wheel rotation angle, throttle pedal travel and brake pedal travel (dimensionless, range 0 to 1), handbrake acutation, gear change, clutch engagement.

The vehicle movement in accordance with this model [11] is described in a x^i, y^i cartesian coordinate system with following equilibrium of forces and moments equations.

$$m\ddot{x} = F_{Fx} \cos(\psi + \delta) - F_{Fy} \sin(\psi + \delta) + F_{Rx} \cos \psi - F_{Ry} \sin \psi \quad (1)$$

$$m\ddot{y} = F_{Fx} \sin(\psi + \delta) + F_{Fy} \cos(\psi + \delta) + F_{Rx} \sin \psi + F_{Ry} \cos \psi \quad (2)$$

$$I_z \ddot{\psi} = (F_{Fy} \cos \delta + F_{Fx} \sin \delta) l_F - F_{Ry} l_R \quad (3)$$

$$I_i \dot{\omega}_i = T_i - F_{ix} r, \quad i = F, R \quad (4)$$

The semi-empirical “Magic formula” model was used to imitate the tyre to road interaction in definite motion conditions [9]. This formula allows the calculation of tangent forces values as a function of complex longitudinal slip, lateral slip and tyre vertical load force [1].

Rolling resistance force, air resistance force and functional combustion engine model are included. The quasi-static relation between torque, crankshaft rotational speed and throttle angle is provided by means of an approximating function.

Car model parameters were estimated based on data collected during the execution of stationary and road tests, the author's experience, and similar literature elaborations [4, 5]. The propriety of using a single track model in the states of motion described was experimentally confirmed in essay [5].

3. Simulations and road testing results

Software simulations were performed in order to validate the capability to induce oversteering with various steering inputs. Afterwards simulation results were compared to data collected during the execution of corresponding road tests [1]. The following road experiments were performed in order to verify the single-track vehicle model and validate the capability to induce oversteering in front-wheel drive car.

Road tests were conducted under the following conditions:

- constant car balance, one setup;
- plain, flat tarmac surface;
- light rain providing continuous dampness of surface;
- air temperature around 15°C, no strong wind;
- air pressure in cold tyres 2.0 bar.

3.1. “Pendulum turn” experimental results

The first manoeuvre is defined as a slight steering input in the opposite direction of the turn, then steering into the turn, while sharply lifting off the throttle. Comparison of experimental (dotted line) and simulation (solid line) traces are presented in Fig. 4. The initial vehicle speed was 64 km/h with the throttle opened 34%.

At time $t = 0.9$ s the throttle pedal was lifted off and simultaneously a sinusoidal input to the steering wheel (approx. 200° to the right) was started. Subsequently step input (approximately 220° to the left) was initiated. The shapes of the road tests and simulation functions are very similar. The tiny differences are in slip angle values. In the simulation timeline the slip angle is delayed (phase shifted) by approximately 0.5 s. Maximum slip angle acquired during the simulation runtime is greater than 40° and still growing.

Due to the simulated vehicle trajectory (Fig. 2) and road test observations, also for the vehicle yaw rate and slip angle values it is noticeable that the car was firmly sideskidding.

3.2. “Left-foot” braking experimental results

The second manoeuvre is defined as a simultaneous pressing of accelerator and brake pedal while executing a turn. Comparison of the experimental (dotted line) and simulation (solid line) time courses are presented in Fig. 3. The initial speed of the vehicle was approximately 63 km/h with the throttle opened 35%.

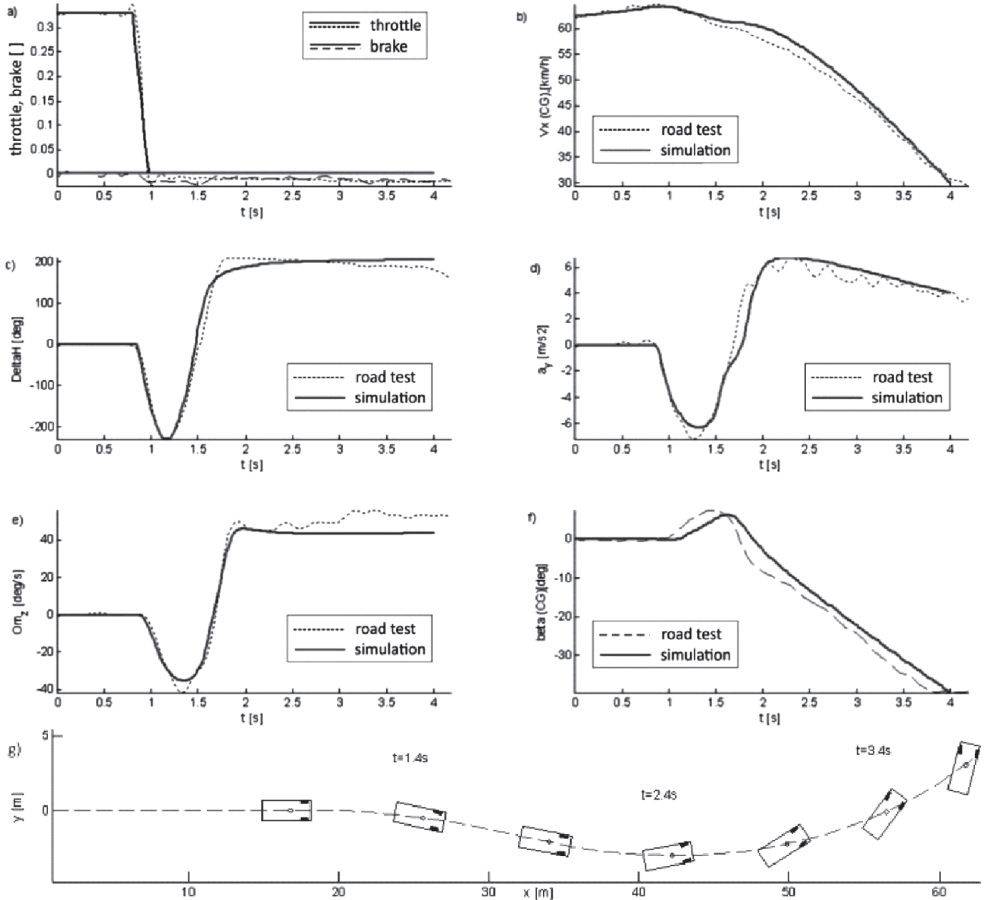


Fig. 2. Experimental and simulation results of “Scandinavian Flick” manoeuvre: a) throttle and brake commands; b) vehicle longitudinal velocity; c) steering wheel control (steering command) d) lateral acceleration; e) vehicle yaw rate; f) slip angle of vehicle’s centre of inertia; g) vehicle trajectory

At time of $t = 1.5$ s the throttle pedal was lifted off and a step input to steering wheel (approximately 210° to the left) was started. Subsequently at time $t = 2.8\text{--}4.5$ s both accelerator and brake pedal were pressed and held. In the simulation timeline throttle liftoff was omitted as an irrelevant factor towards the car’s behaviour. In order to correct the shorter acceleration time, initial speed in the simulation was increased.

The shapes of the signals from road tests and simulations are very similar. The tiny differences are in the vehicle’s yaw rate. Due to the simulated vehicle trajectory (Fig. 3), road test observations, also from the vehicle yaw rate and slip angle values it is noticeable that the car was sideskidding intensely.

The maximum slip angle achieved during the simulation runtime is greater than 90° and car is moving backwards to a full stop in further simulations.

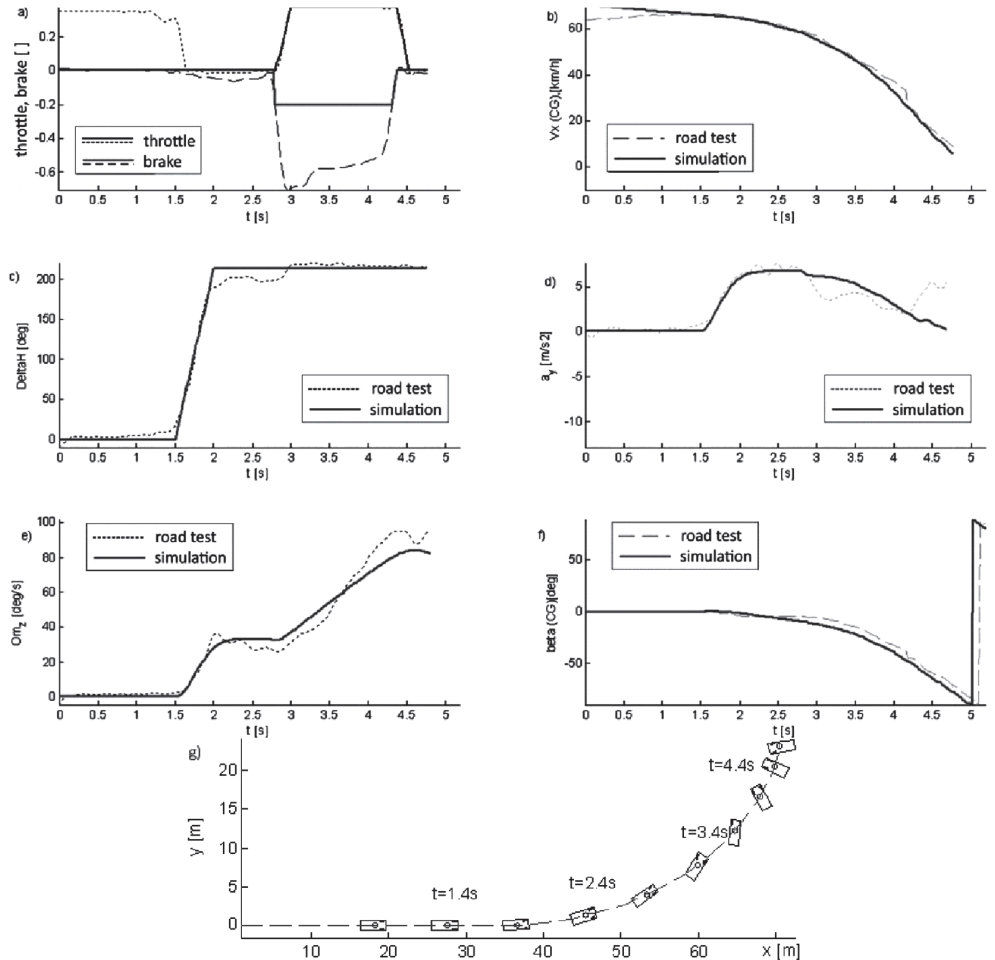


Fig. 3. Experimental and simulation results of “left-foot braking” manoeuvre: a) throttle and brake commands; b) vehicle longitudinal velocity; c) steering wheel control (steering command) d) lateral acceleration; e) vehicle yaw rate; f) slip angle of vehicle’s centre of inertia; g) vehicle trajectory

4. Conclusion

Two methods of inducing oversteering in a nominally understeer front-wheel drive car were presented. The results of simulations were verified qualitatively and quantitatively based on road tests and the author’s experience. No driver reaction (feedback) was assumed.

According to road experiments results of more than 90% of model accuracy were obtained (for constant car setup) in all runs. Both manoeuvres induced significant side-skid (slip angles over 40° during runtime). In real life driver reactions may both strengthen or weaken the oversteering tendency.

References

- [1] Abdulrahim M., *On the Dynamics of Automobile Drifting*, SAE 1019, 2006.
- [2] Bogdanow O. A., Cyganow E. S., *Sportowa Jazda Samochodem*, WKiŁ, Warszawa 1989.
- [3] Hindiyeh Y., Gerdes Ch., *Driftkeeping: path tracking at the friction limits using high sideslip cornering*, International Association of Vehicle System Dynamics, Manchester 2011.
- [4] Kluziewicz M., Maniowski M., *Stany nadsterowności podsterownego samochodu z przednim napędem*. Zeszyty Naukowe Instytutu Pojazdów Politechniki Warszawskiej, z.1(77), 2010, 169–177.
- [5] Kluziewicz M., *Przejściowe stany nadsterowności podsterownego samochodu z przednim napędem*, praca dyplomowa-magisterska, Wydział Mechaniczny, Politechnika Krakowska, 2010.
- [6] Kluziewicz M., Maniowski M., *Porównanie wyścigowej i rajdowej techniki pokonania luku samochodem przednionapędowym*, Czasopismo Techniczne, 5-M/2012, 51–62.
- [7] Maniowski M., Materiały z koła naukowego „Inżynier Ścigant”, Kraków 2011.
- [8] Mitschke M., *Dynamik der Kraftfahrzeuge, Band B*, Springer-Verlag, 1984.
- [9] Pacejka H.B., *Tyre and Vehicle Dynamics*, Butterworth-Heinemann, SAE, 2002/2006.
- [10] Velenis E., Tsotras P., *Minimum Time vs Maximum Exit Velocity Path Optimization During Cornering*, 2005 IEEE International Symposium on Industrial Electronics, Dubrovnic, Croatia, June 2005
- [11] Velenis E., Tsotras P., Lu J., *Modeling Aggressive Maneuvers on Loose Surfaces: The Cases of Trail-Braking and Pendulum-Turn*. Proceedings of the 2007 European Control Conference, Kos, Greece, July 2–5, 2007.

JÓZEF KŁAPUT*

**INFLUENCE OF AGING TEMPERATURE ON
MECHANICAL PROPERTIES OF THE PRECIPITATION
HARDENED MARTENSITIC MARVAC 300 STEEL****WPŁYW TEMPERATURY STARZENIA NA WŁAŚCIWOŚCI
STALI MARLENZYTYCZNEJ GATUNKU MARVAC 300
UTWARDZANEJ WYDZIELENIOWO****A b s t r a c t**

This paper presents the results of a comprehensive study of precipitation hardened martensitic steel after quenching and aging at a number of selected temperatures. The results of metallographic and dilatometric studies are presented along with the effect of aging temperature on hardness, strength and resistance to cracking. A significant effect of aging temperature on the properties of the material was found.

Keywords: maraging steel, tensile strength, toughness, aging, dilatometric curve

S t r e s z c z e n i e

W artykule przedstawiono wyniki badań stali martlenzytycznej utwardzanej wydzielniowo po hartowaniu i starzeniu przy kilku wybranych temperaturach. Zaprezentowano wyniki badań metalograficznych, dylatometrycznych oraz wpływu temperatur starzenia na twardość, wytrzymałość i odporność na pękanie. Badania wykazały istotny wpływ temperatur starzenia na właściwości badanego materiału.

Słowa kluczowe: stal maraging, wytrzymałość na rozciąganie, udarność, starzenie, krzywa dylatometryczna

DOI: 10.4467/2353737XCT.15.176.4381

* PhD. Józef Kłaput, Institute of Material Engineering, Faculty of Mechanical Engineering, Cracow University of Technology.

1. Introduction

In modern equipment, of increasing importance are steels with a strength between 1000 MPa and 2000 MPa. In ferrous alloys, the mechanical properties of such values are obtained by bainitic microstructure [1, 2], but more often by martensitic. Martensite steels can be divided into two groups.

The first group includes those steels hardened mainly with carbon and through the application of heat treatment and plastic working. Increasing carbon content in steel improves the strength of the material, but also decreases its plastic properties and promotes the appearance of brittle fracture – a phenomenon particularly dangerous in structural steels.

The second group is composed of low-carbon maraging steels, which offer a satisfactory combination of mechanical and plastic properties. These are the steels in which the primary strengthening mechanism during heat treatment is the precipitation of intermetallic phases in a matrix of nearly carbonless martensite. Reducing carbon content prevents the formation of carbides and promotes the formation of intermetallic phases. The intermetallic phases precipitate along the dislocations formed during martensitic transformation, i.e. along the laths of martensite. The alloying elements in these steels are nickel and cobalt, introduced in amounts that allow this steel to remain in the class of martensitic grades. These elements additionally promote high ductility. The main hardening elements are molybdenum and titanium, and indirectly cobalt, since cobalt reduces the solubility of molybdenum in α iron, which is beneficial to increasing the amount of dispersion precipitates [3, 4].

Nickel content in an amount of about 18% increases the hardenability and after the austenitising process these steels are through-hardened, even when cooled in air. The hardness of the nickel, low-carbon martensitic structure is low, which makes this structure suitable for plastic working. An increase in the steel strength parameters is achieved during aging. Yet, it should be remembered that an aging process that is too long or carried out at a temperature higher than that recommended will reduce the mechanical properties – an phenomenon known as alloy overageing [6].

2. Test material

The test material was Marvac 300 steel plate with a thickness of 6.5 mm. The chemical composition is given in Table 1.

Table 1
Chemical composition of the tested steel, weight [%]

Ni	Co	Mo	C	Mn	Si	Ti	Al	P	S
18,67	9,40	4.58	0.014	0.14	0.03	0.75	0.12	<0.01	<0.01

Based on the analysis of the content of alloying elements it has been concluded that the material corresponds to the N18K9M5T steel grade produced in Poland in the late twentieth

century [5]. Steels of similar chemical composition produced by foreign manufacturers are known under various trade names such as Nimarc300, 18Ni300 grade or X2NiCoMo18-9-5 [10, 11].

3. Microstructure of the tested steel

This steel is characterised by high metallurgical quality as indicated by its chemical composition as well as microscopic examinations. The surfaces of specimens in unetched condition show no sign of distorted non-metallic inclusions. Only in a few of many fields of vision is the presence of single precipitates of the characteristic titanium carbonitrides noted. Figure 1 shows the steel microstructure etched and subjected to four different variants of heat-treatment:

The microstructure after quenching corresponds to a low-carbon lath martensite. EDS studies have shown that, despite some structural differences, the material has the same chemical composition. The structure after quenching from 830°C and aging at 480°C has

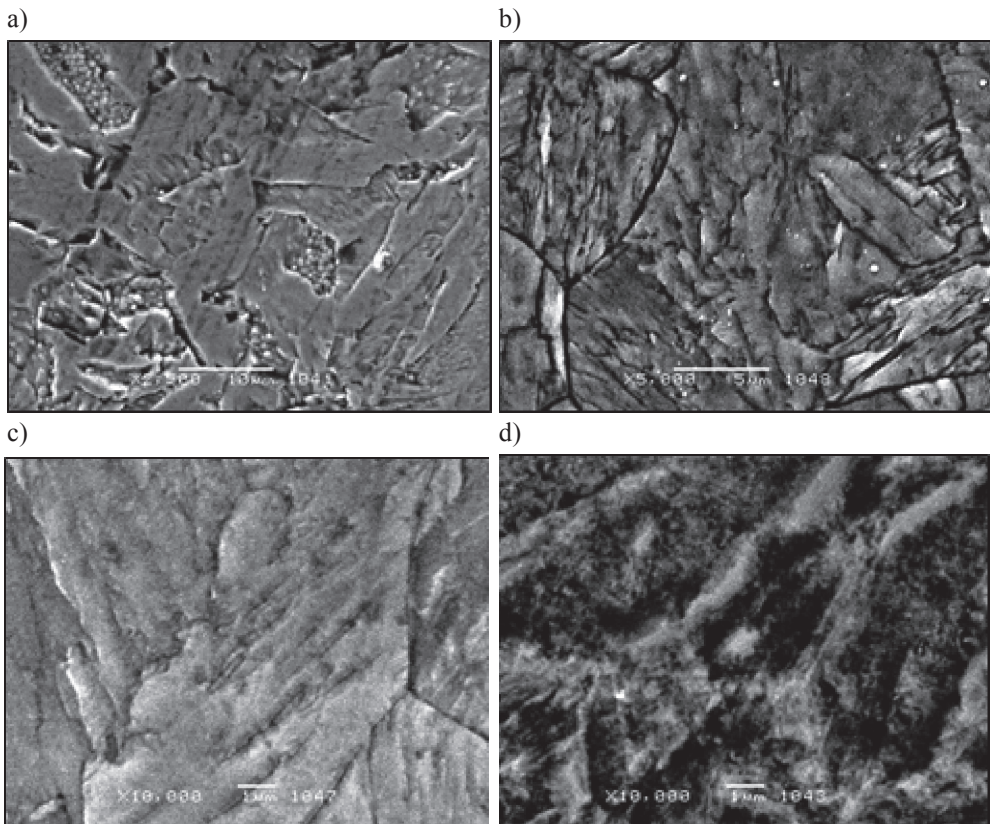


Fig. 1. Steel microstructures: a) quenched from 830°C, b) quenched from 830°C/ and aged at 400°C, c) quenched from 830°C and aged at 480°C, d) quenched from 830°C and aged at 550°C

a more uniform character. One can see the grain boundaries and elements of microstructure that exist inside the grains. The lath character of the martensite is well presented.

Quenching from 830°C with aging at 550°C changes the microstructure of the steel. High magnifications reveal microregions after the presence of very fine precipitates.

4. Dilatometric studies

Samples with a diameter of 4 mm and a length of 35 mm were heated to a temperature of 900°C at a rate of 4°C/min and then cooled at the same speed.

The results of the dilatometric measurements are presented in Fig. 2. Additionally, charts were drawn up to show the dimensional changes and the rate at which those changes occur in time (Fig. 3 – the solid line shows the rate of dimensional changes [%/min] and the dotted line shows the level of dimensional changes occurring in a sample [%]).

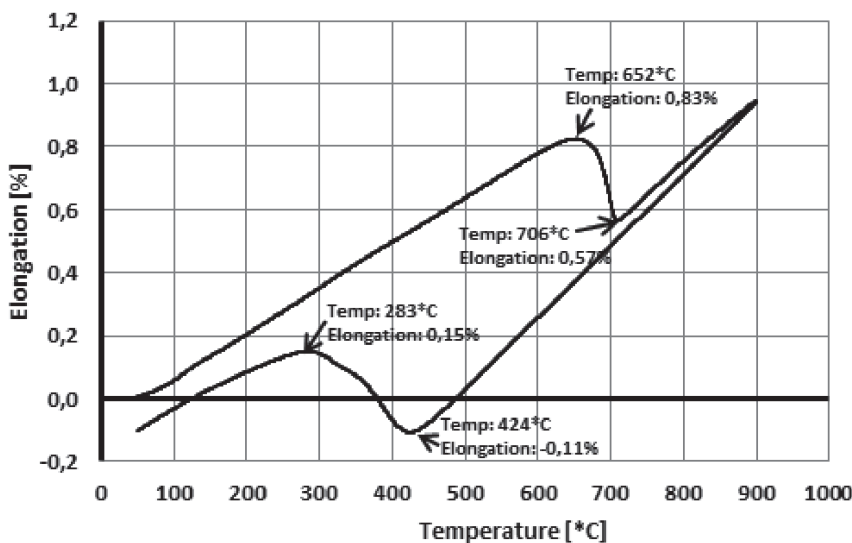


Fig. 2. Dilatogram of sample – the heating and cooling rate was 4°C/minute

In the dilatogram at 652°C one can see the beginning of austenite transformation. The end of the $\alpha \rightarrow \gamma$ transformation takes place at 706°C. During further heating up to 900°C, no other phase transformations were recorded by the dilatometer. Throughout cooling at a rate of 4°C/minute, the austenite is stable up to a temperature of 424°C.

At this temperature, the undercooled austenite is transformed into a diffusion-free structure of higher specific volume, as evidenced by a clear increase in the sample length. The martensitic transformation ends at the M_f temperature somewhere about 283°C.

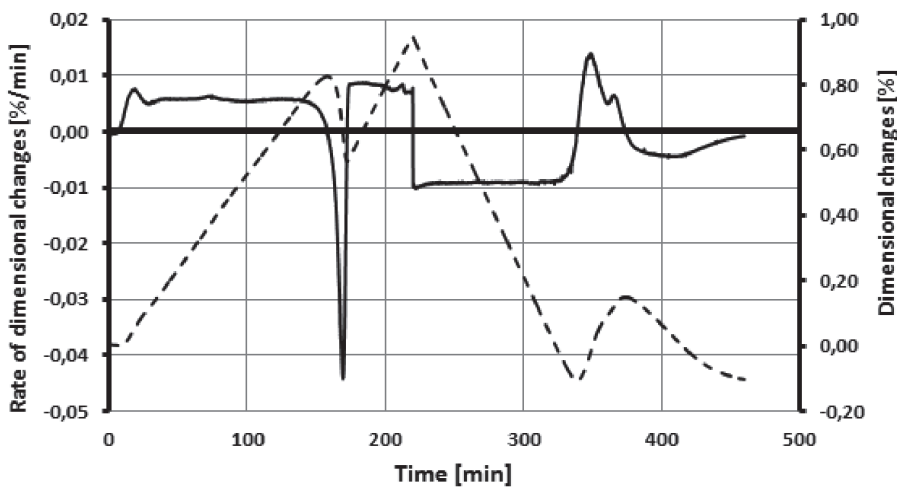


Fig. 3. Dimensional changes and the rate of these changes occurring in a dilatometric sample

5. Testing of mechanical properties

The Marvac 300 steel exhibits different properties, depending on the heat treatment applied, and aging temperature in particular [9]. The following shows how six variants of the heat treatment (quenching, and quenching and aging at five different temperatures) affect the hardness, strength and toughness of the steel tested.

The hardness of the samples after quenching was at a level of about 30 HRC. The effect of aging at five different temperatures (300°C , 400°C , 480°C , 550°C and 600°C) on the average steel hardness values is illustrated in Fig. 4. In each case, the aging time was 4 hours.

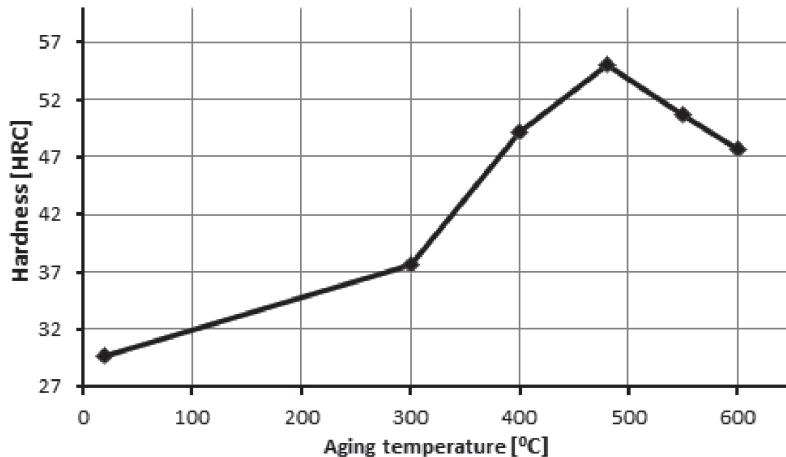


Fig. 4. Aging temperature vs hardness of Marvac 300 steel

The lowest hardness was obtained in the as-quenched state. Aging in the temperature range between 300°C and 480°C made the crystallographic lattice rearrange the atoms of the elements forming intermetallic phases, thus leading to a hardening of the material and hardness increase up to a maximum value of 55HRC at an aging temperature of 480°C. Aging at higher temperatures, i.e. at 550°C and 600°C, reduced hardness by breaking the coherence of the lattice of the precipitating intermetallic phases, at the same time inducing austenite recovery [7, 10].

Aging also affects the strength parameters obtained (Fig. 5). The steel after quenching is characterised by the lowest values of the yield strength $R_{0,2} = 915$ MPa and tensile strength $R_m = 1055$ MPa, combined with high percentage elongation of up to 10%.

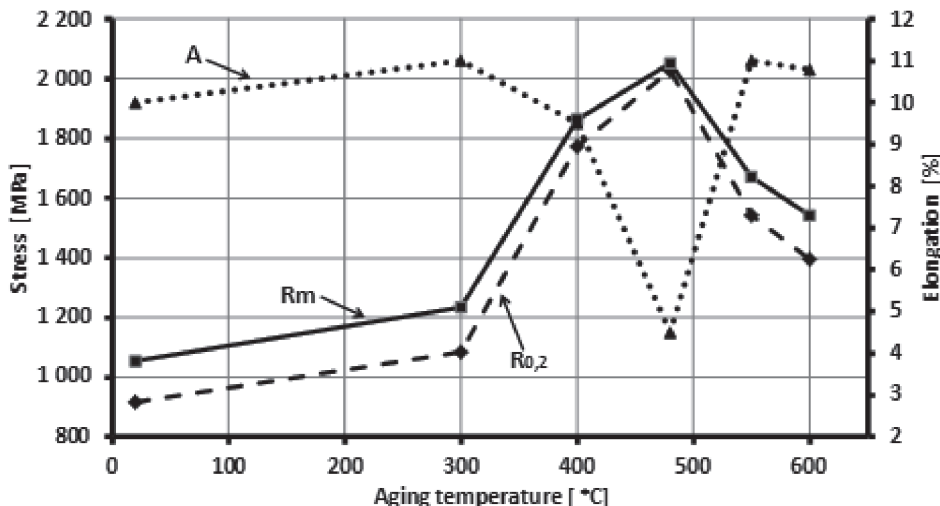


Fig. 5. Yield strength and tensile strength vs aging temperature

The strength starts increasing with the increasing temperature of aging. Its maximum yield strength $R_{0,2} = 2029$ MPa and tensile strength $R_m = 2051$ MPa the material reaches at a temperature of 480°C with small percentage elongation of 4.5%.

Aging at higher temperatures of 550°C and 600°C reduces the strength and increases the percentage elongation. At temperatures so high, the aforementioned effect of austenite recovery also takes place, which means that the microstructure now contains, besides the aged martensite, also small but numerous areas of austenite. Austenite on cooling transforms into a low-carbon plastic martensite which results in a loss of strength.

Also deserving of some attention is the change of another parameter referred to in the literature as the “ductility margin”, i.e. the yield strength to tensile strength ratio $R_{0,2}/R_m$, which indicates the material’s susceptibility to plastic deformation [8]. Figure 6 shows the lowest value for this ratio after quenching and its maximum after aging at a temperature of 480°C. This confirms earlier observations that Marvac 300 steel has the best plastic properties in as-quenched condition and the lowest susceptibility to plastic deformation after aging at 480°C.

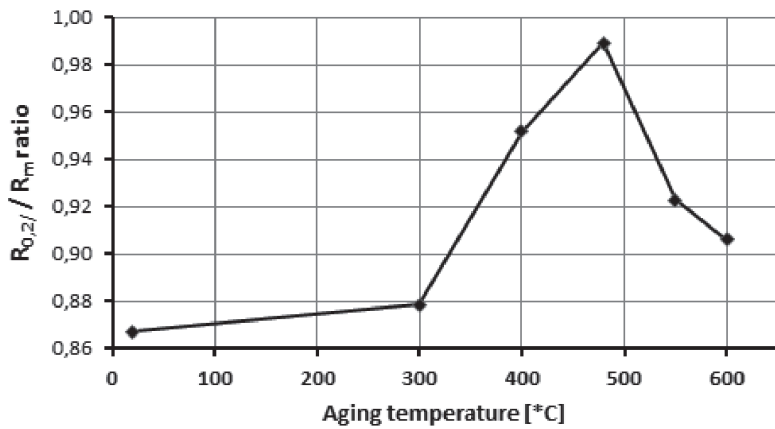


Fig. 6. $R_{0,2}/R_m$ ratio vs aging temperature

Due to the insufficient thickness of the plate, which prevented the execution of standard impact samples, tests were carried out on samples with dimensions $5 \times 10 \times 55$ mm, "V" notched to a depth of 2 mm. The samples were broken at ambient temperature.

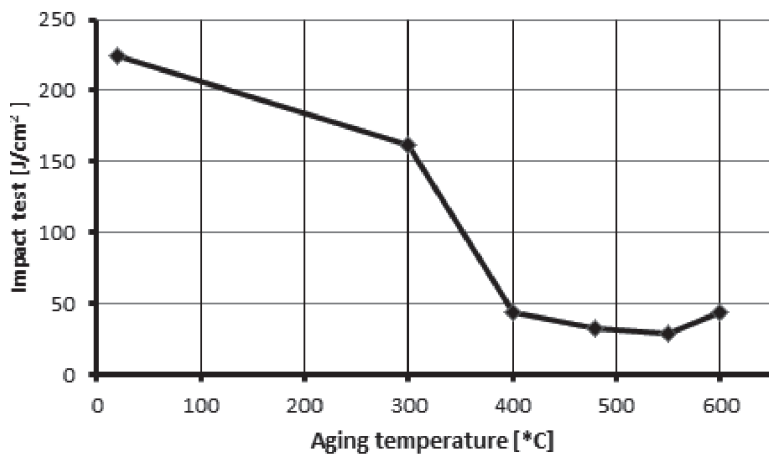


Fig. 7. Toughness vs aging temperature for Marvac300 steel

The plotted graph (Fig. 7) confirms the obvious relationship between the impact test – toughness and temperature of aging. The highest toughness is exhibited by the material in as-quenched condition and the value $224\text{ J}/\text{cm}^2$ is calculated per 1 cm^2 of the broken surface. Increasing the aging temperature results in a significant decrease toughness. For the temperature of 400°C and higher it is below $50\text{ J}/\text{cm}^2$.

6. Discussion of results and conclusions

Microscopic observations and the results of dilatometric studies confirm that even at a very low cooling rate, the steel undergoes a diffusion-free transformation which increases the specific volume of the material. Nickel maraging steel is characterised by small dimensional changes during heat treatment. When heated, these changes are at the beginning of the $\alpha \rightarrow \gamma$ transformation amount to 0.83%. During cooling, at the start of the $\alpha \rightarrow \gamma$ transformation, they amount to approximately -0.11%.

The highest strength values are obtained after quenching and aging at 480°C. Aging at 400°C for 4 hours gives lower values of R_m , but at the same time it provides a better combination of strength, ductility, and toughness. A distinct reduction in strength and hardness occurs at higher aging temperatures. This phenomenon is due to a coagulation of the precipitated intermetallic phases and breaking of their coherence, all this combined with austenite recovery. Properly controlled austenite recovery may be a beneficial phenomenon. The forming austenite, which at the time of cooling is transformed into plastic martensite, when properly distributed in the microstructure, can improve the ductility of the material.

The largest dynamic loads are transferred by the maraging steel after quenching. In this state, it has also high ductility and good cold workability. Low-carbon nickel martensite, free from precipitates, can offer toughness exceeding 220 J/cm².

According to the Hollomon-Jaffe parameter, lower annealing temperatures and longer times produce similar effects as annealing at higher temperatures and shorter times. Hence it seems advisable to consider aging at lower temperatures and extended times of heating.

The determination of critical temperatures for A_1 and A_3 and the stability range of the undercooled austenite is useful in designing a thermo-plastic treatment process for the tested steel.

References

- [1] Bhadeshia H.K.D.H., *The first bulk nanostructured metal*, Science and Technology of Advanced Materials, nr 14, 2013.
- [2] Pytel S.M., Garcia C.I., DeArdo A.J., *Fracture toughness of ultra-low carbon bainitic steels for heavy plate applications*, Proceedings of International Conference on Processing Microstructure and properties of Microalloyed steels, Pittsburgh 1991.
- [3] Marcisz J., Burian W., Adamczyk M., *Właściwości mechaniczne stali maraging MS300 po starzeniu krótkotrwałym*, Prace Instytutu Metalurgii Żelaza nr 2, Gliwice 2013.
- [4] Burian W., Marcisz J., *Kinetyka procesów wydzieleniowych w stalach maraging podczas krótkotrwałego starzenia*, Prace Instytutu Metalurgii Żelaza nr 2, Gliwice 2013.
- [5] Stale stopowe o wysokiej wytrzymałości do pracy w zakresie temperatur od -90 do 500°C, broszura informacyjna o programie produkcyjnym Huta Baildon – Hutniczy Zakład Wytwórczo-Doświadczalny „Mikrohuta”, KAW Katowice 1986.
- [6] Mahmoudi A., Zamanzad Ghavidel M.R., Hossein Nedjad S., Heidarzadeh A., *Aging behavior and mechanical properties of maraging steels in the presence of submicro-crystalline Laves phase particles*, Materials Characterization, ISSN 10445803 nr 10 Elsevier Science 2011.

- [7] Kladaric I., Krumes D., Marković R., *The Influence of multiple-solution annealing on kinetics of structural transformation of maraging steels*, Materials and Manufacturing Processes, issue 8, 2006.
- [8] Kawagoishi N., Nagano T., Moriyama M., Kondo E., *Improvement of fatigue strength of maraging steel by shot peening*, Materials and Manufacturing Processes issue 12, 2009.
- [9] Kladaric I., Kozak D., Krumes D., *The Effect of Aging Parameters on Properties of Maraging Steel*, Materials and Manufacturing Processes, issue 7–8, May 2009.
- [10] Mateja P., *Badania przemian fazowych w stalach maraging metodami rentgenowskimi*, U.Ś., Katowice 1990.
- [11] Ciszewski B., Przetakiewicz W., *Nowoczesne materiały w technice*, Bellona, Warszawa 1993.

KATARZYNA MACIEJASZ*, RAFAŁ BOGUCKI**

THE EFFECT OF DEFORMATION ROUTE IN EQUAL CHANNEL ANGULAR PRESSING ON MECHANICAL PROPERTIES OF ALUMINUM ALLOY 1050

WPŁYW DROGI ODKSZTAŁCENIA PLASTYCZNEGO W PROCESIE ECAP (EQUAL CHANNEL ANGULAR PRESSING) NA WŁAŚCIWOŚCI MECHANICZNE STOPU ALUMINIUM Z SERII 1050

A b s t r a c t

Annealed samples of commercial purity aluminium (1050) were processed by Equal Channel Angular Pressing (ECAP) at room temperature for up to eight passes. ECAP was conducted by using three processing routes (schemes). Tensile tests and micro hardness were conducted to evaluate variation of mechanical properties after each pass. Analysis of fractography was carried out due to investigate a fracture of the samples. The results showed that all the schemes had similar micro hardness values – around 50 HV. The tensile test results showed that the highest yield strength was achieved in the second scheme after eight passes – 186 MPa – while elongation maintained at the level of 17.4%. The value of yield strength achieved increased more than six times in proportion to annealed condition.

Keywords: aluminium, severe plastic deformation, equal channel angular pressing, mechanical properties

S t r e s z c z e n i e

Wyżarzone próbki, wykonane ze stopu aluminium AA1050, poddano procesowi przeciskania przez kanał kątowy (Equal Channel Angular Pressing – ECAP) w temperaturze pokojowej. Próbki przeciskano w ośmiu cyklach według trzech dróg odkształcania. W celu oceny zmian właściwości mechanicznych przeprowadzono statyczną próbę rozciągania oraz pomiar mikrotwardości. Wykonano również analizę fraktograficzną w celu obserwacji przelomów próbek. Otrzymane wyniki mikrotwardości we wszystkich schematach wykazywały zbliżone wartości – na poziomie 50 HV. Statyczna próba rozciągania wykazała, że najwyższa granica plastyczności $R_{p0,2}$ została osiągnięta dla próbki przeciskanej według II drogi odkształcania po ósmym cyklu i wyniosła 186 MPa przy wydłużeniu równym 17,4%. Uzyskana wartość granicy plastyczności wykazuje ponad sześciokrotny wzrost w stosunku do stanu wyżarzonego.

Słowa kluczowe: aluminium, techniki intensywnych odkształceni plastycznych, przeciskanie przez kanał kątowy, właściwości mechaniczne

DOI: 10.4467/2353737XCT.15.177.4382

* MSc. Katarzyna Maciejasz, (graduate) Cracow University of Technology.

** PhD. Rafał Bogucki, Institute of Material Engineering, Faculty of Mechanical Engineering, Cracow University of Technology.

1. Introduction

The dynamic development of industry leads to an increased demand for new types of materials, which are characterized by high strength properties while maintaining relatively good plastic properties. According to the dependence of Hall-Petch, the refinement of microstructure is the only known mechanism to achieve high strength and good ductility [1, 2]. Traditional techniques refinement of microstructures such as thermomechanical processes allow a grain size of about $2, 3 \mu\text{m}$ to be obtained. However, intensive plastic deformation techniques (Severe Plastic Deformation – SPD) are methods for obtaining submicron or nano-size [3, 4]. In these methods plastic deformation is used in order to create a cell dislocation substructure [5, 6]. A major advantage in SPD is that the material cross section is unchanged during pressing. There are wide severe plastic deformation techniques. The most popular include: Equal Channel Angular Pressing (ECAP), High Press Torsion (HPT), Accumulative Roll Bonding (ARB), and Cyclic Extrusion Compression (CEC) [7–12]. ECAP is processing. ECAP is a technique whereby an intense plastic strain is imposed by pressing a sample in a special die. The die consists of two channels with a square or circular cross-section and bend radius usually of 90° .

The aim of this study is to analyse the influence of road plastic deformation in the ECAP process on the mechanical properties of aluminium alloy of series AA1050.

2. Experimental procedure

Commercial purity aluminium (AA 1050) was used in this study. The chemical composition of the alloy was performed on a Bruker Q4TASMAN spectrometer and the result is shown in table 2.1. The content of the elements correspond to the chemical composition of the AA 1050 alloy according to PN – EN 573-3:1998.

Table 1

**Comparison of the chemical composition of the aluminum alloy AA1050
Series PN – EN 573-3:1998 and test material.**

	Chemical composition [wt.%]							
	Al	Fe	Si	Cu	Mn	Mg	Zn	Ti
AA 1050	99.54	0.304	0.066	0.004	<0.002	0.008	0.005	0.008
AA 1050 PN –EN 573-3:1998	≥ 99.50	≤ 0.40	≤ 0.25	≤ 0.05	≤ 0.05	≤ 0.05	≤ 0.07	≤ 0.05

Material for the study was provided in the form of a cold drawn bar with a cross section $40 \times 10 \text{ mm}$, from which were cut longitudinal samples of $55 \times 10 \times 10 \text{ mm}$ dimensions.

Prior to the process of pressing the sample was annealed at 500°C for 8 h and then cooled in a furnace. The annealed samples were lubricated using a graphite based lubricant and pressed in a square channel ECAP die with dimensions $10 \times 10 \text{ mm}$. The applied die was

characterized by internal angle $\phi = 90^\circ$ and the angle of the external $\psi = 20^\circ$. A view of the die with marked angles is shown in Fig. 1b. The ECAP process was performed using hydraulic testing machine, EU 20.

The samples were pressed by three schemes:

- Scheme I – The samples were pressed without rotation – the sample was pushed next sample,
- Scheme II – The samples were rotated after each cycle of alternating forward – backward. The bending process always occurred on the same surface – the sample was pushed next sample,
- Scheme III – The samples were pressed as in Scheme I, after each passed die was revs up and the sample was pulled out.

The samples were processed to 1 up to 8 passes. The micro-hardness was determined under load of 5N in an Innovatest 400 Series 423a Vickers micro-hardness meter. The tensile test was performed at room temperature on an MTS Criterion Model 43 hydraulic testing machine.

Tensile samples with gauge dimensions of $14 \times 3 \times 5$ mm were machined from the ECAP samples and their tensile axes were paralleled to the pressing direction. The fracture surface of the tensile testing samples were conducted using a scanning electron microscope (SEM) Joel JSM5510LV.

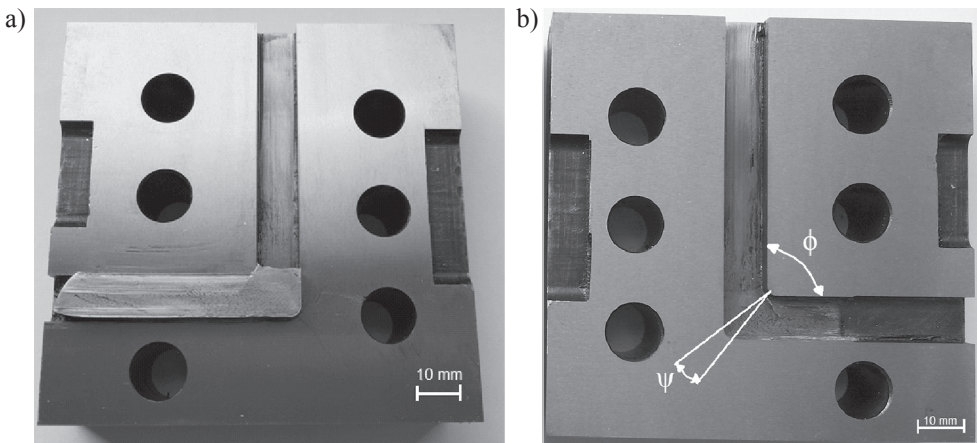


Fig. 1. A picture of ECAP die used in this study: a) die with sample, b) characteristic angles

3. Results

The micro hardness was measured on the cross section on the samples deformed by routes I and II. Measuring points were located at distances of 1 mm. On the samples deformed by route III the measurement was made on lateral surface at points which were located at distances of 3 mm.

The annealed material had a micro hardness level of about 22.5 HV, yield stress – 30 MPa and elongation – 39.8%. Fig. 2 presents a summary of the micro hardness values obtained for each pass in each routes.

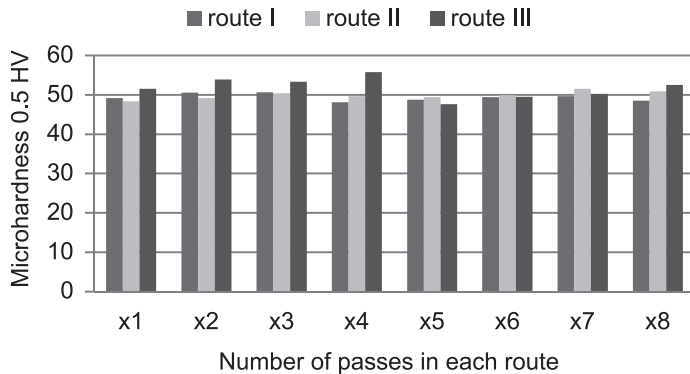


Fig. 2. Summary of micro hardness values obtained for each pass in each route

The highest increase of micro hardness was achieved in route I. The measurements were made on the lateral surface because of the limited amount of research material. This method of measurement led to an overvaluation of the micro hardness due to strong deformation of the sample surface due to the friction of the surface of the die. Comparing the samples whose micro hardness was measured on the cross section it was observed that the highest value was achieved in the sample deformed by route II after the seventh pass – about 52 HV. This value was more than double than value of the annealed sample.

Tensile tests enabled the evaluation of variation of the yield stress and the elongation. Fig. 3 and Fig 4 show respectively the summary of the yield stress values and elongation values achieved for each pass in each route.

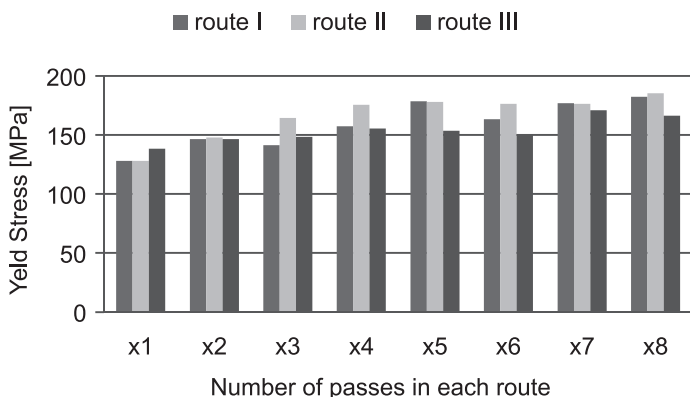


Fig. 3. Summary of achieved values of yield stress for each pass in each route

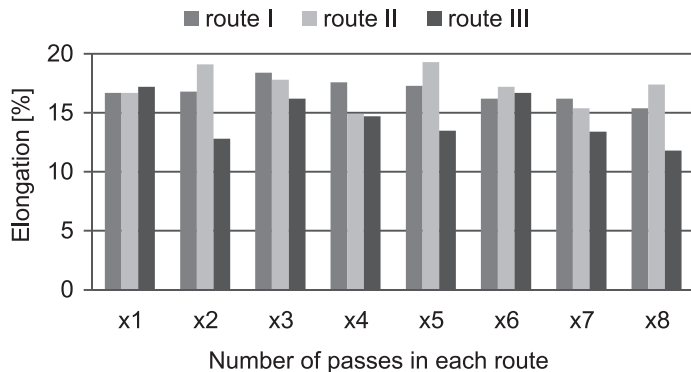


Fig. 4. Summary of values of elongation achieved for each pass in each route

The highest value of yield stress was 185 MPa. This was achieved after the eighth pass of route II. This value is six times higher than the value of the annealed sample. The lowest values of yield stress were achieved for samples deformed by route III. The greatest elongation was achieved by the sample deformed by route II after the fifth pass and this was almost 20%. The lowest recorded values for this parameter were reached by the samples deformed by route III.

Fractography showed that the fractures in all the deformed samples were ductile. There were no significant differences in the topography of fractures of particular samples. Fig. 5a and Fig. 5b show example images of fractures of samples deformed by route II after the second and eighth passes.

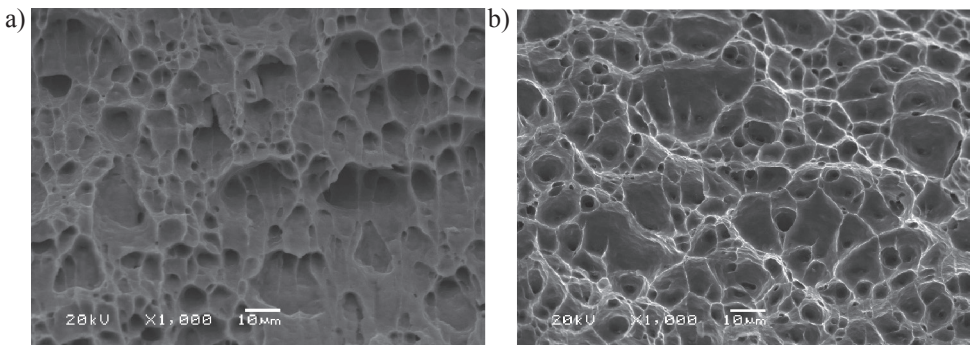


Fig. 5. Fractures of samples deformed by route II: a) after second pass, b) after eighth pass

4. Discussion

The aim of this paper was to analyse the effect of the deformation route in Equal Channel Angular Pressing (ECAP) on the mechanical properties of aluminium alloy AA 1050. An annealed material had low mechanical properties (yield stress – 30 MPa) and high formability

(elongation 39.8%). After the first pass of ECAP a significant increase in yield stress and micro hardness and a decrease of plasticity were observed. There was more than a four times increase in yield stress which was 128 MPa for routes I and II and 139 MPa for route III. The formability was limited, which can be observed in the decrease of the elongation which was 19.1% for routes I and II and 17.2% for route III. Such a significant increase in yield stress and decrease in plasticity is a consequence of strong plastic deformation of the material and an increase in dislocation density. The effect of this is to strengthen the material. Subsequent passes of ECAP led to further improvement in the mechanical properties with plasticity at a similar level. This is probably caused by significant grain refinement, which can be achieved by structure fragmentation and an increase in subgrain misorientation angle [13]. The aim of SPD methods is to achieve microstructure with the largest share of high angle grain boundaries. Decrease in grain size leads to an increased volume fraction of grain boundaries. This leads to an increase in the number of barriers to the movement of dislocations. At the same time this does not limit the capability of the dislocation glide. It allows for an increase in the mechanical properties while plasticity maintains a relatively high level.

The best combination of mechanical properties was achieved in route II. The highest yield stress was reached in pass eight and amounted to 186 MPa with elongation at a level of 17.4%. The highest plasticity was also recorded in route II. This was 19.3% after fifth pass with yield stress at a level of 178 MPa. The lowest combination of mechanical properties was achieved in route III. The reason for this is probably the lower value of cumulative strain in samples which were taken apart from the die compared to the samples which were pressed through the die. The conduct of deformation in routes I and II led to stronger deformation of a sample, which is connected with higher cumulative plastic strain and higher increase in dislocation density. Higher dislocation density leads to the appearance of cellular a substructure which, due to the coalescence of subgrains, leads to an increase in misorientation angle and significant grain refinement. Numerous scientific studies confirm that an increase in deformation degree leads to an increase in subgrain misorientation angle. As a consequence significant grain refinement and the appearance of high angle grain boundaries can be observed [5, 11, 12].

Variations in micro hardness correlate with the mechanical properties obtained. The highest increase in micro hardness was recorded after the first pass. There were no significant changes in subsequent passes. The highest micro hardness was obtained for route III after the fourth pass and this amounted to 55.8 HV. The difference in the values between routes I and II is probably due to the method of measurement. The micro hardness was measured on the cross section on the samples deformed by routes I and II and on the lateral surface on the sample deformed by route III. Micro hardness analysis showed high homogeneity of microstructure on the cross section for routes I and II, which is evidenced by the relatively small spread of values.

Fractographic observations confirm high formability. For all the fractures analysed the mechanism of transcrystalline ductile fracture was observed. The results confirm the analysis of the effect of the ECAP process on the mechanical properties of aluminium alloy 1050 conducted. The specific method of conducting plastic deformation allows both high strength and ductility to be obtained. Comparing these properties with those of aluminium alloy 1050 deformed by conventional methods an increase in both strength and ductility was observed. After classic cold working the value of yield stress does not exceed 145 MPa with elongation at a level of 7%. After ECAP the obtained value of yield stress was at level of 186 MPa with elongation of 17.4%. The results obtained in this study correlate well with similar

work. Changing the route of the plastic deformation has a positive effect on the mechanical properties [5, 14].

5. Conclusions

1. Mechanical properties increased with successive cycles for each scheme, while the ductility remained at a similar level.
2. The value of the yield strength $R_{p0.2}$ increased six-fold compared to the annealed for scheme I and II at an elongation of respectively 15.4% and 17.4%, after eight passes.
3. The best combination of mechanical properties were obtained for the samples deformed according to scheme II, while the worst for scheme III.
4. Changing of deformation route by rotating the sample by scheme II had a positive effect on the mechanical properties after the ECAP process.

References

- [1] E. O. Hall, Proc. Phys. Soc. London, 643 (1951), 747-753.
- [2] N. J. Petch, J. Iron Steel. London, 173 (1953), 25.
- [3] R. Z. Valiev, N. A Krasilnikov, N. K. Tsenev, Mater. Sci. Eng. A137, 1991, 35.
- [4] B. Verlinden, *Severe plastic deformation of metals*, 2nd International Conference on Deformation Processing and Structure of Materials Belgrade, Serbia and Montenegro, 26–28 May 2005.
- [5] El-Danaf E. A., Soliman M.S., Almajid A. A., El-Rayes M.M., *Enhancement of mechanical properties and grain size refinement of commercial purity aluminum 1050 processed by ECAP*, Materials Science and Engineering A, 458, 2006.
- [6] M. Furukawa, Y. Iwahashi, Z. Horita, M. Nemoto, T. G. Langdon, *The shearing characteristics associated with equal-channel angular pressing*, Materials Science and Engineering A 257, 1998, 328–332.
- [7] G. Sha, K. Tugcu, X.Z. Liao, P.W. Trimby, M.Y. Murashkin, R.Z. Valiev, S.P. Ringer, *Strength, grain refinement and solute nanostructures of an Al-Mg-Si alloy (AA6060) processed by high-pressure torsion*, Acta Materialia, 63, 2014, 169–179.
- [8] H. Huang, Z. Tang, Y. Tian, G. Jia, J. Niu, H. Zhang, J. Pei, G. Yuan, W. Ding, *Effects of cyclic extrusion and compression parameters on microstructure and mechanical properties of Mg-1.50Zn-0.25Gd alloy*, Materials and Design, 86, 2015, 788–796.
- [9] Srinivasan R., Chaudhury P. K., Cherukuri B., Han Q., Swenson D., Gros P., *Final Technical Report. Continuous Severe Plastic Deformation Processing of Aluminum Alloys*, DOE Award Number: DE-FC36-01ID14022, 2001–2006.
- [10] Wang Ch. P., Li F. G., Wang L., Qiao H.J., *Review on modified and novel techniques of severe plastic deformation*, Science China Press, 9, 2012.
- [11] El-Danaf E. A., *Mechanical properties and microstructure evolution of 1050 aluminum severely deformed by ECAP to 16 passes*, Materials Science and Engineering A 487, 2008, 189–200.

- [12] El-Danaf E. A., *Mechanical properties, microstructure and micro-texture evolution for 1050AA deformed by equal channel angular pressing (ECAP) and post ECAP plane strain compression using two loading schemes*, Materials and Design 34, 2012, 793-807.
- [13] Olejnik L., Rosochowski A.: *Methods of fabricating metals for nano-technology*, Bulletin of the Polish Academy of Sciences, Technical Sciences, 4, 2005.
- [14] B. Mani, M. Jahedi, M. H. Paydar.: *A modyfication on ECAP process by incorporating torsional deformation*, Materials Science and Engineering A, 528, 2011, 4159–4165.

ANETA SZEWCZYK-NYKIEL, MAREK NYKIEL*

ANALYSIS OF THE SINTERING PROCESS OF 316L – HYDROXYAPATITE COMPOSITE BIOMATERIALS

ANALIZA PROCESU SPIEKANIA BIOMATERIAŁÓW KOMPOZYTOWYCH 316L-HYDROKSYAPATYT

A b s t r a c t

The 316L-hydroxyapatite biocomposites were produced by the powder metallurgy technology. The properties and microstructure of these materials are affected by the chemical composition of the powders mixture and the sintering temperature. The sintering temperature of 1240°C and hydroxyapatite addition in an amount of 3% of mass obtained the highest density and hardness and smaller open and closed porosity. Hydroxyapatite addition to austenitic stainless steel modified sintering behaviour. During heating the thermal decomposition of hydroxyapatite took place, which led to the formation of a CaO phase. However, phosphorus diffused into the austenitic matrix and was involved in the eutectic transformation.

Keywords: hydroxyapatite, 316L, biocomposites, microstructure, sintering

S t r e s z c z e n i e

Kompozyty 316L-hydroksyapatyt zostały wytworzono technologią metalurgii proszków. Właściwości i mikrostruktura badanych materiałów uzależnione są od składu chemicznego mieszanki proszków oraz zastosowanej temperatury spiekania. Temperatura spiekania 1240°C i dodatek hydroksyapatytu w ilości 3% wag. pozwalały uzyskać najwyższą gęstość i twardość oraz najmniejszą porowatość otwartą i zamkniętą. Hydroksyapatyt wpływa na przebieg procesu spiekania stali austenitycznej. Podczas nagrzewania następuje rozkład hydroksyapatytu, który prowadzi do powstania fazy CaO. Natomiast fosfor dyfunduje do osnowy austenitycznej, a następnie bierze udział w przemianie eutektycznej.

Słowa kluczowe: hydroksyapatyt, 316L, biokompozyty, mikrostruktura, spiekanie

DOI: 10.4467/2353737XCT.15.178.4383

* PhD. Aneta Szewczyk-Nykiel, PhD. Marek Nykiel, Institute of Material Engineering, Faculty of Mechanical Engineering, Cracow University of Technology.

1. Introduction

Due to its interesting properties, the hydroxyapatite plays an important role as a biomaterial. It is characterized by the highest biocompatibility and biological activity of all the materials used in medicine. Hydroxyapatite owes these features to the similarity of chemical and phase composition to inorganic phases occurring in human bones and teeth [1–7].

The high degree of osseointegration means that hydroxyapatite can directly connect to the bone. Hydroxyapatite is poorly soluble and slowly reabsorbed in tissues [1]. Years of clinical studies (supported by histological studies) have confirmed the high biotolerance and beneficial effect of hydroxyapatite in the process of healing and rebuilding of bone and its ability to initiate and stimulate the formation processes of living organism bones [2].

The range of hydroxyapatite applications is quite broad and covers dentistry, craniofacial surgery, orthopaedics, otolaryngology and plastic surgery [3].

Due to its origin, mineral hydroxyapatite (in igneous rocks, limestone metamorphic or sedimentary rock phosphate), natural hydroxyapatite (mainly in the bones and teeth of vertebrates) [5–9] or synthetic hydroxyapatite [4] can be distinguished. Synthetic hydroxyapatite is the most commonly used on the large scale. This material is quite expensive and does not show total compatibility between the chemical composition to the bone and teeth of the human body [5]. In addition, we should be aware of the fact that its chemical composition and properties highly depend on the conditions of production. Therefore, attempts have been made to obtain a powder of hydroxyapatite from natural sources. From an economic point of view the use of natural hydroxyapatite is preferable. It can be obtained from natural materials, which are simultaneously waste in animal husbandry such as animal bones (beasts, goats, pigs, sheep), eggshells, as well as from coral skeletons or human teeth [4–8]. Most of the processes for preparing hydroxyapatite are relatively simple, cheap and also ensure repeatability of results. The natural hydroxyapatite (obtained from animal bones) takes over some of the properties of the raw material from which has been produced, such as its chemical composition or structure [7, 9]. It has greater compatibility with the hard tissues of the human body compared to synthetic hydroxyapatite. On the other hand, the use of natural hydroxyapatite causes certain concerns. Mainly because an incorrect extraction process creates the possibility of transferring dangerous diseases such as Creutzfeldt Jakob disease, BSE, HIV, hepatitis B and C and AIDS [5]. Despite this, in recent times many attempts have been made to obtain natural hydroxyapatite.

Despite very good biocompatibility and bioactivity, hydroxyapatite bioceramics have low mechanical properties, particularly a low fracture toughness ($K_{IC} = 1.1\text{--}1.2 \text{ MNm}^{-1.5}$ compared to the amount of bone $K_{IC} = 2\text{--}12 \text{ MNm}^{-1.5}$), so that its use is essentially limited to perform implants which do not transfer too high a stress [10, 11].

The ease of bonding hydroxyapatite bioceramics to other materials enables new composite materials to be created [1] and it may be a solution to the problem described above. It is no wonder that new materials are continually sought. Trends observed in recent years in the development of biomaterials indicate precisely the increasing importance of composite materials in implantology. The introduction of hydroxyapatite phase directly to the metal phase, associated with the combination of very good biocompatibility and corrosion resistance of hydroxyapatite with a very good strength and susceptibility to deformation of metals is a very good solution. The metal-ceramic composites constitute promising biomaterials for use in medicine for long-term implants (e.g., articular prosthesis, dental implants) [11–13].

Such composite biomaterials can be successfully obtained by powder metallurgy technology as finished products. Plasma sputtering, CVD and other methods to create a layer of hydroxyapatite can be applied on the surface of a metallic biomaterial implant [1, 10, 12].

Several metal-hydroxyapatite composites have been studied. Particular attention has been paid to composites involving titanium [14–16] and austenitic stainless steel [17–21]. Based on an analysis of the results obtained, it can be concluded that the addition of 316L stainless steel to hydroxyapatite has resulted in an improvement in toughness and strength in comparison to pure hydroxyapatite bioceramics. However, the addition of hydroxyapatite to stainless steel has contributed to increasing the biocompatibility, corrosion resistance and also the hardness and wear resistance of stainless steel [17].

Different compositions of the biocomposite stainless steel 316L-hydroxyapatite have been studied thus far [18]. The hydroxyapatite was introduced in amounts of 0 to almost 50% of mass. It can be stated that the composites with higher hydroxyapatite additive (20 and 50% of mass) had higher porosity and thus lower mechanical strength. Due to these properties, the use of these biocomposites has been precluded as a structural element in the human body [18–19]. Also corrosion resistance (in Ringer's solution) of 316L-hydroxyapatite biocomposites decreased with increasing content of hydroxyapatite [19]. From the viewpoint of mechanical properties the amount of hydroxyapatite has to be smaller than 20% of weight.

The powders of 316L stainless steel and hydroxyapatite were used to obtain biocomposites containing 5, 10 and 15%-mass of hydroxyapatite [20]. The reduction of properties for 316L-hydroxyapatite biocomposites prepared by powder metallurgy was also observed. Namely, when the amount of hydroxyapatite in the powder mixture increased up to 15% mass, the sintered density and also hardness of 316L-hydroxyapatite biocomposites decreased, while the open and total porosity increased. The sintered 316L-hydroxyapatite (5% mass) biocomposite obtained the best combination of physical and mechanical properties.

The 316L steel-hydroxyapatite biocomposites were obtained by powder metallurgy technology in the following stages: mixing the powders of AISI 316L steel and natural origin hydroxyapatite, pressing and sintering. The aim of this study was to clarify the effect of the addition of hydroxyapatite on the sintering process of 316L austenitic stainless steel.

2. Materials for research

Austenitic stainless steel and hydroxyapatite powders were used as the starting materials. The powder of AISI 316L is the commercially available powder manufactured by Höganäs. This grade is water atomized powder with particle size < 150 µm. The chemical composition (in mass %) of AISI 316L is following: 17–18 % Cr, 12–13.5% Ni, 2–2.5% Mo, 0.8% Si, 0.1% Mn, 0.03% C and Fe – up to 100%. The natural origin hydroxyapatite powder was obtained by extracting the cortical part of the long bone of the pig. The procedure for preparing the natural hydroxyapatite involves the following steps: cooking bone in distilled water, the mechanical removal of tissues and parts of the spongy bone residue, leaching of organic matter by 4 molar sodium hydroxide solution, rinsing in distilled water until a constant pH, drying at 120°C to constant weight, and milling [7–8]. The results of a quantitative chemical analysis show that hydroxyapatite powder contained (in % mass): 17.45% P and 39.51% Ca. The value of the Ca/P ratio in the hydroxyapatite was 1.75.

The powders of 316L stainless steel and natural hydroxyapatite were used to prepare the mixtures with the following compositions:

- 316L – 1% mass hydroxyapatite,
- 316L – 3% mass hydroxyapatite,
- 316L – 5% mass hydroxyapatite.

In order to compare the results, pure 316L steel powder was also used for the studies.

3. Experimental procedures

The 316L and hydroxyapatite powders (in appropriate mass proportions) were subjected to mixing for 60 minutes in Turbula. The mixtures thus prepared and also powder of 316L were uniaxially pressed in a rigid matrix at a pressure of 600 MPa. Thus cuboidal samples were obtained with dimensions of $4 \times 4 \times 15$ mm for dilatometric studies. Furthermore cylindrical green compacts of size $\varnothing 20 \times 5$ mm were prepared in the same way. They were designed for density, porosity measurements and microstructural studies.

The sintering process took place in a horizontal NETZSCH 402E dilatometer at two temperatures 1180°C and 1240°C. The 402E DIL was used to evaluate the dimensional changes and phenomena occurring during sintering. During the sintering dry (dew point below -60°C) and high purity (99.9992%) hydrogen flowed by measurement system at a rate of 100 ml/min. The sintering time was 60 minutes. The samples were slowly heated to the isothermal sintering temperature at a rate of 10°C/min. The same rate was applied during cooling samples from sintering temperature to ambient temperature. The sintering process of the cylindrical compacts was carried out in a Nabertherm furnace under the same conditions.

The density and porosity of cylindrical samples were measured by the water-displacement method (according to the requirements of PN-EN ISO 2738:2001 norm).

The hardness (HRB) was determined. A metallographic study of the sintered specimens was done with Nikon Eclipse ME 600P Light Optical Microscopy and Scanning Electron Microscopy (SEM). Microhardness HV0.01(10s) was measured by means of FM 700 E Microhardness Tester.

Dilatometric investigations were carried out in the horizontal NETZSCH 402E dilatometer.

4. Result and discussion

Figure 1 shows the results of sintered density and also relative density measurements of 316L stainless steel and 316L – Hap biocomposites depending on the applied sintering temperature and the amount of hydroxyapatite addition introduced into the powder mixture. The results of open and closed porosity measurements of the same sintered materials are presented in Fig. 2.

The analysis of the above presented results indicates that both sintering temperature and the chemical composition of the powders mixture had an impact on the density and porosity of sintered 316L – Hap biocomposites.

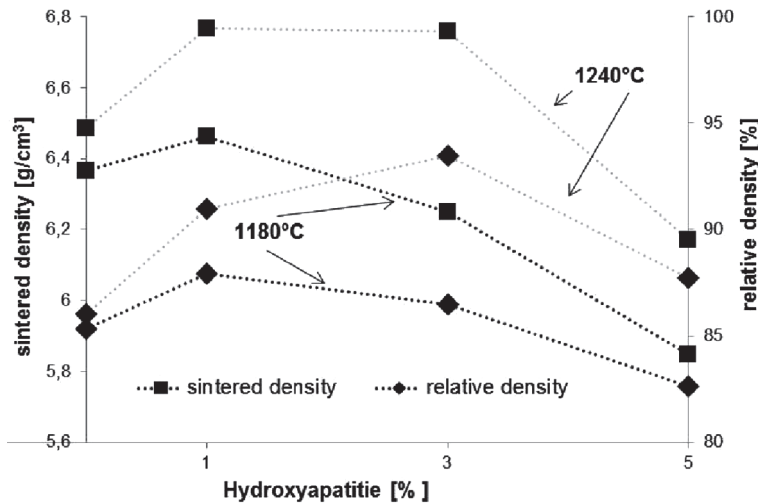


Fig. 1. The influence of sintering temperature and hydroxyapatite addition on density of sintered 316L steel and 316L – Hap biocomposites

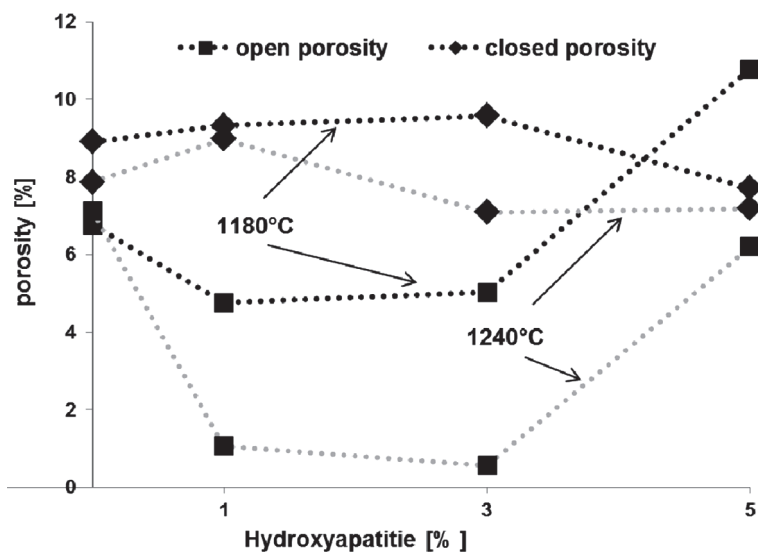


Fig. 2. The influence of sintering temperature and hydroxyapatite addition on porosity of sintered 316L steel and 316L – Hap biocomposites

Regarding the effect of sintering temperature on the physical properties, it can be observed (Fig. 1) that the higher temperature of the sintering process led to much larger values of both sintered density and relative density for all the investigated biocomposites. The same growing trend in density occurred for sintered stainless steel. But the density variation of 316L is not as significant as in the case of the biocomposites studied. Furthermore, it can be

concluded that the increase in the sintering temperature from 1180°C to 1240°C resulted in a decrease in the total, open and closed porosity of sintered 316L – Hap biocomposites and also 316L steel.

As we have already mentioned, the physical properties are significantly affected by the introduction of the hydroxyapatite additive to the material composition. Namely, initially the sintered density and relative density of the biocomposites investigated increases as the amount of hydroxyapatite additive increases up to 1%-mass (in the case of sintering at 1180°C) and 3%-mass (in the case of sintering at 1240°C). Then the densities tend to decline. However, the 316L-5% mass Hap biocomposite shows sintered density below the value obtained for steel 316L.

It should be noted that the effect of the hydroxyapatite addition on the open porosity is just the opposite than in the case of density.

Not only are properties such as density dependent on the sintering temperature and amount of addition of hydroxyapatite. They also decide about hardness as showed results presented in Fig. 3.

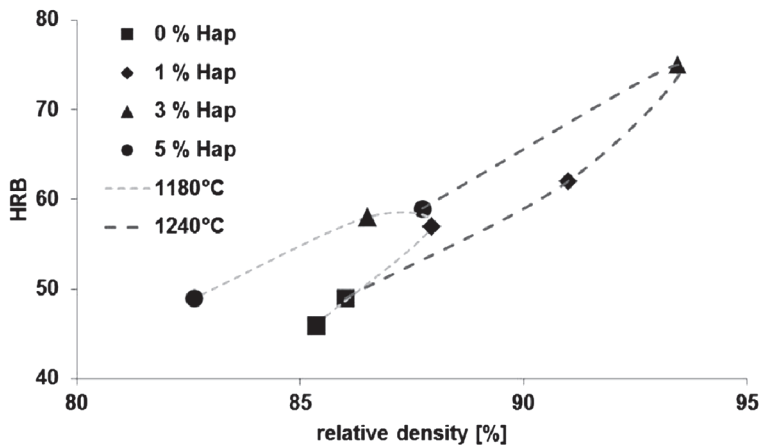


Fig. 3. The influence of sintering temperature and hydroxyapatite addition on relative density and hardness of sintered 316L steel and 316L – Hap biocomposites

For each of the sintering temperatures used the similarity of the relationship between the hydroxyapatite amount and the relative density and hardness of materials obtained can be noted. This means that the initial increase in the content of hydroxyapatite led to an increase in both the density and hardness. The maximum increase in the abovementioned properties occurred in the biocomposite containing hydroxyapatite in amount of 1%-mass sintered at 1180°C. Nevertheless, the combination of the highest values of relative density (93.5%) and hardness (75 HRB) were obtained in the case of 316L-3%-mass hydroxyapatite biocomposite sintered at 1240°C. Further increases in the hydroxyapatite content up to 5% mass meant that the properties were relegated to values comparable to these for sintered 316L steel.

Examples of the microstructures of the materials investigated are presented in Fig. 4-11. The sintered 316L steel (Fig. 4) has an austenitic microstructure. The microhardness of

austenite is about 220 HV 0.01 and 270 HV 0.01 for the steels obtained after sintering at 1180°C and 1240°C respectively.

The introduction of hydroxyapatite addition to 316L steel caused a distinct change in the microstructure of the materials. This is visible in the presented Figures 5–9. The microstructure of the sintered 316L-1%-mass hydroxyapatite material (regardless of sintering temperature) was clearly dual phase. Namely, hydroxyapatite appeared next to the austenite phase. It is also seen in pores disposed at the grain boundaries (Fig. 5, 6). When hydroxyapatite was introduced into the powders mixture in larger quantities (3 and 5%-mass), the microstructure of the sintered biocomposites was dependent on the applied sintering temperature. Namely, there was a heterogeneous eutectic at the grain boundaries of the austenitic matrix (Fig. 7, 9) in the microstructure of sintered at 1240°C biocomposites. Of course, hydroxyapatite was also present. The same microstructure was in 316L-5%-mass hydroxyapatite composites sintered at 1180°C (Fig. 8). Whereas sintered at same temperature 316L-3%-mass hydroxyapatite composite had a dual phase microstructure, as did the sintered 316L-1%-mass Hap biomaterial.

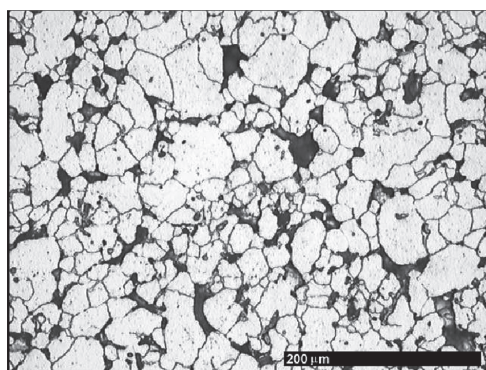


Fig. 4. Microstructure of sintered 316L steel
(sintering temperature – 1240°C)

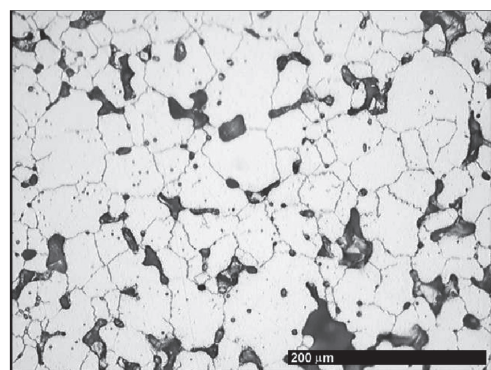


Fig. 5. Microstructure of 316L – 1 mass % Hap
(sintering temperature – 1240°C)

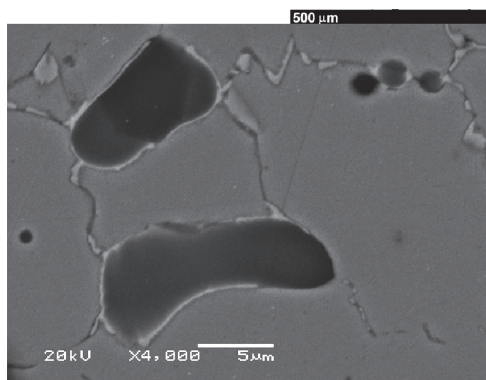


Fig. 6. Microstructure of 316L – 1 mass % Hap
(sintering temperature – 1240°C)

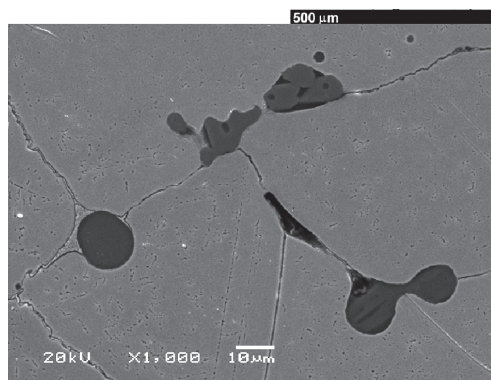


Fig. 7. Microstructure of 316L – 3 mass % Hap
(sintering temperature – 1240°C)

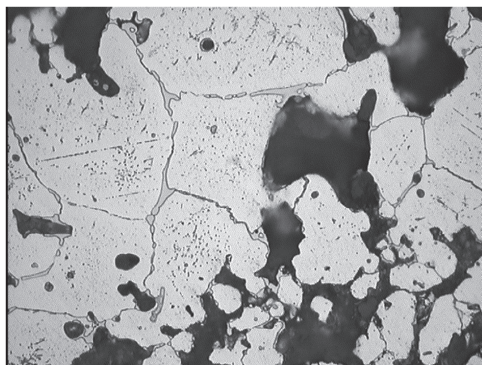


Fig. 8. Microstructure of 316L – 5 mass % Hap
(sintering temperature – 1180°C)

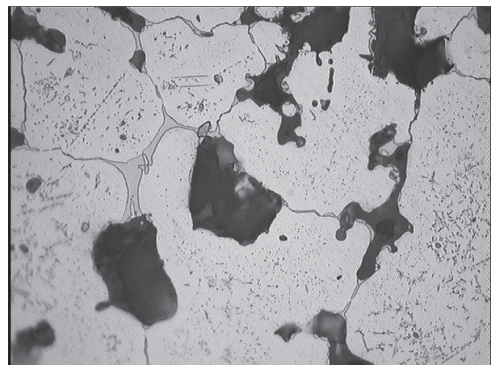


Fig. 9. Microstructure of 316L – 5 mass % Hap
(sintering temperature – 1240°C)

The microhardness of austenite in sintered 316L-hydroxyapatite biocomposites was higher than in the sintered 316L stainless steel. And in addition there was an increasing trend of microhardness with the increase of hydroxyapatite addition. For example after sintering at 1240°C, the microhardness of austenite increased from about 220 HV 0.01 up to about 370 HV 0.01. It was expected that the higher hydroxyapatite content in the materials, the higher the share of eutectic, as well as hydroxyapatite phase.

The SEM microstructure of sintered 316L-5%-mass hydroxyapatite biocomposites (obtained after sintering at 1240°C) and the results of the EDAX analysis are presented in Fig. 10. These results of chemical composition microanalysis (performed at point 1 and 2) are shown in the table below the photograph. Point number 2 was designated in the middle of the austenite grain, while point number 1 was on the grain boundary, where the presence of eutectic was previously observed. Microanalysis of the chemical composition indicated that the main elements at point number 2 were Fe, Cr, Ni. Also traces of P appeared. It should be noted that there was no phosphorus in the chemical composition of the 316L steel. This means that the phosphorus diffused from hydroxyapatite into the austenitic matrix (during the sintering process). The main elements in point number 1 are also Fe, Cr, Ni and P. The eutectic occurred on the austenite grain boundaries. It is associated with the Fe – P equilibrium phase diagram.

Figure 11 presents the SEM microstructure of 316L-3%-mass hydroxyapatite biocomposites sintered at 1240°C. The results of the EDAX are shown in the table below photograph. A microanalysis of chemical composition was performed at point number 1. This point was designated in the middle of hydroxyapatite phase that occurred on the grain boundary. There are such elements as O, Ca and also Cr. However, there is no phosphorus. So it is not exactly hydroxyapatite, as presented above. Therefore it is a new phase. The occurrence of the CaO phase is due to the decomposition of hydroxyapatite during the sintering process. It should be emphasized that this is not free CaO. There was a chromium diffusion from the austenitic matrix to the CaO phase.

It is known that the thermal decomposition of hydroxyapatite depends on the chemical formula of the compound, the presence of small additions of other substances, and the partial pressure of water vapour [22–25]. The stoichiometric hydroxyapatite exhibits

thermal stability up to 1350°C [22–24]. Then (according to the equilibrium phase diagram for CaO-P₂O₅) the hydroxyapatite decomposes into TTCP (tetracalcium phosphate, Ca₄P₂O₉) and α-TCP (α-tricalcium phosphate, Ca₃(PO₄)₂) at 1350°C. This involves no change in weight.

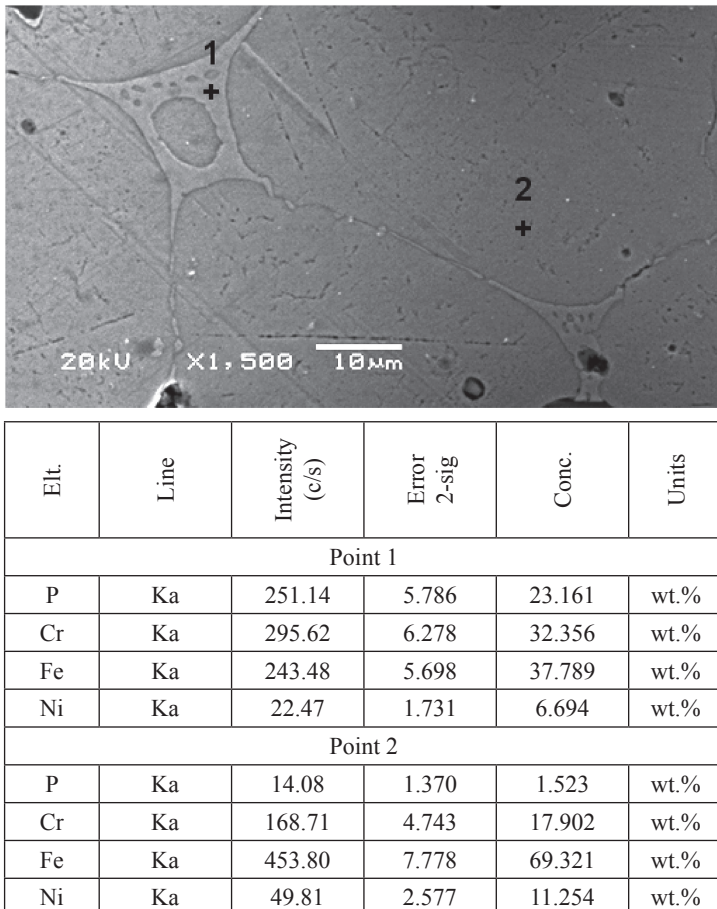


Fig. 10. The SEM microstructure and microanalysis of chemical composition of sintered 316L – 5 mass % hydroxyapatite (sintering temperature – 1240°C)

However, there is an essential difference between synthetic hydroxyapatite and natural hydroxyapatite (extracted from bovine, pig and human bones). Because the Ca/P ratio is higher than 1.67, natural hydroxyapatite is non-stoichiometric. Moreover, it contains carbonate groups and usually some Mg built into its structure [22, 25]. Some investigators reported that the decomposition of non-stoichiometric hydroxyapatite occurs at temperatures below 1000°C. It was found that the products of this decomposition are different depending on the Ca/P molar ratio of the hydroxyapatite [23].

It was demonstrated [8, 9] that the Ca/P ratio for the hydroxyapatite ceramics sintered at 1200°C was lower than that of material sintered at 800°C. According to the authors

this was due to the occurrence of a CaO phase originating from the decomposition of Hap. It was noticed that the natural hydroxyapatite started to decompose at temperatures above 700°C, while CaO occurrence began at a temperature of approximately 800°C. The content of free CaO quickly increased (up to about 1%) with increasing temperature (to 1000°C). These results are also confirmed in other work. According to Knepper [10], hydroxyapatite is not thermally stable during sintering. Namely, both the hydroxyapatite dehydration and irreversible phase transformations take place in composite materials containing hydroxyapatite.

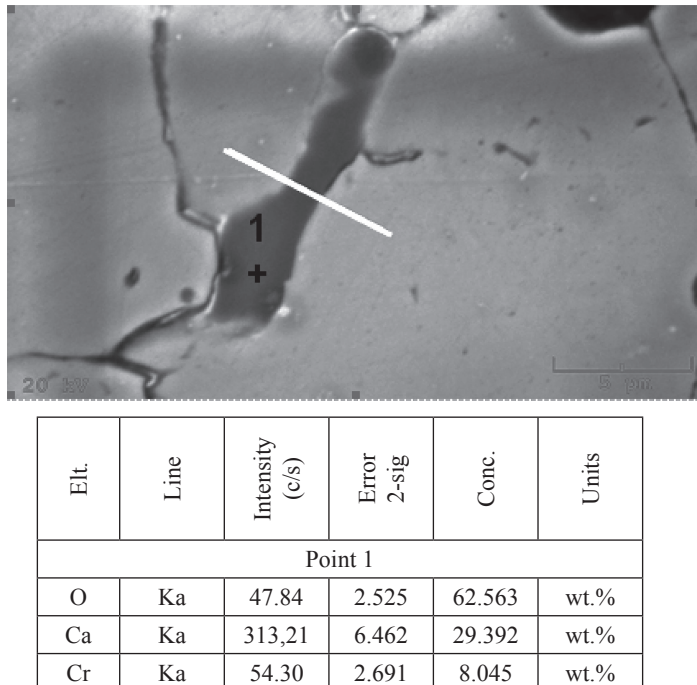


Fig. 11. The SEM microstructure and microanalysis of chemical composition of sintered 316L – 3 mass % hydroxyapatite (sintering temperature – 1180°C)

In the system $\text{CaO}-\text{P}_2\text{O}_5-\text{H}_2\text{O}$ there are many calcium phosphates, which are often the metastable phases. They may occur in the material after a suitable heat treatment. According to the abovementioned phase diagram and the study of the thermal decomposition reaction of hydroxyapatite, some authors have reported that not only calcium phosphate (such as $\text{Ca}_2\text{P}_2\text{O}_7$), but also CaO and P_2O_5 may appear during HAP decomposition [24].

Figure 12 presents the concentration distribution of elements (which occurred in the tested material) along the line marked in Fig. 11. This line passed through the austenite grains and modified CaO phase (originating from the decomposition of Hap) located on the boundary. The measurement of concentration of elements does not enable the quantitative chemical composition of the material to be determined, but it is a very convenient method for the observation of even small changes in the concentrations of the elements.

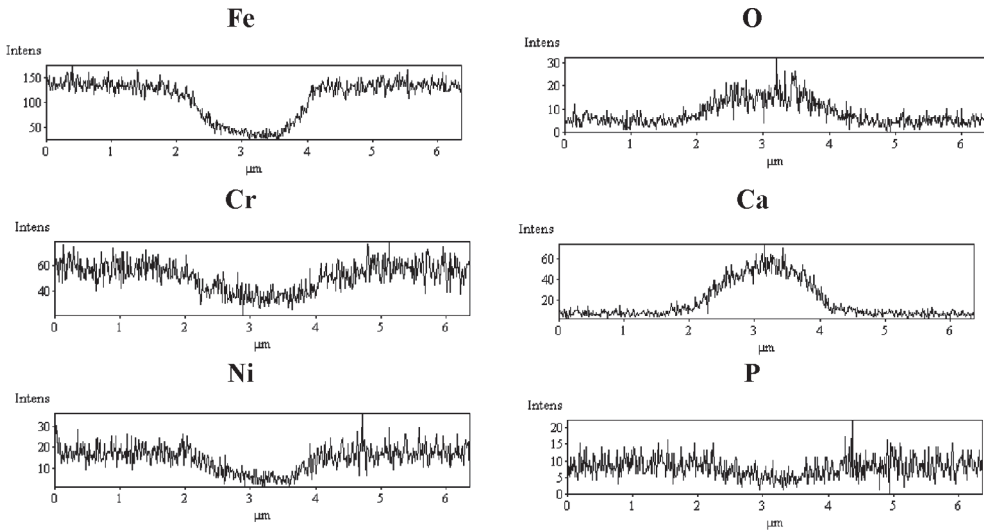


Fig. 12. Concentration distribution of Fe, Ni, Cr, O, Ca and P along a line marked at Fig. 11

It is visible that the concentration distribution of the elements was not the same along the whole length of the measurement line. Namely, the concentration of elements like O and Ca exhibits a marked increase in the area of hydroxyapatite phase occurrence. There is a significant decrease in the concentration of iron, nickel, chromium as well as phosphorus in the phase analysed. This correlates well with the above presented results.

The dilatometric curves of steel 316L and 316L-hydroxyapatite biocomposites recorded during sintering at a temperature of 1240°C are shown in Fig. 13. Analysis of these curves permits the conclusion that hydroxyapatite (depending on the amount introduced into the powder mixture) influences the sintering process of austenitic stainless steel in different ways. Based on the curves presented, the presence of certain points common to all curves and dimensional changes accompanying sintering as a result of occurrence the thermal expansion and sintering shrinkage can be observed.

Initially, as the temperature increases, the thermal expansion of the materials rises, resulting in an increase in sample dimensions. Fig. 13 shows that the presence of hydroxyapatite practically does not contribute to the change in the dimensions of samples in the range of heating from ambient temperature to about 700°C, compared with pure 316L steel. Also the thermal expansion coefficient of 316L-hydroxyapatite biocomposites in this temperature range has a value of about $1.83 \cdot 10^{-5} [1/\text{°C}]$ regardless of the chemical composition of the powder mixture. The presence of hydroxyapatite modified dimensional changes from a temperature of approximately 800°C, from which composites show less swelling than pure steel. The hydroxyapatite reduces the thermal expansion of the materials. After exceeding a temperature of about 850°C thermal expansion starts to decrease, mechanisms of material transport become active. They cause the occurrence of shrinkage. With time, shrinkage starts to dominate over the expansion of the material and we observe the pronounced peak on the curve. The temperature of this peak is about 1000°C for 316L steel. In the case of 316L-hydroxyapatite is within the range of 905–990°C. The shrinkage of samples starts during heating to the sintering temperature.

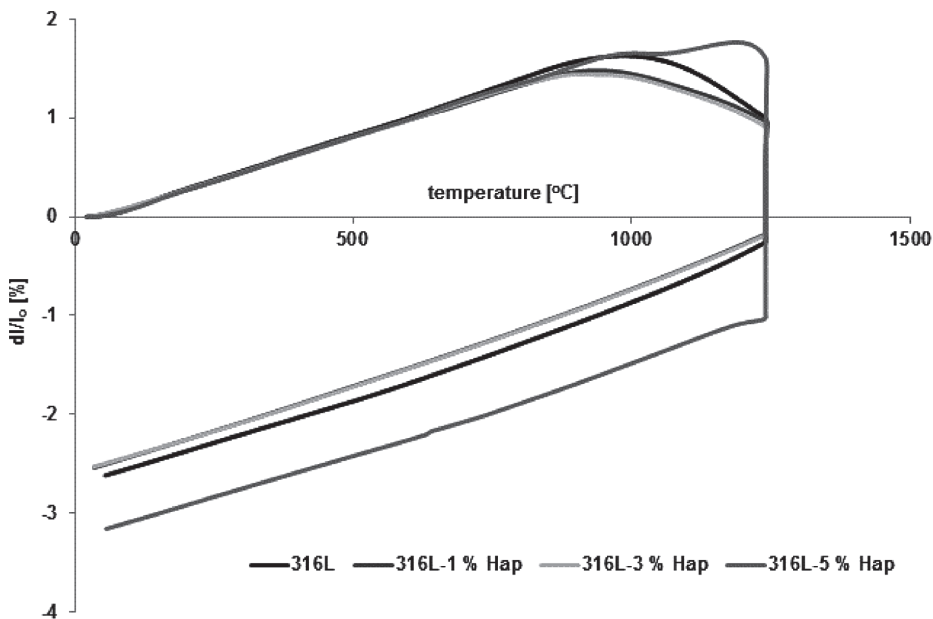


Fig. 13. Dilatometric curves of 316L steel and 316L-hydroxyapatite biocomposites sintered at 1240°C

Because the shrinkage (observed during cooling) is practically the same for all the studied composites (about 2.6 %), the phenomena and processes taking place during isothermal sintering are crucial for the final dimensional changes.

After the whole sintering cycle the highest value of shrinkage was recorded for the sintered 316L-5% mass hydroxyapatite. It equalled 3.16%. This value is significantly larger than the shrinkage observed for other materials. Such a large value of the total shrinkage is associated with a shrinkage occurring during isothermal sintering (Fig. 13), which is caused by the occurrence of a liquid phase. The microstructural studies confirmed the presence of phosphorus in austenite. Hence it can be assumed that there was a reduction of phosphorus oxide with hydrogen during the heating. The analysis of Fe-P equilibrium phase diagram indicates the formation at 1050°C of the eutectic between iron and iron phosphide (Fe_3P), when the content of phosphorus in the ferrite exceeds 2.8 mass %.

5. Conclusion

The 316L-hydroxyapatite biocomposites were obtained using the powder metallurgy technology. The commercially available powder of 316L steel and natural hydroxyapatite (extracted from pig bone) were used. The production process for the samples involved the following steps: mixing powders, pressing and then sintering.

Based on the research results it can be concluded that the properties and microstructure of the sintered biocomposite materials can be changed by selecting of suitable compositions of powder mixture as well as the sintering process parameters.

When the sintering process was carried out at a temperature of 1240°C, the materials under investigation had a higher sintered density, relative density as well as hardness, while the open and closed porosity was lower (compared to the values of these properties obtained after sintering at temperature of 1180°C). Regarding the effect of hydroxyapatite addition on properties, it can be concluded that the combination with the highest values of relative density and hardness and the smaller values of porosity was obtained in the case of 316L-3%-mass hydroxyapatite biocomposite sintered at 1240°C.

Hydroxyapatite addition to austenitic stainless steel modified the sintering behaviour. Namely, the decomposition of hydroxyapatite took place during heating to sintering temperature. This led to the formation of a CaO phase. However, phosphorus diffused into the austenitic matrix and was involved in the eutectic transformation. This was confirmed by the results of the EDAX analysis. It can be observed an austenite matrix, but also heterogeneous eutectic and new phase (formed after the diffusion of chromium to the CaO) on the grain boundaries in the microstructure of 316L-hydroxyapatite biocomposites sintered at 1240°C.

References

- [1] Sobczak A., Kowalski Z., *Materiały hydroksyapatytowe stosowane w implantologii*, Czasopismo Techniczne, z. 1-Ch/2007, 149–158.
- [2] Dawidowicz A., Pielka S., Paluch D., Kuryszko J., Staniszewska-Kuś J., Solski L., *Zastosowanie mikroanalizy pierwiastkowej do oceny osteindukcyjności i osteokondukcji dokostnych implantów hydroksyapatytowych*, Polimery w medycynie, nr 1, 2005, 1–19.
- [3] Zima A., Paszkiewicz Z., Śłosarczyk A., *Bioceramika TCP (α TCP, β TCP, BTCP) dla ortopedii i stomatologii – otrzymywanie oraz ocena w testach in vitro*, Materiały Ceramiczne, 62, 1, (2010), 51–55.
- [4] Sobczak-Kupiec A. Wzorek Z., *Właściwości fizykochemiczne ortofosforanów wapnia istotnych dla medycyny – TCP i HAp*, Czasopismo Techniczne, z. 1-Ch/2010, 309–321.
- [5] Elkayer A., Elshazly Y., Assaad M., *Properties of Hydroxyapatite from Bovine Teeth, Bone and Tissue Regeneration Insights* 2009, 2, 31–36.
- [6] Xiaoying L., Yongbin F., Dachun G., Wei C., *Preparation and Characterisation of Natural Hydroxyapatite from Animal Hard Tissues*, Key Engineering Materials, vol. 342–343, 2007, 213–216.
- [7] Haberko K., Bućko M., Mozgawa W., Pyda A., Zarębski J., *Hydroksyapatyt naturalny – preparatyka, właściwości*, Inżynieria Biomaterialów, R. 6, nr 30–33, 2003, 32–37.
- [8] Janus A. M., Faryna M., Haberko K., Rakowska A., Panz T., *Chemical and microstructural characterization of natural hydroxyapatite derived from pig bones*, Microchim Acta, vol. 161, no 3–4, June 2008, 349–353.
- [9] Haberko K., Mirosław M., Bućko., Brzezińska-Miecznik J., Haberko M., Mozgawa W., Panz T., Pyda A., Zarębski J., *Natural hydroxyapatite – its behavior during heat treatment*, Journal of the European Ceramic Society, vol. 26, 2006, 537–542.
- [10] Knepper M., Milthorpe B.K., Moricca S., *Interdiffusion in short-fibre reinforced hydroxyapatite ceramics*, Journals of Materials Science: Materials in Medicine 9, 1998, 589–596.

- [11] Dudek A., Przerada I., *Kompozyty metalowo-ceramiczne do zastosowań w medycynie*, Materiały Ceramiczne, 62, 1, 2010, 20–23.
- [12] Niespodziana K. Jurczyk K., Jurczyk M., *Synteza bio nanomaterialów kompozytowych typu tytan-hydroksyapatyt*, Inżynieria Materiałowa, nr 3/2006, 636–639.
- [13] Szewczyk-Nykiel A., Kazior J., Nykiel M., *Charakterystyka biomaterialów kompozytowych typu AISI 316L-hydroksyapatyt*, Czasopismo Techniczne, z. 2-M/2009, 39–44.
- [14] Balbinotti P., Gemelli E., Buerger A.G., Lima A.S., De Jesus J., Camargo N.H.A., *Microstructure Development on Sintered Ti/HA Biocomposites Produced by Powder Metallurgy*, Materials Research, 14(3), 2011, 384–93.
- [15] Karimi S., Nickchi T., Alfantazi A.M., *Long-term corrosion investigation of AISI 316L, Co–28Cr–6Mo, and Ti-6Al-4V alloys in simulated body solutions*, Applied Surface Science, 258, 2012, 6087–96.
- [16] Silva G., Baldissera M.R., Trichêes E.S., Cardoso K.R., *Preparation and characterization of stainless steel 316L/HA biocomposite*, Materials Research, 16(2), 2013, 304–309.
- [17] Miao X., *Observation of microcracks formed in HA-316L composites*, Materials Letters, 57, 2003, 1848–53.
- [18] Silva G., Baldissera M. R., Trichêes E., Cardoso K. R., *Preparation and Characterization of Stainless Steel 316L/HA Biocomposite*, Materials Research, 16(2), 2013, 304–309.
- [19] Robin A., Silva G., Rosa J. L., *Corrosion Behavior of HA-316L SS Biocomposites in Aqueous Solutions*, Materials Research, 16(6), 2013, 1254–1259.
- [20] Szewczyk-Nykiel A., Nykiel M., *Study of hydroxyapatite behaviour during sintering of 316L*, Archives of Foundry Enginnering, vol. 10, 3/2010, 235–240.
- [21] Szewczyk-Nykiel A., Nykiel M., Kazior J., *Spiekane biomateriały kompozytowe AISI 316l – hydroksyapatyt*, Czasopismo Techniczne, z. 6-M/2012.
- [22] Haberko K., Bućko M., Mozgawa W., Haberko. M. Pyda A., *Przemiany hydroksyapatytu pochodzenia naturalnego w podwyższonych temperaturach i wybranych atmosferach*, Inżynieria Biomaterialów, R. 9, nr 58–60, 2006, 35–37.
- [23] Zima A., *Wpływ dodatków modyfikujących na właściwości hydroksyapatytowych wielofunkcyjnych tworzyw implantacyjnych przeznaczonych na nośniki leków*, AGH, Kraków 2007.
- [24] Liao C.J., Lin F.H., Chen K.S., Sun J.S., *Thermal decomposition and reconstitution of hydroxyapatite in air atmosphere*, Biomaterials, 20 (1999), 1807–1813.
- [25] Mezahi F.Z., Oudadesse H., Harabi A., Gal Y., Cathelineau G., *Sintering Effects on Physico Chemical Properties of Bioactivity of Natural and Synthetic Hydroxyapatite*, Journal of the Australian Ceramic Society Volume 47[1], 2011, 23–27.

CONTENT

E. Augustyn, M. S. Kozięń: Possibility of existence of torsional vibrations of beams in low frequency range	3
K. Dobaj: Influence of car wheel suspension parameters on improvement of active safety and ride comfort	13
P. Dobrzański: Active system for control of operational parameters of mine diesel locomotive drive	23
P. Dobrzański, K. Kaczmarczyk: Tests of diesel drives carried out at KOMAG.....	35
S. Guzowski, M. Michnej: Fretting wear in the wheel–axle joint of a wheel set with an automatic gauge change system	43
M. Kluziewicz: Modelling manoeuvres that may induce side skid in a front-wheel drive car	53
J. Kłaput: Influence of aging temperature on mechanical properties of the precipitation hardened martensitic MARVAC 300 steel.....	61
K. Maciejasz, R. Bogucki: The effect of deformation route in Equal Channel Angular Pressing on mechanical properties of aluminum alloy 1050.....	71
A. Szewczyk-Nykiel, M. Nykiel: Analysis of the sintering process of 316L – hydroxyapatite composite biomaterials.....	79

TREŚĆ

E. Augustyn, M. S. Kozięń: Możliwości wystąpienia drgań skrętnych w belkach w zakresie niskoczęstotliwościowym.....	3
Krzysztof Dobaj: Wpływ parametrów zawieszenia kół samochodu na poprawę bezpieczeństwa czynnego i komfortu jazdy	13
Piotr Dobrzański: Aktywny system kontroli parametrów pracy układu napędowego górniczej lokomotywy spalinowej.....	23
P. Dobrzański, K. Kaczmarczyk: Kierunki badań napędów spalinowych prowadzone w ITG KOMAG.....	35
S. Guzowski, M. Michnej: Zużycie frettingowe w połączeniu koło–oś zestawu kołowego z automatyczną zmianą rozstawu kół.....	43
M. Kluziewicz: Modelowanie manewrów wywołujących stan zarzucenia w samochodzie przednionapędowym.....	53
J. Kłaput: Wpływ temperatury starzenia na właściwości stali martenzytycznej gatunku MARVAC 300 utwardzanej wydzieleniowo	61
K. Maciejasz, R. Bogucki: Wpływ drogi odkształcenioplastycznego w procesie ECAP (Equal Channel Angular Pressing) na właściwości mechaniczne stopu aluminium z serii 1050	71
A. Szewczyk-Nykiel, M. Nykiel: Analiza procesu spiekania biomateriałów kompozytowych 316L-hydroksyapatyt.....	79